SST DIURNAL VARIABILITY IN THE CLIMATE FORECAST SYSTEM AND ITS INFLUENCE ON LOW FREQUENCY VARIABILITY

by

Jian Li
A Dissertation
Submitted to the
Graduate Faculty
of
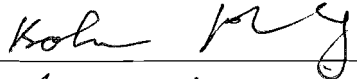George Mason University
in Partial Fulfillment of
The Requirements for the Degree
of
Doctor of Philosophy
Climate Dynamics
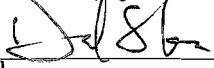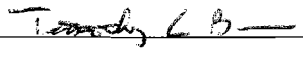
Committee:

_____   Dr. Bohua Huang, Dissertation Director

_____   Dr. Barry Klinger, Committee Member

_____   Dr. Edwin Schneider, Committee Member

_____   Dr. Paul Schopf, Committee Member

_____   Dr. David Straus, Committee Member

_____   Dr. Ruixin Yang, Committee Member

_____   Dr. David Straus, Department Chair

_____   Dr. Timothy L. Born, Associate Dean for
Student and Academic Affairs, College of
Science

_____   Dr. Vikas Chandhoke, Dean, College of
Science

Date: _____   Fall Semester 2011
George Mason University
Fairfax, VA

SST Diurnal Variability in the Climate Forecast System and its Influence on Low
Frequency Variability

A dissertation submitted in partial fulfillment of the requirements for the degree of
Doctor of Philosophy at George Mason University

By

Jian Li
Master of Science
Beijing University, 2005
Bachelor of Science
Lanzhou University, 2002

Director: Bohua Huang, Associate Professor
Department of Atmospheric, Oceanic, and Earth Sciences

Fall Semester 2011
George Mason University
Fairfax, VA

Acknowledgments

First and foremost, I would like to express my deepest gratitude to my advisor, Dr. Bohua Huang, who has supported me throughout my dissertation with his patience, guidance and knowledge. This dissertation would not have been completed or written without his inspiration and encouragement. One simply could not wish for a better and friendlier advisor.

I would also like to thank all my committee members: Dr. Barry Klinger, Dr. Edwin Schneider, Dr. Paul Schopf, Dr. David Straus and Dr. Ruixin Yang, for their encouraging words, thoughtful criticism, and time and attention during busy semesters.

I sincerely thank Dr. Andreas Schiller and Dr. Xubing Zeng. They have generously offered two types of the diurnal mixed layer parameterization scheme they developed, respectively, which is a critical factor in the success of my experiments. I would also like to thank Dr. Zhaohua Wu for kindly providing his novel time series analysis method, Ensemble Empirical Mode Decomposition, which is a powerful tool to identify the periodic signal in the data.

In my daily work I have been blessed with a friendly and cheerful group of students. Their friendship is a valuable treasure I have gained in the past several years. Among them, special thanks are given to Mr. Erik Swenson and Mr. Gary Bucher for their patiently correcting my writing.

I acknowledge the Department of Atmospheric, Oceanic and Earth Sciences, George Mason University and Center for Ocean-Land-Atmosphere Studies for providing financial assistance and other necessary resources for completing my doctoral program.

Finally, I would like to thank my family members, especially my wife, Jia Wang, for supporting and encouraging me to pursue this degree.

Table of Contents

List of Figures

viii

Abstract

SST DIURNAL VARIABILITY IN THE CLIMATE FORECAST SYSTEM AND ITS INFLUENCE ON LOW FREQUENCY VARIABILITY

Jian Li, PhD

George Mason University, 2011

Dissertation Director: Bohua Huang

The diurnal cycle of sea surface temperature (SST) is one of the fundamental periodic variations in the earth climate system. It is generated by the upper ocean′s response to large diurnal change of the incoming solar radiation and other local metrological conditions such as wind stress, precipitation etc. In situ observations and satellite remote sensing have indicated that the SST day-night difference can be highly varied from daily to intraseasonal time scales and the amplitude of the variation can be up to $2-3^oC$ under certain conditions. The potential impacts of diurnal SST variation on the weather and climate deserve further investigation. In particularly, it has been hypothesized that the episodic enhancement of the SST diurnal amplitude actively affects organized convections over the western Pacific warm pool and modulates the tropical atmospheric intraseasonal variability. The hypothesis, however, cannot be verified with current coupled ocean-atmosphere general circulation models (CGCMs) because the SST diurnal cycle has yet to be efficiently resolved in these global climate models.

We believe that realistic representation of SST diurnal cycle in CGCMs is important because such enhancement may improve the capability of these models to simulate weather and climate. The major difficulty in simulating the SST diurnal cycle is due to the inability

of current CGCM oceanic components to resolve the transient diurnal mixed layer evolving within the upper few meters of sea water. Here we adopt two sub-layer parameterization schemes, which are designed by other scientists based on the diurnal mixed layer theories but have not been implemented in CGCMs for climate research, to the Climate Forecast System (CFS) developed by National Center for Environmental Prediction (NCEP). Both parameterization schemes have been fully tested; multi-year simulations and several sensitivity experiments have been conducted. The SST diurnal cycle has been objectively extracted from the simulations and compared with The Tropical Ocean Global Atmosphere Coupled Ocean Atmosphere Response Experiment (TOGA/COARE) observations and an empirically reconstructed dataset of daily SST diurnal variation based on the International Satellite Cloud Climatology Project (ISCCP) and Special Sensor Microwave/Imager (SSM/I). The results show that the CFS with sub-layer parameterizations can reproduce the characteristics of the spatial pattern and temporal variation of SST diurnal cycle to a large extent. Furthermore, we study the diurnal SST effects on the mean state and low frequency variability, with an emphasis on the atmospheric intraseasonal oscillation, through a comparison of the error patterns of the model simulation including the diurnal mixed layer process with the original CFS simulation without diurnal variation. A possible mechanism for the feedback of SST diurnal variability on tropical atmospheric intraseasonal variability has been discussed.

Chapter 1: Introduction

The diurnal cycle is one of the fundamental periodic variations in the earth climate system. The diurnal variation of the sea surface temperature (SST) was first measured scientifically at least a century ago. Sverdrup et al. (1942) and Roll (1965) reviewed some early observational studies using research vessel SST data. These studies indicated that the diurnal amplitude of SST was about 0.2-0.6^{o}C on average, varying with latitude and season. The early researchers also realized that the diurnal SST amplitude depended on cloudiness and wind speed, with day-night SST difference reaching 1.5^{o}C spotted at certain locations under clear, calm sky. More recent observations from buoys, profiling floats, and infrared radiometers on vessels reported larger diurnal SST amplitude of 2-3°C in calm and clear conditions. In some extreme cases, day-night SST differences exceeding 5°C were recorded (e.g. Flament et al., 1994; Yokoyama et al., 1995).

Since the 1980s, remote sensing instruments on operational satellites have been systematically measuring the day-night temperature difference averaged within the oceans thin skin layer of a depth of approximately 10-20μm. The skin layer temperature, or the "skin SST", is more representative of the lower boundary temperature the atmosphere feels than the in situ "bulk SST", which represents the mean temperature for about 1-meter depth. These satellite measurements provided not only more accurate estimates of the day-night SST difference but also its temporal-spatial distribution that was previously unavailable. In particular, wide areas of large diurnal cycle were more clearly identified. For instance, using the Advanced Very High Resolution Radiometer (AVHRR) measurements, Cornillon and Stramma (1985) found that a large diurnal warming occurs around the ridge of the Azore-Bermuda high pressure in spring and summer, with the maximum day-night SST difference reaching 3-4°C. Large diurnal SST variations were also observed frequently in the marginal seas around Japan from spring to summer (e.g. Sakaida et al., 2000). However, the

spatial distribution of the oceanic diurnal amplitude, as well as its annual and interannual variations, has yet to be mapped with more measurements. The corresponding deepening/shoaling of the oceanic mixed layer on a daily scale should also be further investigated. Kawai and Wada (2007) provided a comprehensive review of the recent progress on some of these issues. Several basic aspects of them are directly related to our topic are further discussed below.

1.1 Basic processes of the diurnal SST variability

The diurnal cycle of SST is due to the large variation in day/night surface solar radiation. Its strength, however, also depends critically upon the stratification and currents of the upper ocean. A few hours after sunrise, the heated surface layer reaches the compensation depth where the absorbed solar radiation balances the surface heat loss (Woods and Barkmann, 1986; Fairall et al., 1996). Afterwards, growing solar heating inhibits convection and traps heat and momentum within the thin surface layer. A competing process working against this tendency is associated with the vertical shear of the wind-induced inertial jet, which accelerates downwind in the morning but turns against wind by early evening. At the bottom of the heated water, perturbations grow rapidly due to the Kelvin-Helmholtz instability when the bulk Richardson number, i.e., the ratio of the stratification to the shear of the diurnal jet, drops below a critical value (Pollard et al., 1973). The resultant finite-amplitude perturbations break up the layer interface and accelerate entrainment. As the work of the shear stress is used to lift and agitate dense waters from below, the bulk Ricardson number is restored to its neutral or marginally stable value. The surface heating and inertial currents are then built up for the next stage of the mixing. This repeated penetrating mixing deepens the mixed layer and limits the surface warming phase to only about half of the period during which the net heat flux is into the ocean. Following this characterization, Price et al. (1978) divide a typical diurnal cycle of the upper ocean into three stages:

Stage 1. Warm layer formation. From sunrise until about noon, thermal stratification is formed within the top few meters of the ocean due to strong insolation. Usually, the intense warming occurs within one meter of the sea surface, which is called the "warm layer". The large stratification at the bottom of this layer (i.e., the diurnal thermocline) effectively cuts off the downward gradient heat diffusion and the expansion of the warm layer into deeper ocean.

Stage 2. Deepening due to penetrating mixing. Starting within a few hours after noon, wind mixing begins to play a major role in mixing downward the heat stored near the surface. This mixing process follows the mechanism described by Pollard et al. (1973), which uses the mechanical energy to lift denser water below. The entrainment of colder water from below causes a decrease in the warm layer temperature and SST, even though the net heat flux from the sea surface is still positive. Below the warm layer, the wind-induced mixing causes warming.

Stage 3. Nocturnal dissipation. By around midnight, the downward transport of the heat flux has reached a depth of several tens of meters. There is a continuous net heat loss to the atmosphere at the sea surface due to the disappearance of shortwave radiative heating. The direct loss of heat at the sea surface reinforces the cooling within the diurnal mixed layer, which already occurred in the late afternoon due to the entrainment of the cooler water from below. It also generates convection that is more effective for the cooling throughout the layer. Heat loss continues until the following sunrise when there are little remnants of the diurnal mixed layer.

1.2 Weather and climate influences of the diurnal SST variability

As our knowledge of the observed diurnal SST variability improves, researchers are getting more and more interested in its influences on air-sea interactions and the earth's climate. It is estimated that the SST diurnal cycle increases the long-term mean of the net surface

heat flux from the ocean to the atmosphere by more than 10 W m^{-2} because the warmer daytime SST generates an additional oceanic heat loss of 50-60 W m^{-2} (Kawai and Wada, 2007). This magnitude of heat exchange is not negligible for both oceanic and atmospheric heat balance.

Moreover, the SST diurnal cycle is likely to play more significant role in the western Pacific warm pool where the intraseasonal atmospheric variability is active. During the Tropical Ocean Global Atmosphere (TOGA)/Coupled Ocean-Atmosphere Response Experiment (COARE), substantial diurnal SST variations were detected there during episodes of relatively calm and clear weather, even though the local cloud covers are usually high (Godfrey et al., 1998). Using satellite data, Qin et al. (2007, 2008) found exceptionally strong SST diurnal cycle during the so-called hot events in the warm pool, when SST is higher than 30°C over an area greater than 3×10^6 km^2 and lasts for more than 10 days. These SST diurnal signals may not simply be a passive response to the atmospheric forcing because the air-sea feedback on daily scale also modifies the SST and atmosphere on longer times scales (e.g. Shinoda and Hendon, 1998; Slingo et al., 2003; Bernie et al., 2005)

There are indications that the episodic diurnal SST change can influence intraseasonal variability in the atmosphere. Slingo et al. (2003) proposed a hypothesis of the impact of diurnal SST variability on The Madden-Julian Oscillation (MJO), following the Blade and Hartmann (1993) recharge-discharge scenario. Blade and Hartmann (1993) suggest that the timescale of MJO is set by the time it takes to rebuild moist static energy over the warm pool after it was consumed during last convective episode. Slingo et al. (2003) argue that stronger SST diurnal cycle during a suppressed MJO phase triggers shallow convection, which moistens the lower-to-middle atmosphere, thus recharging the moist static energy. As a result, it preconditions the atmosphere for the next active MJO phase, which is likely to enhance the intensity of the MJO and even to affect its temporal development. Therefore, resolving the episodic enhancements of the SST diurnal cycle in a climate system is crucial for the MJO simulation. In essence, scale interaction lies at the heart of this paradigm.

In addition to affecting the atmosphere, the presence of a diurnal thermocline below the

sea surface may also directly contribute to the SST variation on intraseasonal time scales. Bernie et al. (2005) used observations from TOGA/COARE and a one-dimensional oceanic mixed layer model to investigate the rectification of the SST intraseasonal variability by the diurnal cycle in the western Pacific. They found that a control run (CTL) performed at 1-m vertical resolution forced by hourly surface forcing measured at a specific location gives a good qualitative representation of the observed temperature profiles. However, when the same model was forced with daily mean fluxes (referred to as 24HR), the magnitude of its SST intraseasonal variability is reduced by $0.34^{o}C$, which is a 40% reduction compared to that of CTL. To assess the sensitivity to model resolution, they also run the hourly forcing experiment at 10-m vertical resolution. At lower resolution the model seriously underestimates both the diurnal and intraseasonal variability of SST at such resolution, with magnitudes actually being reduced to $0.23^{o}C$ and $0.41^{o}C$, respectively. These results suggest that in order to fully account for the upper ocean diurnal cycles climate effects in a coupled system, high temporal resolution is required to resolve surface flux exchange and high vertical resolution is required to resolve the stratification within a few meters from the sea surface. In a set of ocean model experiments, Sui et al. (1997) also found that the mixed-layer variations on diurnal timescale is nonlinearly related to the SST intraseasonal variability. The influence on the intraseasonal SST anomalies forms an indirect mechanism for the diurnal cycle to modulate the tropical convection associated with the MJO.

Although the relative roles of these mechanisms are not yet clear, there has modeling evidence suggesting that diurnal air-sea interaction potentially important has an effect on the MJO. For instance, Woolnough et al. (2007) found that the medium-range predictive skill of a model forecast is improved by resolving the SST diurnal cycle, particularly for the MJO phases when the convection is active over the Indian or West Pacific Ocean. Specifically, they performed three sets of hindcast experiments with different treatments of SST, the first provided by the persistence of the initial conditions, the second generated by coupling hourly to a full dynamical ocean model with typical vertical resolution (10m) in the upper ocean (CONT), and the third by hourly coupling to a one-dimensional oceanic

mixed layer model (Large et al., 1994) with high vertical resolution (1m) (ML). Each set of experiments consists of a series of 32-day forecasts using a five-member ensemble initialized at 00 UTC each day from the 15 December 1992 to 31 January 1993.

The MJO signal is diagnosed in these integrations using multivariate empirical orthogonal functions (EOFs) (Wheeler and Hendon, 2004). Its forecast skill is measured by comparing the two observed leading principal component (PC) time series with the predicted ones. Compared with the experiment using fixed SST, both CONT and ML forecasts, which allow for air-sea interactions, show longer periods with correlation excess of 0.6. Moreover, coupling to the high-resolution mixed layer model (ML) further improves the forecast skill over the low-resolution dynamical ocean by extending the period of correlations in excess of 0.6 from 14 to 19 days. The improvement is contributed to the enhanced sensitivity of the SST to the surface flux anomalies. Since the surface fluxes in the CONT and ML experiments are similar, the difference in the SST amplitudes shows the importance of representing the diurnal mixed layer accurately. Additional experiments using the mixed layer model with either lower resolution or daily coupling degrade the forecast skill, which confirms their conclusion.

1.3   Theoretical models of diurnal mixed layer

Since the diurnal cycle of SST is related to the intraseasonal variability nonlinearly, a logical approach to study their interaction is through coupled ocean-atmosphere general circulation models (CGCM) experiments. According to the physical processes involved in the formation of the diurnal SST variation as we mentioned previously, a correct representation of the diurnal mixed layer is necessary for simulating the SST diurnal cycle realistically. The main challenge for the mixed layer modeling is to faithfully parameterize the turbulent mixing processes. Two general categories of such parameterization are the gradient (or turbulence closure) and bulk models.

The gradient models parameterize the turbulent fluxes in terms of the vertical gradient

of mean properties with different orders of turbulent closure assumption. Major parameterizations in this category include non-local K-profile parameterization (KPP) by Large et al. (1994) and the level-2.5 turbulent closure scheme by Mellor and Yamada (1974). These parameterizations can resolve the structure of the mixed layer explicitly if vertical resolution is sufficiently high. In particular, Woolnough et al. (2007) have used KPP in their successful simulation of the diurnal mixed layer with a one-dimensional model. The gradient models also have the advantage of relatively universal formulation, which makes it easy for them to smoothly merge with the parameterizations of the subscale turbulence in the interior of the ocean.

Bulk models consider the integrated properties of the mixed layer based on a simple scenario: the depth to which a fluid layer can be thoroughly stirred depends on the amount of turbulent kinetic energy (TKE) available, and within the stirred layer, the stratification should be neutral. A deepening of the layer depth, h, is caused by entrainment at the bottom

$$\frac{\partial h}{\partial t} = -W_e \tag{1.1}$$

where W_e is the rate at which quiescent water below the mixed layer is agitated and mixed upward. Based on our basic assumption, W_e can be determined by the TKE balance of the mixed layer (e.g. Niller and Kraus, 1977) as

$$-g'(h/2)W_e = m_1 h(B/2)H(B) - m_2 W_e \delta V^2/2 + m_3 U_*^3 \tag{1.2}$$

where B is air-sea buoyancy flux; $H(B)$ is the Heaviside function; δV is the mean velocity difference across the base of the mixed layer ; U_* is wind stress friction velocity; and g' is reduced gravity. The left hand side of (1.2) is the rate of potential energy increase during layer deepening, which is supplied by, from left to right of the right-hand side, energy released by free-convection, energy released from the mean flow by the reduction of vertical shear during deepening, and work of wind stress on surface drift current. m_1 , m_2, and m_3

are empirical parameters, representing the energy conversion efficiency of the three sources.

Compared with gradient models, the bulk mixed layer has the advantage that Equation (1.2) has clearer physical meaning and can be easily simplified for special situations. In fact, Pollard et al. (1973) and Price et al. (1978) have pointed out that, for transient processes occurring within days, the dominant balance in (1.2) is between potential energy increase and shear flow kinetic energy release, i.e.,

$$-g'(h/2)W_e = -m_2 W_e \delta V^2/2 \tag{1.3}$$

This balance leads to a critical bulk Richardson number for the stability limit of the mixed layer depth

$$\frac{g'h}{\delta V^2} = R_i \tag{1.4}$$

Its physical meaning has been described in section 1.1, i.e., the Kelvin-Helmholtz instability breaks out as the diurnal jet shear flow becomes too strong. Price et al. (1978) called (1.4) the dynamical instability model (DIM). Analyzing field measurements, they found that the DIM balance prevails during storm-induced mixed layer deepening while the turbulent erosion as represented by the wind work term in (1.2) is roughly negligible. Usually, the mixed layer deepens when δV accelerates, while it ceases to grow as δV decelerates, even though the surface wind stress continues to increase. Previous laboratory results showed that the critical bulk Richardson number is in the range of 0.4-0.8, and Price et al. (1978) found the best fit to their data is 0.65.

Based on the DIM principle, Price and Weller (1986) further developed the following one-dimension model to simulate the temperature (T), salinity(S) and velocity (V) in the diurnal mixed layer:

$$\frac{\partial T}{\partial t} = -\frac{1}{\rho_0 c} \frac{\partial F}{\partial z} \tag{1.5}$$

$$\frac{\partial S}{\partial t} = -\frac{\partial E}{\partial z} \tag{1.6}$$

$$\frac{\partial \mathbf{V}}{\partial t} = -\mathbf{f} \times \mathbf{V} - \frac{1}{\rho_0}\frac{\partial \mathbf{G}}{\partial z} \tag{1.7}$$

where F, E, and G are profiles of unresolved turbulent fluxes. Their surface values are known as: $F(0) = Q$, the net heat flux (positive downward); $E(0) = S(E - P)$, the freshwater flux; $G(0) = \tau$, the wind stress.

The system (1.5)-(1.7) may be solved with prescribed boundary fluxes, an exponentially decaying penetrating solar radiation, and a linearized equation of state. The subgrid turbulent mixing is treated by the so-called hybrid mixed-layer formulation, which assumes that the upper ocean density and velocity will be mixed vertically to depth h to satisfy three stability criteria:

$$\frac{\partial \rho}{\partial z} \geq 0 \tag{1.8}$$

for static stability,

$$R_i = \frac{g\Delta\rho h}{\rho_0(\Delta\mathbf{V})} \geq 0.65 \tag{1.9}$$

for mixed layer shear flow stability, and

$$R_g = \frac{g\partial\rho/\partial z}{\rho_0(\partial\mathbf{V}/\partial z)^2} \geq 0.25 \tag{1.10}$$

for stratified shear flow stability.

where operator Δ takes the vertical difference of a variable across the interface between the mixed layer and the level just beneath. Besides the bulk Richardson number criterion (Eq. 1.9), the criterion for the gradient Richardson number (R_g, Eq. 1.10) produces vertical mixing in a transition layer below the surface mixed layer when the local vertical shear

becomes too large. Price and Weller (1986) found that this model gives good simulations of the observed diurnal mixing processes.

However, current CGCMs are inadequate for directly incorporating these theoretical mixed layer models to reproduce the SST diurnal cycle, mainly because the vertical resolution (10 meters) of the oceanic components is usually too low to resolve the diurnal processes occurring in the top few meters of water. As a result, these very basic physical processes are not adequately represented in most climate models. Given the computational constraints, it is unlikely that the models will acquire the necessary resolution (say, up to 0.5 meters) to explicitly resolve the diurnal mixed layer in the foreseeable future. As an alternative, attempts have been made to parameterize the physics of oceanic mixing near the sea surface at the diurnal scale based on the theoretical mixed layer models. However, to our knowledge, the effectiveness of these parameterizations has not been tested in state-of-the-art climate models. Therefore, the first question we attempt to address is whether the diurnal SST variability can be simulated realistically through physical parameterizations of diurnal mixed layer in a coupled general circulation model. In comparison with the explicitly resolving diurnal mixing processes, physical parameterizations are more suitable for current computational capability. Technically, the parameterization is a portable component that is easily implemented in any CGCM without modifying the model structures dramatically.

If the parameterizations are able to reproduce the realistic diurnal SST variability, we will further investigate whether diurnal SST variability has significant effects on lower frequency ocean and atmosphere variations, including its influences on the climate mean state, the interannual variability and especially, the intraseasonal oscillations over the Indo-Pacific region. Although the previous studies based on the 1-D mixed layer model suggest the relative importance of diurnal SST variability in the air-sea coupling process, the mechanisms of the impact still need to be explored with more sophisticated model. For instance, the significant daytime warming of SST is likely to happen during the suppressed phase of Madden-Julian oscillation, which may increase the evaporation and the heat flux from the

ocean. The changes of the hydrological cycle and the energy balance tend to reduce the SST and intensify the atmospheric convection. However, such feedbacks between atmosphere and ocean can only be explored in a coupled model. We expect the simulations with the coupled model will provide comprehensive understanding of the interactions between the diurnal SST variability and low frequency ocean and atmosphere variations.

Our discussion is arranged as follows: In Chapter 2, we introduce two types of the mixed layer parameterizations that were developed by Zeng and Beljaars (2005) and Schiller and Godfrey (2005), respectively. Following this, we introduced the implementation of the schemes into the NCEP Climate Forecast System (CFS). Chapter 3 shows a thorough comparison between the simulated SST diurnal variability and that from observations. Results indicate the significant improvement of the diurnal SST in the simulations. The influences of the diurnal SST variability on the climate mean state and interannual variability are discussed in Chapter 4. It is found that there are no dramatic changes observed in the mean state and ENSO patterns, but the portion of model biases have been rectified due to the implementation of diurnal SST variability. In Chapter 5, we focus on the impact of diurnal SST on tropical intraseasonal variability, and it is found to mainly affect the strength of the atmospheric intraseasonal oscillations. The summary and discussion are given in Chapter 6.

Chapter 2: Model and Experiments

2.1 CFS model

To simulate the SST diurnal variability and investigate its influences on the atmospheric intraseasonal variability, we conducted a set of numerical experiments on the Climate Forecast System (CFS, Wang et al., 2005; Saha et al., 2006), a state-of-art CGCM developed at the National Centers for Environmental Prediction (NCEP). CFS is a fully coupled model representing the interaction between the Earths oceans, land and atmosphere. Currently the CFS was used for the operational climate prediction at NCEP.

In the CFS, the atmospheric component is a lower resolution version of the Global Forecast System (GFS) that has been the operational weather prediction model at NCEP since 2003. GFS is a spectral model of atmospheric primitive equations with vorticity, divergence, logarithm of surface pressure, specific humidity, virtual temperature, and cloud condensate as dependent variables. It is a spectral model having spherical harmonics with a triangular truncation at wave number 62 (equivalent to nearly 200km in a Gaussian grid) horizontally and 64 levels in a sigma coordinate from the earth's surface to the top of the atmosphere (about 0.27 hPa) vertically. GFS uses leapfrog time stepping as the main time integration scheme for nonlinear advection terms, and a semi-implicit time stepping for gravity wave drag terms and for zonal advection of vorticity and moisture. An Asselin (1972) time filter is applied to reduce computational modes. The time step is 7.5 minutes for the computation of dynamics and physics, except that the full calculation of longwave radiation is done once every 3 hours and shortwave radiation every hour, but with corrections made at every time step for diurnal variations in the shortwave fluxes and in the surface upward longwave flux.

Several physical parameterizations are upgraded from the 2003 version of GFS (Saha

et al., 2006). In the model solar radiation transfer uses multi-band techniques (Hou et al., 1996, 2002) following the approach of Chou (1992), Chou and Lee (1996), and Chou et al. (1998). The algorithm includes absorption/scattering by water vapor, ozone, carbon dioxide, clouds, aerosols and oxygen. Horizontal distribution of surface albedo is a function of Matthews (1985) surface vegetation types in a manner similar to Briegleb et al. (1986). Monthly variation of surface albedo is derived in reference of Staylor and Wilbur (1990). A first-order scheme based on Troen and Mahrt (1986) for boundary layer vertical diffusion (Hong and Pan, 1996) is implemented in planetary boundary layer (PBL). PBL height is diagnostically determined by using the bulk-Richardson approach, then the profile of the coefficient of diffusivity is specified as a cubic function of the PBL height. The actual values of the coefficients are determined by matching with the surface-layer fluxes.

Cumulus convection is based on the simplified Arakawa-Schubert scheme (Grell, 1993; Pan and Wu, 1995; Hong and Pan, 1996). The improved scheme adapts concepts that the sub-scale perturbation is a combination of forcing due to surface inhomogeneities, boundary layer turbulence, and free atmosphere turbulence, and its modulation by grid-scale vertical motion. Gravity wave drag is simulated as described by Alpert et al. (1988). The parameterization includes determination of the momentum flux due to gravity waves at the surface as well as at higher level. The treatment of the gravity wave drag parameterization in the lower troposphere is improved by the use of Kim and Arakawa (1995) enhancement. In addition, the cloud condensate is a prognostic quantity in GFS with a simple cloud microphysics parameterization (Sundqvist et al., 1989; Zhao and Carr, 1997; Moorthi et al., 2001). The large-scale condensation is calculated based on not only on changes in relative humidity, but also changes of temperature, moisture and pressure. The fractional cloud cover used for radiation is diagnostically determined by the predicted cloud condensate. The precipitation is produced from clouds where the condensed water/ice become sufficient.

The oceanic component of CFS is the Modular Ocean Model version 3 (MOM3, Pacanowski and Griffies, 1998) developed by the Geophysical Fluid Dynamics Laboratory(GFDL) in

13

Princeton, New Jersey. MOM3 is a finite difference version of the ocean primitive equations that consist of the Navier-Stokes equations subject to the Boussinesq and hydrostatic approximations. Prognostic variables of the model are the two active tracers: potential temperature and salinity, as well as meridional and zonal velocity, and the height of the free ocean surface. The model domain encompasses non-polar world oceans within 74°S and 64°N with a zonal resolution of 1°, while the meridional resolution is $1/3^{o}$ between10^{o}S and 10°N, gradually decreasing to a fixed resolution of 1° poleward of 30°S and 30°N. MOM3 has 40 vertical levels in height coordinate, with a 10-m resolution from the sea surface to 240m depth and 27 levels in the upper 400m; the bottom depth is around 4.5km. Basically MOM3 uses a centered leapfrog scheme to integrate the prognostic equations; a Robert time filter is applied to handle the computational mode. Vertical mixing in the model follows the non-local K-profile parameterization (KPP) of Large et al. (1994). KPP consists of several entities to deal with unresolved vertical mixing processes in the ocean's surface boundary layer and the interior. Based on the KPP scheme, the boundary layer depth is determined at each grid point according to bulk Richardson number. Surface forcing (buoyancy and momentum) enhances the mixing in the boundary layer and enables the properties of boundary layer to penetrate into the thermocline. The boundary layer profile is constrained to agree with similarity theory of turbulence and is matched to the interior where the mixing is governed by shear instability, internal wave activity, and double-diffusion. Specifically, the KPP scheme has a non-local term that is independent of the vertical gradient and can further enhance the mixing where the water column becomes unstable near the surface. The horizontal mixing of tracers uses the isoneutral method (Gent and MaWilliams, 1990; Griffies et al., 1998). The horizontal mixing of momentum uses the nonlinear scheme of Smagorinsky (1963).

For the simulation of land surface hydrology, a two layer soil model (Mahrt and Pan, 1984) is utilized in CFS. The soil model includes soil thermodynamics and soil hydrology, both modeled as diffusive processes. The evaporation process in the surface energy balance

is represented by three components: direct evaporation from the bare soil surface, transpiration through the leaf stomata, and evaporation of precipitation intercepted by the leaf canopy.

The atmospheric and oceanic components are coupled with no flux adjustment or correction. Because of the difference in latitudinal domain, full interaction between atmospheric and oceanic components is confined to 65ºS-50ºN. Poleward of 74ºS and 64ºN, SSTs needed for the atmospheric model are taken from observed climatology. Between 65ºS and 74ºS and between 50ºN and 64ºN, SSTs for the atmospheric component are a weighted average of the observed climatology and the SST from oceanic component. The weights vary linearly with latitude such that the SSTs at 74ºS and 64ºN are equal to the observed climatology, and SSTs for 65ºS and 50ºN are equal to the values from the oceanic component. Sea ice extent is prescribed from the observed climatology.

CFS was originally designed to exchange daily averaged quantities, such as surface fluxes and SST, between the two components once a day. Such a coupling interval, however, implicitly suppressed the diurnal variability in the ocean model although the diurnal cycle of the solar radiation is fully resolved in the atmospheric component. Bernie et al. (2005) demonstrated that a temporal resolution of 3 hours or shorter is necessary to capture the diurnal variability. So our first experiment (control run, CTL hereafter) is to increase the coupling frequency and to exchange flux/SST between two components on a 3-hour basis. A CFS integration with the higher coupling frequency is carried out for 20 years. The model is stable to carry out the integration with the higher coupling frequence. However, the simulated diurnal SST cycle, as we will show in the following chapters, is unrealistically weak even if the 3-hour coupling interval allows the diurnal change of the surface heat and momentum fluxes into the ocean.

Such a result is not surprising. We have described how critical the turbulent mixing in the upper ocean is to cause the diurnal cycle of SST with the observed strength. However, the coarse vertical resolution (10m) of MOM3 adopted in the current CFS inhibits the sufficient representation of mixing processes near the sea surface, although a comprehensive

15

vertical mixing parameterization scheme (KPP) has been installed in model.

In order to simulate a realistic SST diurnal cycle in the CFS model, besides increasing coupling frequency, we need a correct representation of the diurnal mixed layer. The challenge for the mixed layer modeling is to faithfully represent the consequence of the turbulent mixing processes generated by the diurnal cycle of the surface fluxes into the upper ocean.

2.2 Parameterization Schemes

The challenge for incorporating these diurnal mixing processes into an ocean general circulation model (OGCM) is that the diurnal mixed layer itself is an unresolved feature in many of the current climate models due to their low vertical resolution in the upper ocean. Apart from substantially increasing the number of model levels near the sea surface to resolve it explicitly, an alternative approach is to represent its influences on the model predicted SST through physical parameterization. In general, the diurnal mixed layer can be treated as a sub-layer (or layers) embedded within the upper grid of the OGCM, with its structure and heat budget determined, based on physical principles described in Chapter 1, from large-scale properties (i.e., surface fluxes and the OGCM predicted grid temperature). The sub-layer then produces a new SST, which feeds back to the OGCM through modulating the surface fluxes received by the OGCM. These kinds of parameterization schemes have been in existence for some time and have shown promising results in uncoupled atmosphere model simulations or very simple coupled systems. Surprisingly, as far as we know, they have not been widely used in current climate models. A major task of our study is to examine the effectiveness of these parameterization schemes in realistic environments of climate models. Next, we review two sub-layer parameterizations, which can be seen as following the theoretical models of KPP and DIM respectively. As a result, the schemes are closed with different assumptions.

2.2.1 Zeng and Beljaars skin layer scheme

Zeng and Beljaars (2005) developed a prognostic scheme to calculate the sea surface skin temperature from the mean temperature of an oceanic layer about 10-m in depth. The ocean layer can be seen as the first vertical grid level of an ocean model. Within the top ocean layer, they consider a thin skin layer of depth δ, where molecular thermal flux exchange with the atmosphere is dominant, with a warm layer of strong diurnal cycle beneath. It is further assumed that, at a fixed depth d (3 m) within the ocean layer, the diurnal cycle of temperature is negligible. The governing equation within the warm layer is the vertical heat diffusion:

$$\frac{\partial T}{\partial t} = \frac{\partial}{\partial z}(K_w + k_w)\frac{\partial T}{\partial z} + \frac{1}{\rho_w c_w}\frac{\partial R}{\partial z} \tag{2.1}$$

where the subscript w refers to sea water, T is the sea water temperature and z is the depth defined as positive upward, ρ_w and c_w are the density and volumetric heat capacity of sea water, respectively, K_w and k_w are the turbulent diffusion coefficient and molecular thermal conductivity respectively, and R is the net solar radiation flux defined as positive downward. Assuming that the turbulent diffusion and temperature tendency can be neglected within the skin layer, Equation (2.1) can be vertically integrated from $z = 0$ to $z = -\delta$ with the boundary conditions at $z = 0$ as

$$\rho_w c_w k_w \frac{\partial T}{\partial z} = Q = LH + SH + LW \tag{2.2}$$

and the temperature at the bottom of the skin layer to have

$$T_s - T_{-\delta} = \frac{\delta}{\rho_w c_w k_w}Q + R_s f_s \tag{2.3}$$

where LH, SH and LW are the surface latent and sensible heat flux and the net longwave radiation respectively, positive downward. T_s is the skin temperature and R_s is the net

solar radiation at ocean surface. Following Fairall et al. (1996) and Wick et al. (2005), the fraction of solar radiation of the sub-layer, f_s , can be written as

$$f_s = 0.065 + 11\delta - \frac{6.6 \times 10^{-5}}{\delta}\left[1 - \exp(-\frac{\delta}{8 \times 10^{-4}})\right] \tag{2.4}$$

The skin layer thickness, δ, is taken from Fairall et al. (1996), depends on the surface fluxes and the seawater heat absorption property:

$$\delta = 6\left[1 + \left(\frac{-16g\alpha_w\nu_w^3}{u_{*w}^4 k_w^2 \rho_w c_w(Q + R_s f_s)}\right)\right]^{-1/3} \tag{2.5}$$

where g is gravity, α_w is the thermal expansion coefficient, ν_w is the kinematic viscosity and u_{*w} is the oceanic frictional velocity. T_s is solvable from (2.1)-(2.5) if $T_{-\delta}$ is known.

To get $T_{-\delta}$, we assume molecular thermal conductivity is negligible below the skin layer and integrate (2.1) from $z = -\delta$ to $z = -d$ to result in

$$\frac{\partial}{\partial t}\int_{-d}^{-\delta} T dz = \frac{Q + R_s - R(-d)}{\rho_w c_w} - K_w \frac{\partial T}{\partial Z}\big|_{z=-d} \tag{2.6}$$

where $R(-d)$, the penetrated solar radiation at depth d, can be determined from an empirical formula (Soloviev, 1982). Following the KPP formulation (Large et al., 1994), Zeng and Beljaars (2005) determine the turbulent diffusion coefficient K_w as

$$K_w = 0.4 \times \frac{u_{*w}(-z)}{\phi_t(-z/L)} \tag{2.7}$$

where ϕ_t is the universal stability function and L is the Monin-Obukhov length. The key assumption to close the system is that the temperature profile within warm layer has a

prescribed structure as:

$$T = T_{-\delta} - [(z + \delta)/(-d + \delta)]^{\nu}(T_{-\delta} - T_{-d}) \tag{2.8}$$

where T_{-d} is assumed to be the mean temperature of the ocean layer and ν is an empirical parameter. Zeng and Beljaars (2005) suggested that $\nu = 0.3$ when the depth of warm layer is set to be 3 meters, which provides more realistic diurnal warming of SST. Then the prognostic function for $T_{-\delta}$ can be written as

$$\frac{\partial}{\partial t}(T_{-\delta} - T_{-d}) = \frac{Q + R_s - R(-d)}{d\rho_w c_w \nu/(\nu + 1)} - \frac{(\nu + 1)ku_{*w}}{d\phi_t(d/L)}(T_{-\delta} - T_{-d}) \tag{2.9}$$

Combining with (2.3), we can determine the temperature structure within the warm layer as well as the skin temperature T_s. Zeng and Beljaars (2005) tested this scheme using in situ measurements over tropical and mid-latitude oceans and the ECMWF model and found realistic diurnal cycle of the skin temperature.

2.2.2 Schiller and Godfrey sub-layer scheme

Schiller and Godfrey (2005) embedded a transient sub-layer of warm water in the upper portion of the top grid of an ocean model while the total heat flux received by the model layer is positive. Temperature is assumed to be constant within the sub-layer and the weighted mean of the sub-layer temperature and the temperatures of the rest of the waters in the grid is equivalent to the model-predicted grid temperature. Since the sub-layer traps surface-induced turbulence, waters beneath are assumed to be non-turbulent and heated by penetrating solar flux alone.

Given these assumptions, Schiller and Godfrey (2005) showed that the sub-layer temperature, as well as its temperature and momentum differences for the water immediate beneath its base, can be determined if the surface fluxes, the sub-layer depth, and the model grid temperature are known. Since either observations or an atmospheric model can

provide the surface fluxes and the ocean model predicts the grid temperature, a formulation of the sub-layer depth, D_T, closes the system.

Following the DIM principle, Schiller and Godfrey (2005) argued that, at a given time $t > t_0$ when the sub-layer starts mixing downward mechanically, its bulk Richardson number should be maintained at the critical value, $Ri_c = 0.65$, as suggested by Price et al. (1986), so that:

$$D_T = \left(\frac{\rho C_p Ri_c I_\tau}{\alpha g I_s} \right)^{1/2} \tag{2.10}$$

where I_τ and I_s are respectively the trapped shear-flow kinetic and heat energies accumulated from the time t_0. α is the thermal expansion coefficient and C_p is the heat capacity of sea water.

At dawn, the nocturnal mixed layer is typically deeper than the 1st model level. The warming zone due to the solar radiation newly forms near the surface and inhibits convective deepening at the depth of D_c, where the absorbed solar radiation balances the surface heat loss. The incoming shortwave radiation still warms the new sub-layer at nearly the same rate as that of the non-turbulent water just beneath. Assuming that $D_T(t_0) = D_c$, the rates of momentum and heat fluxes introduced into the layer are just enough for the bulk Richardson number to hold at the critical value (Fairall et al., 1996). If winds are steady and the surface solar heating increases linearly (i.e., no cloud), it can be shown that, shortly afterwards at time t, the accumulations of momentum and heat in the near-surface zone are

$$I_s(t) = \frac{\partial Q_{sw}(t_0)}{\partial t} \frac{G(-D_T(t_0))\Delta t^2}{2} \tag{2.11}$$

$$I_\tau = \left(\frac{|\tau|\Delta t}{\rho} \right)^2 \tag{2.12}$$

where $\Delta t = t - t_0$ and $G(z) = 1 - f(z) + z\partial f/\partial z$ is a function of $f(z)$, the fraction of the surface shortwave radiation passing through level z. τ is the magnitude of wind stress and

20

$\partial Q_{sw}(t_0)/\partial t$ represents the time tendency of surface solar heat flux at t_0. Inserting (2.11) and (2.12) into (2.10), we obtain an equation for $D_T(t_0)$,

$$D_T(t_0)G(-D_T(t_0))^{1/2} = \frac{\tau}{\rho}\left(\frac{2\rho C_p Ri_c}{\alpha g \partial Q_{sw}(t_0)/\partial t}\right)^{1/2} \tag{2.13}$$

Schiller and Godfrey (2005) pointed out that, while (2.11) and (2.12) hold, the sub-layer remains constant while its temperature increases quadratically with time. On longer time scales, the sub-layer in the tropics tends to deepen throughout the day. Whenever D_T reaches the base of the first model grid, the scheme should be discontinued and restart at dawn the next day. Schiller and Godfrey (2005) tested this scheme using a one-dimensional ocean model and got quite realistic results.

2.3   Experiments

As mentioned previously, the surface flux/SST exchange in CFS is conducted on a daily basis with daily averaged fields transferred. As a result, there is no diurnal signal in the oceanic component although the diurnal cycle of the solar input is fully resolved in the atmospheric component. In order to simulate the diurnal cycle of the SST, several experiments are conducted.

As we have briefly described above, the first experiment is to increase the coupling interval of CFS from once a day to every three hours. A multi-year integration of CFS with higher coupling frequency has been performed. Compared with a long-term simulation using the original CFS with the daily coupling conducted by our colleague at COLA, this version of the CFS simulation with the shorter coupling interval show very similar features and there is no significant change of the model mean state although a small diurnal variability is invoked in the ocean. We consider this run as the baseline simulation of the diurnal SST variability by the CFS without any special treatment and will refer to it as the control simulation, or the CTL run, hereafter.

Built upon the CTL run, the two diurnal mixed layer parameterizations are implemented in the CFS and the corresponding simulations are conducted, both with the 3-hour air-sea coupling intervals. For simplicity, hereafter we will refer to the experiments that adopt parameterizations of Zeng and Beljaars (2005) and Schiller and Godfrey (2005) as ZB and SG, respectively. Both schemes have been applied to CFS as an additional "coupler" treatment between the atmospheric and oceanic components of the CFS model. The coupler obtains the required variables, such as the temperature (the bulk SST) from the top ocean level, and the atmospheric surface fluxes are obtained from the oceanic and atmospheric components every three hours. The skin SST in the ZB parameterization and the warm sublayer temperature in the SG parameterizations are then calculated for every oceanic grid point following the procedure described in the previous section. These newly generated SSTs from the parameterizations are then provided as the boundary condition driving the atmospheric integration in the next 3 hours, and consequently atmospheric changes feed back to the ocean for the next cycle.

Both experiments have been carried out for 20 years. In the following chapters, we will evaluate the simulated diurnal SST variability by comparing with the observations and among the different simulations. Furthermore, the impact of diurnal SST on the climate mean state and intraseasonal variability will be explored from the model simulations.

Chapter 3: SST diurnal variability in model simulations

As indicated by many previous studies, large areas of global oceans exhibit significant SST diurnal variability in favorable conditions of high solar insolation and low winds (Stommel et al., 1965; Anderson et al., 1996; Kawai and Kawamura, 2002; Stuart-Menteth et al., 2003; Ward, 2006). But this fundamental component of climate system is not represented in most coupled general circulation models (CGCMs), because current models are designed to conduct the surface flux exchange between the ocean and the atmosphere basis with daily means, totally neglecting the diurnal effect. More importantly, the vertical resolution of oceanic models is too low to resolve the diurnal mixing processes, which is critical to the diurnal cycle of SST, occurring in the top few meters of water.

We have proposed to simulate the SST diurnal variability using a state-of-the-art CGCM through the implementation of diurnal mixed layer parameterizations. Two parameterization schemes (ZB and SG), introduced in the previous chapter, have been embedded in the CFS model. Both parameterizations are capable of creating realistic diurnal SST in one-dimensional idealized experiments (Zeng and Beljaars, 2005; Schiller and Godfrey, 2005). However, they have not been employed in the coupled model for climate research before. Therefore the computational stability of the parameterizations needs to be tested in multi-year simulation. More importantly, we will evaluate simulations extensively to determine how realistically the SST diurnal cycle can be reproduced, which is critical for the further investigation of the relationship between SST diurnal variability and long-term atmospheric variability.

For this purpose, the remainder of this chapter is structured as follows: the in situ observations from TOGA buoys will be introduced to reveal the characteristics of the observed diurnal SST variability in section 3.1. Section 3.2 provides a novel data analysis method for extracting the diurnal signals from the SST time series. Several aspects of the simulated

SST diurnal variability are evaluated in section 3.3. A directly comparison with the in situ observations is made (section 3.3.1), and its annual mean and seasonality patterns are compared with satellite observations (section 3.3.2 and section 3.3.3, respectively). EOF analysis of the simulated diurnal SST variability is compared with that of the reconstructed diurnal warming dataset in section 3.3.4.

3.1 Observational diurnal SST variability

In this study, the CGCM simulated diurnal SST variability is directly verified against the available in situ measurements on point-by-point base, and its spatial distribution and seasonality are compared with the satellite data. Observations of diurnal SST variability can be traced back to 1940s (Sverdrup et al., 1942; Roll, 1965). These early studies were based on in situ measurements from research vessels, which provided a robust and valuable source of high accuracy in situ SST observations. However, due to the limited geographic and temporal coverage of individual vessel measurements, this approach fell short of providing the continuous SST observations with a broader spatial distribution. This situation, however, was quite common in oceanographic research during that period. Since the 1980s, several international monitoring programs were developed, such as the Global Climate Observing System (GCOS) and the Global Ocean Observing System(GOOS)(Smith and Needler, 1995; Nowlin and Coauthors, 1996), the World Ocean Circulation Experiment (WOCE, Thompson et al., 2001) and the Tropical Oceans and Global Atmosphere /Coupled Ocean-Atmosphere Response Experiment (TOGA-COARE, Webster and Lukas, 1992). These programs applied operational satellites and surface-based monitoring systems to provide comprehensive, long-term and global observations. Although observing the SST variations diurnally was not a priority in most of these programs, measurements were collected at some mooring sites with time spans.

In particular, the TOGA Tropical Atmosphere Ocean Project/Triangle Trans-Ocean

Buoy Network (TOGA-TAO/TRITON), which emphasized climate variability in the tropical Pacific Ocean, produced accurate real-time SST and subsurface temperature measurement with moored buoy arrays, as well as surface wind, long-wave and shortwave radiation etc. Starting in the mid-1980s in eastern and central equatorial Pacific, the mooring array has been expanded to more than 120 buoys, covering the whole equatorial Pacific Ocean (TAO/TRITON, Hayes et al., 1991). Following the success of the TOGA-TAO program, similar in situ observational networks were developed in the Atlantic (Prediction and Research Moored Array in the Atlantic, PIRATA, Servain and Coauthors, 1998), and in the Indian Ocean (Research Moored Array for African-Asian-Australian Monsoon Analysis and Prediction, RAMA, McPhaden and Coauthors, 2009). The data collected from these mooring sites were available at a sample rate of one hour, or as high as ten-minute interval for some sites. Such high temporal resolution is sufficient to estimate diurnal SST variability and corresponding meteorological conditions more accurately. In this study, we have chosen some continuous time series of hourly SST measurements from several mooring sites to compare with the CGCM simulations.

As an example, a set of nine SST observations in year 2009 in the Indian, Pacific and Atlantic Oceans are shown in Fig. 3.1. A common feature of all time series is that significant diurnal signals are superimposed on the slower variations for the buoys positioned across three ocean basins, although the amplitudes of the diurnal SST signals fluctuate significantly, suggesting that the signals are intermittent and chaotic. Such intermittence of diurnal SST variability reflects the influences of local meteorological conditions, which also implies the interdependence of the SST variability between low and high frequency components. In order to concentrate on the diurnal variability, the diurnal anomalies were calculated by subtracting from original hourly observations its daily mean for each day (Fig. 3.2). From this, the relative strength and the episodic feature of SST diurnal cycle can be compared among the sites.
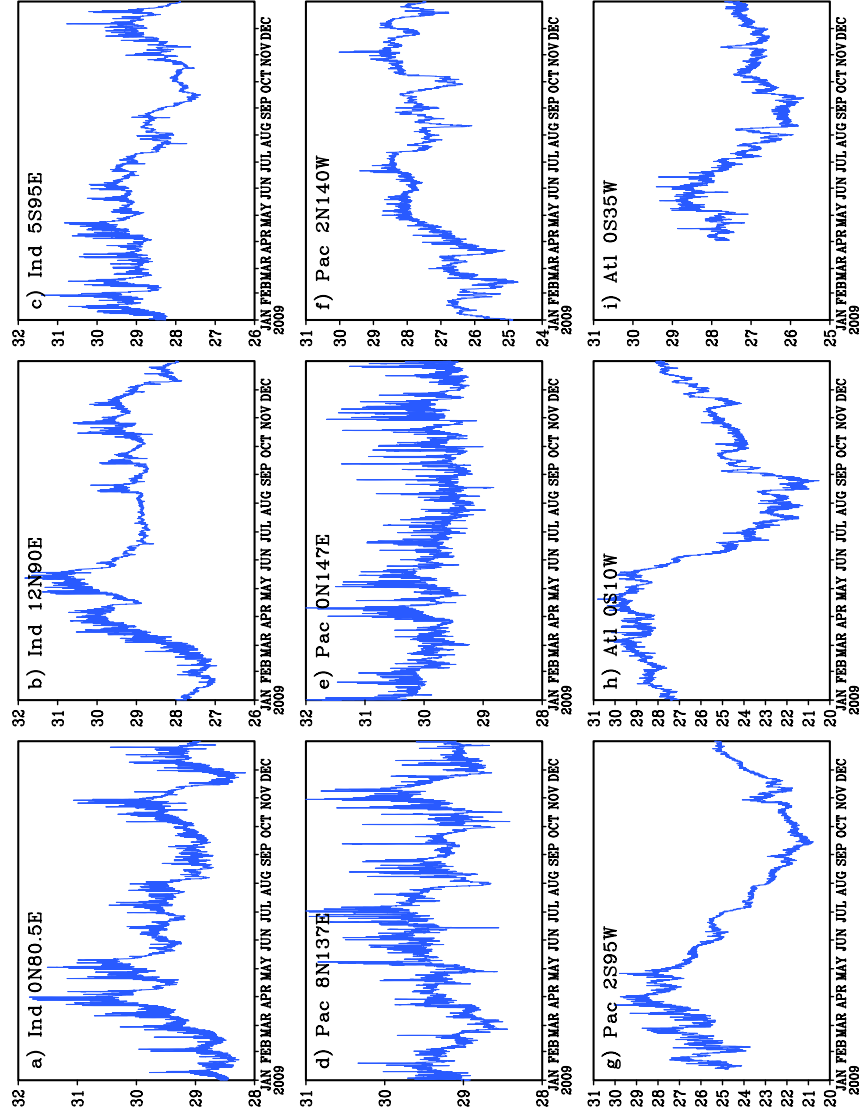
Figure 3.1. Real-time SST observations from nine selected TOGA mooring buoys in year 2009 to represent the typical seasonal and higher frequency SST variability in the Indian (a-c), Pacific (d-g), and Atlantic (h-i) Oceans. The unit of the SST is °C. The range of ordinate is chosen for each site to accommodate the amplitude of the local variability. Measurement is conducted at one meter depth. Sample rate is once per hour. Missing observations are left blank.

26
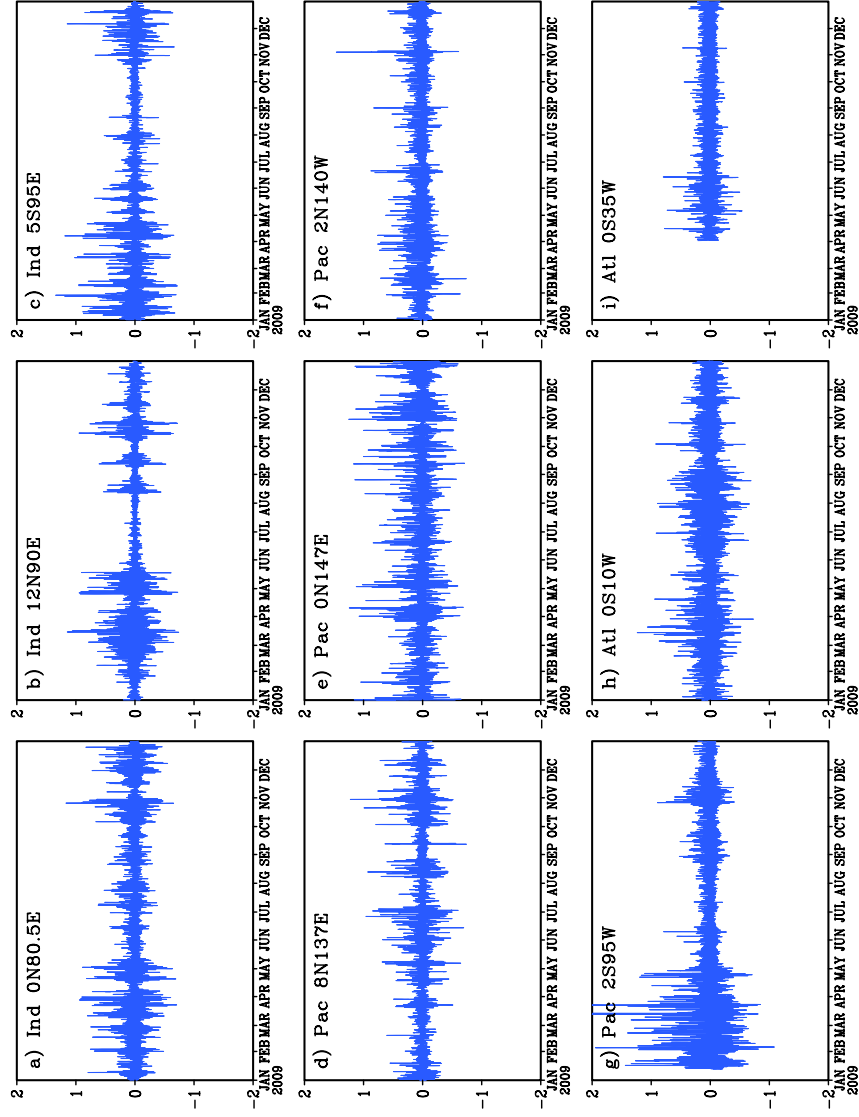
Figure 3.2. Diurnal anomalies calculated from the SST observations as in Fig. 3.1 to illustrate the high frequent variability with the period shorter than a day. The daily mean is removed from each site respectively. The unit is °C

Three sites are selected in Indian Ocean to the south of Sri Lanka on the Equator at 80.5^oE (Fig. 3.1a), within the Bay of Bengal at 12^oN, 90^oE(Fig. 3.1b) and to the west of Sumatra at 5^oS, 95^oE(Fig. 3.1c). The low-frequency variability of SST represents the significant influences of Indian summer monsoon winds in the region, especially for the site close to the subcontinent and the one within the Bay of Bengal. At these two locations, the SST gradually increased in the early spring from January to April before the monsoon outbreak (Figs. 3.1a, 3.1b). After reaching its maximum in late April to early May, the SST decayed rapidly and stayed at about 29^oC until September. For the site next to the Sumatra, the SST cooling can also be observed from June to September when the monsoon prevails (Fig. 3.1c). Besides the seasonal variations, the SST diurnal anomalies are also modulated by the strong wind and heavy precipitation brought by monsoon (Figs. 3.2a, 3.2b, 3.2c). For instance, the daily departures of SST are relatively small (less than 0.5^oC), even negligible for sites in the Bay of Bengal and west of Sumatra (close to 0.1^oC)(Figs. 3.2b, 3.2c), during the boreal summer season (June to September) when the monsoon dominates the Indian Ocean. On the other hand, the large diurnal anomalies, with value reaching or sometime exceeding one degree, occur during boreal winter and spring seasons (November to April). Such significant diurnal variability is associated with the seasonal warming during this period and relatively mild winds in the winter (Webster et al., 1998). In fact, these large anomalies appear consistently during a certain period but there are discontinuities between the diurnal warming events. Considering the site in the Bay of Bengal as an example (Fig. 3.2b), three significant daily departures are superimposed on the SST warming trend are periodically observed in mid-August, mid-September and mid-October. There are clear gaps in between these periods featured with small anomalies when SST cools down during the time (Fig. 3.1b).

The SST annual cycle is not as strong in the observational sites of the western Pacific warm pool and central Pacific (Figs. 3.1d, 3.1e, 3.1f). Here in particular, the SSTs remain at a warm stage with the mean temperature above 29^oC and varying no more than 2 degrees throughout the year. Correspondingly, SST diurnal anomalies had little seasonal

variability for all three sites (Figs. 3.2d, 3.2e, 3.2f). However, the amplitude of diurnal anomalies is larger in the warm pool than in the central Pacific. The the equatorial site (0^oN, 147^oE) within the warm pool consistantly has stronger anomalies compared with the site off the equator (8^oN, 137^oE). The relationship between diurnal anomalies and the tendency of the lower frequency SST change still holds, i.e., significant diurnal cycles are usually associated with SST warming tendency. For instance, for the site at 8^oN, 137^oE, large diurnal anomalies are concentrated in late June when the SST increases during that month, while suppressed diurnal anomalies accompany a general cooling trend of SST in July.

The sites selected in the eastern equatorial Pacific and equatorial Atlantic have notable annual cycle (Figs. 3.1g, 3.1h, 3.1i). The SST has a maximum value during the April-May period in the eastern equatorial Pacific(Fig. 3.1g), and May-June for the two sites in equatorial Atlantic(Figs. 3.1h, 3.1i). The minimum SST occurs from late August to middle of September for all three sites. A number of studies have discussed the mechanisms of the observed SST annual cycle in the eastern equatorial Pacific and Atlantic Oceans (Mitchell and Wallace, 1992; Xie, 1994; Liu, 1996). We will focus on the diurnal anomalies superimposed on the annual cycle (Figs. 3.2g, 3.2h, 3.2i). For the observations taken at eastern equatorial Pacific (Fig. 3.2g) and eastern equatorial Atlantic (Fig. 3.2h), anomalies with amplitude above 1 degree are often observed. An interesting fact is that the largest diurnal anomaly among all nine observations during January through May occurred in the cold tongue area (Fig. 3.2g) , with a maximum amplitude close to two degrees.

Overall, substantial diurnal SST variations superimposed on low-frequency variability are detected from in situ observations in tropical oceans. The seasonal conditions of the atmosphere and the ocean have great effects on the SST diurnal variability. In general, the diurnal signals generally have higher amplitudes while the background SST is increasing. Due to the effects of the atmospheric fluctuations, the diurnal signals of SST are intermittent and chaotic with variable amplitude.

3.2 A new diagnostic tool for extracting diurnal SST signals

Because the SST diurnal cycle is episodic, objective identification of the diurnal component from the total values becomes a non-trivial issue. Most of available data analysis methods, such as the spectrogram or the wavelet analysis, are essentially derived from the Fourier spectral analysis, which is a powerful tool to identify the periodic signal generated by the linear systems (Tichmarsh, 1948; Pinsky, 2002). However, the SST time series are non-stationary data that reflect the nonlinearity of the climate system. Fourier spectral analysis or similar methods are limited to process such data for several reasons. The Fourier spectrum gives a uniform harmonic components globally; consequently many "artificial" components are needed to thoroughly represent non-stationary data. Meanwhile, the periodic components tend to have constant amplitude, which is obviously not the case for the SST diurnal variability as we observed in the previous sections. Also, with Fourier spectral analysis using linear combinations of trigonometric functions, apart from harmonic components that capture linear fluctuations, additional harmonic components are required to simulate the nonlinear time series that does not strictly consist of sinusoidal waves. Other methods, such as the wavelet analysis that has alternative basic wavelet functions, still suffer from the same limitation. Moreover, considering the predetermined basic functions are only needed to fulfill the mathematical requirements of uniquely fitting the data, one cannot expect the decomposition to fully account for the underlying physics (Huang et al., 1998). Therefore, in this study we apply a novel data analysis method, the Ensemble Empirical Mode Decomposition (EEMD, Wu and Huang, 2009).

As an adaptive time-frequency analysis tool, the EEMD method is particularly suitable for identifying intermittent signals like the diurnal cycle. It is an extension of the original empirical mode decomposition (EMD, Huang et al., 1998). Being derived from the simple assumption that any data consists of simple unique oscillatory modes intrinsic to the data, the EMD is a completely posterior approach in regards to the decomposition of data into intrinsic modes and does not assume anything more about the data, contrary to Fourier methods for which data is assumed linear and stationary. Because basis functions

of EMD are derived directly from the signal itself, this adaptive analysis method has been shown numerically to better describe temporal patterns in non-stationary nonlinear time series than traditional methods such as Wavelet and Fourier methods (Huang et al., 1998). Furthermore, the technique is well localized in the time-frequency domain and is able to reveal important physical characteristics of the signal, because the decomposition is based on direct extraction of the signal associated with various intrinsic time scales. The efficiency of the technique is another advantage with the time series usually decomposed into a finite and often small number of modes.

The EMD method separates the locally fast oscillations from the slower ones through a reiterative extremes-connecting procedure. Given a time series $x(t)$, the EMD derives its oscillating modes by

1. Identify all local extremes of $x(t)$

2. Connecting neighboring maxima (minima) to form an upper (lower) envelope $\max(t)$ $(\min(t))$ of $x(t)$

3. Compute the average of the envelopes as $m(t) = (\max(t) + \min(t))/2$

4. Extract the locally high-frequency oscillation or detail as $d(t) = x(t) - m(t)$

5. Iterating steps 1)-4) until the mean of $d(t)$ has a magnitude smaller than a preset criterion. Then $d(t)$ is the highest oscillating mode of $x(t)$

6. Subtract $d(t)$ from $x(t)$ to derive the residual time series $r(t) = x(t) - d(t)$. Apply procedures 1)-5) to $r(t)$ to extract the second mode.

Repeating the above procedure allows one to derive modes of successively longer oscillating periods until the residual becomes monotonic in time, which can be considered as the trend of the time series.

Previous studies have demonstrated that EMD is effective in identifying episodic oscillating signals from time series of multiple scales (Huang and Attoh-Okine, 2005; Huang

and Shen, 2005). An EMD drawback, however, is the lack of mode stability, i.e., small perturbations to a time series can lead to qualitative differences between the extracted "modes". EEMD overcomes this problem with the so-called noise-assisted signal extraction. In essence, an ensemble of randomly perturbed time series is generated by adding white noise to the original time series, and an EMD analysis is conducted for each time series. Then, ensemble-means of the corresponding modes from all perturbed time series forms the EEMD modes. It has been shown that the EEMD modes are significantly more stable than the original EMD modes.

As an example, the diurnal mode and other components are extracted by EEMD for the hourly SST time series observed at Equator, 147°E during year 2009 (Fig. 3.3). Compared with the original time series (Fig. 3.1e), it is visually clear that EEMD is an effective way to identify the diurnal signal (Fig. 3.3b). The diurnal mode extracted by the EEMD is consistent with the daily anomalies computed in the previous section (Fig. 3.2e). The original data shows several periods with abrupt changes of SST, including a rapid increase from late March to early April then a sudden decay thereafter, with a similar pattern in May. These changes are reflected in diurnal mode as pulse signals. The diurnal mode also successfully reflects the intermittence of the diurnal SST variability, and the strong signal is often interrupted by periods of several days with negligible amplitudes. Besides the diurnal mode, low frequency variability of synoptic-scale (less than 10-day, Fig. 3.3c) and intraseasonal-scale (30-60-day, Fig. 3.3d) are also successfully identified with EEMD. The relationship between the diurnal variation and slower-changing variability (Fig. 3.3d) is evident with strong diurnal signals always accompanied by the SST warming tendency. Such a relationship is consistent with the results we draw from the previous section, but it is illustrated more clearly and objectively with EEMD modes.

The power spectrum analysis reveals that each component extracted with EEMD has a dominant peak on the spectral map indicating the distinct period of each mode (Fig. 3.4). The notable diurnal peak is comparable with the result of a spectrum analysis on diurnal anomalies (Fig. 3.2e), proving that the EEMD gives a clean extraction of the diurnal
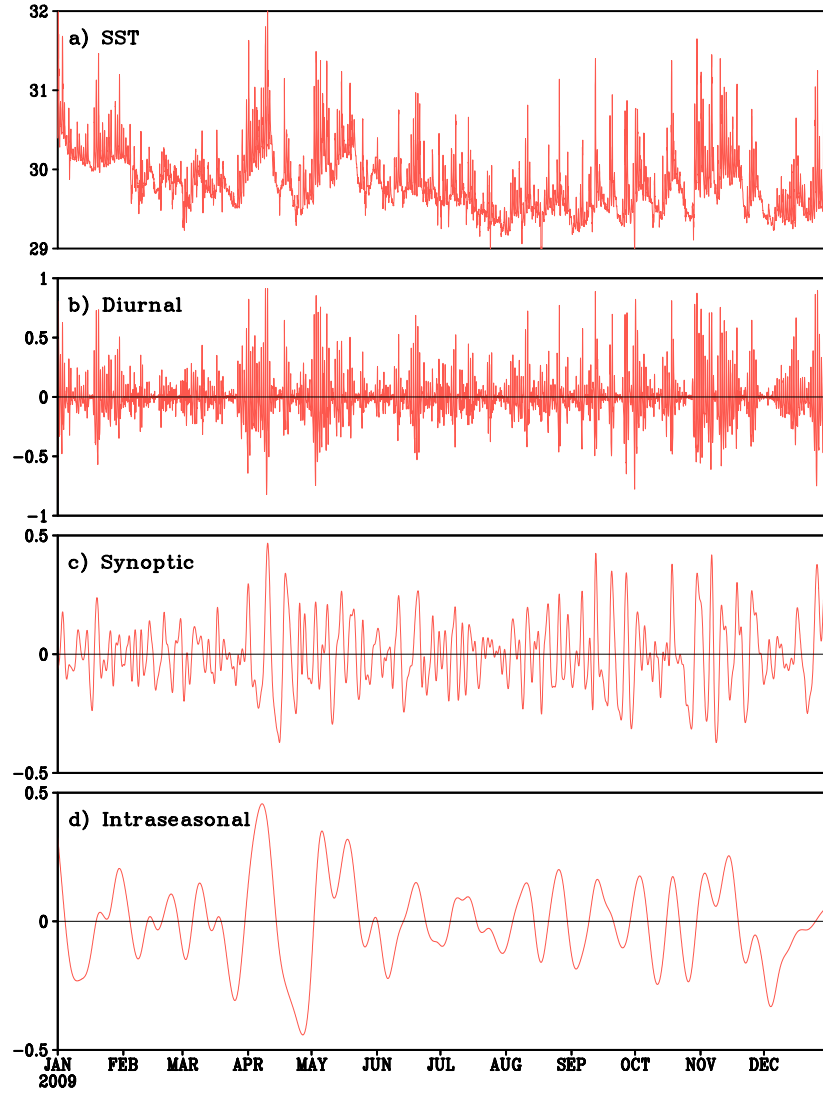
Figure 3.3. Ensemble Empirical Mode Decomposition (EEMD) on the hourly SST observation (unit: ^{o}C) at equator, 147°E in year 2009 (a, as in Fig. 3.1e). The components of the variability on diurnal (b), synoptic(c), and intraseasonal (d) time scales are displayed. The range of diurnal variability is -1.0 to 1.0 ^{o}C, and -0.5 to 0.5 ^{o}C for other two components.
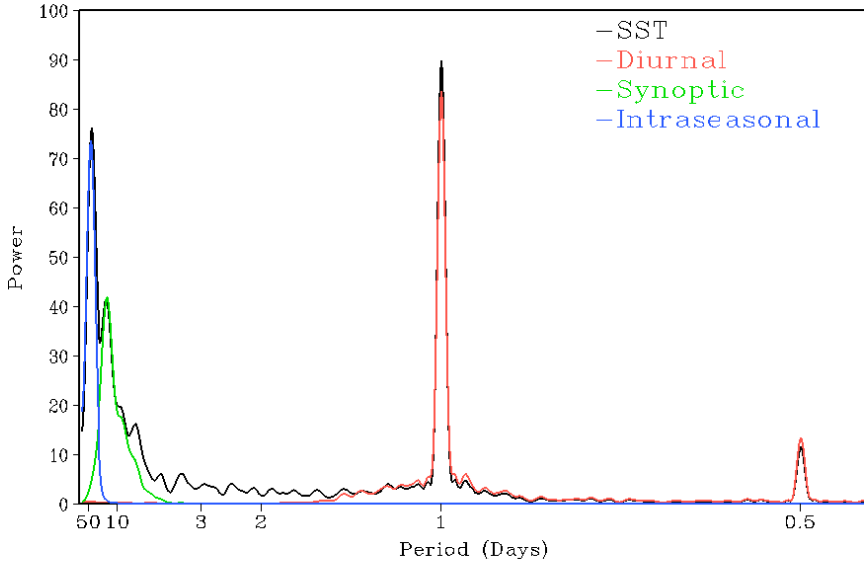
Figure 3.4. Power spectra of SST time series (black), and its diurnal (red), synoptic (green) and intraseasonal (blue) components extracted by the Ensemble Empirical Mode Decomposition (EEMD) on hourly SST observation at site 0°, 147^oE.

signals. Therefore, using EEMD, we are able to objectively identify episodes of high and low diurnal amplitude. Both diurnal and intraseasonal modes are oscillatory signals, and the relatively large spectral power of these two modes demonstrates that a large portion of SST variability is contained at the diurnal and intraseasonal (30-60-day) time scales. Whether there are cross-scale feedbacks between them and how they interact with each other, further investigation is needed.

3.3   Simulated SST diurnal variability

After examining the observed SST variability, the diurnal cycle of SST in the CFS simulations is evluated. In this aspect, we apply the EEMD method that has been successfully used before to decompose the simulated SST at a single model grid point (Fig. 3.5). As an example, we select a one-year SST time series in the eastern Indian Ocean at 5^oS, 95^oE (Fig. 3.5a). The general pattern of seasonal variability of SST is well captured by the model

34
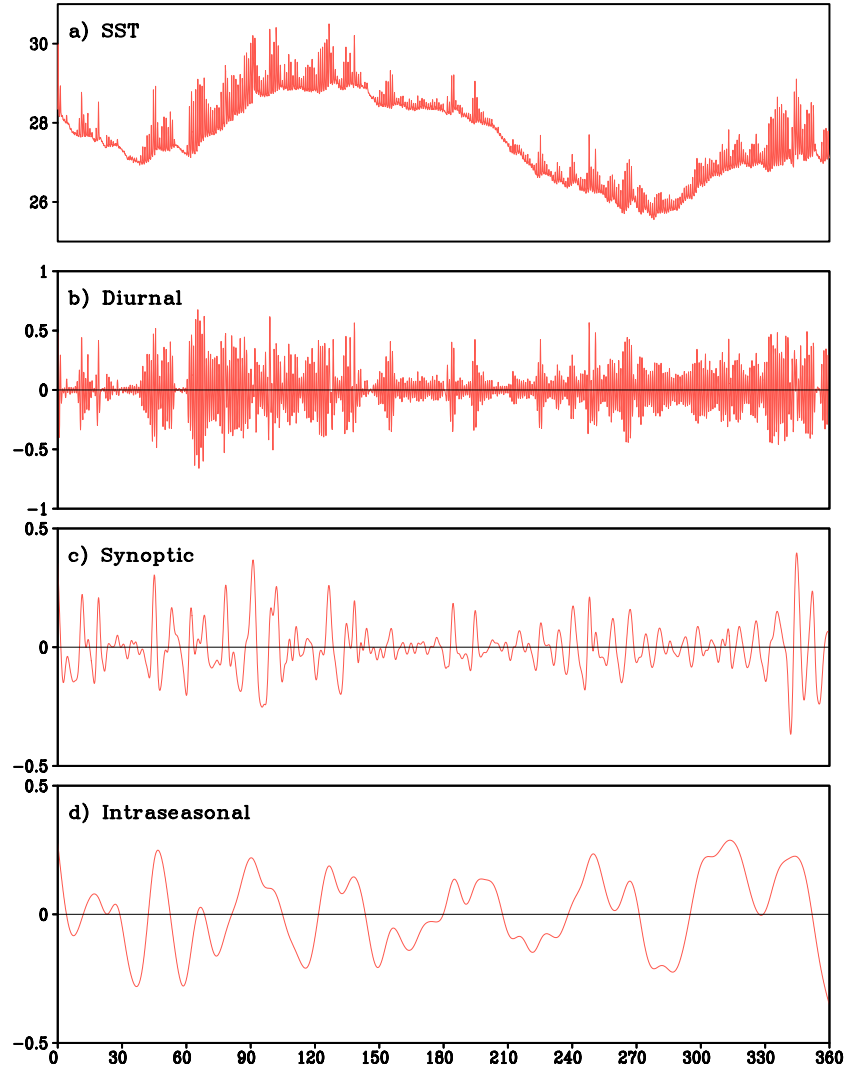
Figure 3.5. EEMD on simulated SST from ZB experiment at model grid point 5ºS, 95ºE (a, unit: ºC). The length of SST time series is one year. The model generated SSTs at 3-hour interval. The diurnal mode (b), synoptic mode (c), and intraseasonal mode (d) of SST variability are shown.
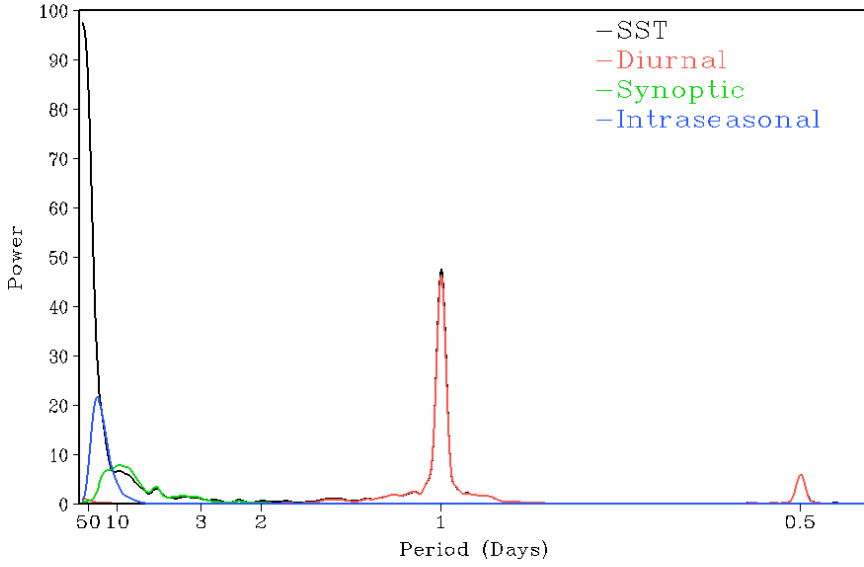
Figure 3.6. Power spectra of SST time series (black), and its diurnal (red), synoptic (green) and intraseasonal (blue) components extracted by the Ensemble Empirical Mode Decomposition (EEMD) on simulated SST from ZB experiment at grid point 5ºS, 95ºE.

comparing with the observation at the same location (Fig. 3.1c). On top of that, the significant diurnal variability is superimposed, which is successfully extracted by diurnal mode of EEMD (Fig. 3.5b). The diurnal mode contains the essential features of SST diurnal cycle such as its amplitude and intermittence. The synoptic and intraseasonal signals are also identified in simulated SST (Figs. 3.5c, 3.5d): the association of the large diurnal variation with warming tendency is still effective here. All of these modes have distinct periods as indicated in the power spectrum map (Fig. 3.6), but the oscillation of diurnal component is more significant than that at the intraseasonal scale at this grid point.

3.3.1 Diurnal mode of simulated SST at single point

Based on the previous analysis of observed SST from moorings, although the largest diurnal amplitude of SST is observed over cold tongue area from boreal winter to spring, enhanced SST diurnal variability also tends to occur in the Indian Ocean and in the western equatorial Pacific where there is relatively high SST on average throughout the year and

active atmospheric variability at intraseasonal time scales. Therefore, we are most interested in the simulated SST diurnal cycles in the Indian Ocean and western Pacific area.

In the warm pool, the SST observation positioned at Equator, 147^oE is selected as the reference of evaluation. The original observation time series (Fig. 3.1e) and its corresponding diurnal mode (Fig. 3.7e) isolated with EEMD are shown in Fig. 3.7. For the model experiments (ZB, SG and CTL), one-year SST time series (the 10th model year) are picked at the model grid point closest to the observation site (Figs. 3.7b-d). The EEMD is applied and only diurnal modes are shown (Figs. 3.7f-h). The simulated time series successfully captures the essential temporal features of the SST in the warm pool, such as insignificant annual cycle and high mean temperature, aspects that agree well with the observation.
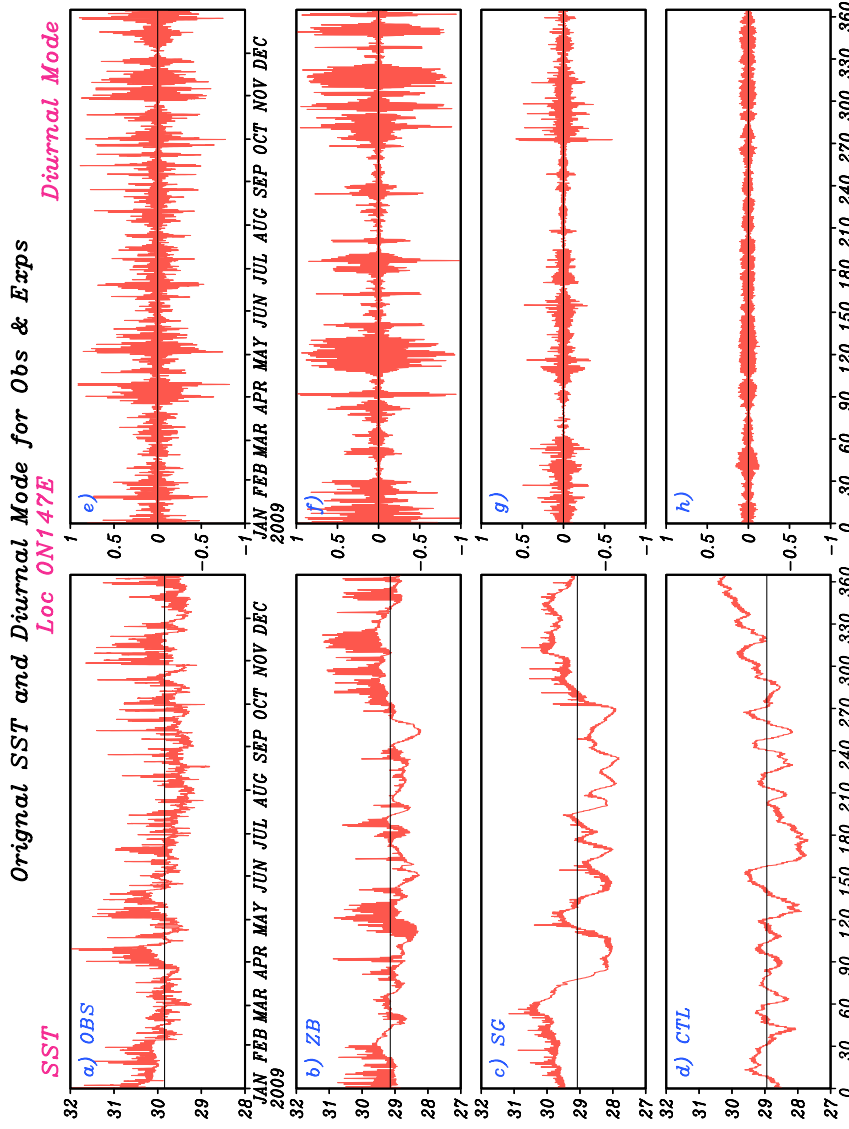
Figure 3.7. SST time series of the observation at western equatorial Pacific (site: 0° 147°E, unit:°C) in year 2009 (a, as in Fig. 3.1e) and its diurnal mode extracted with EEMD (e, as in Fig. 3.3b) picked as references to evaluate the model simulations of diurnal SST variability. One year simulated SST (unit: °C) from experiments ZB(b), SG(c), and CTL(d) selected at model grid point 0°, 147°E. The corresponding diurnal modes extracted with EEMD are in right column (f-h).

More importantly, both experiments with the implementation of diurnal mixed layer parameterizations have significant improvement on SST diurnal cycle (Figs. 3.7f, 3.7g) while the amplitude of SST diurnal variability is unrealistically small in the CTL run (Fig. 3.7h). Between the two sensitivity experiments, the ZB scheme is much more effective and produces the strength of diurnal cycle that has maximum value around 1^oC, comparable with the observation. The SG scheme tends to underestimate the amplitude of diurnal cycle with largest amplitude at about half a degree.

In comparison with the observation, the intermittence of the diurnal signal is also represented by ZB and SG experiments. Several periods are featured with persistently large SST diurnal cycle and are separated by gaps with suppressed diurnal variability. Such temporal irregularity is caused by the local meteorological conditions as pointed out previously in the observations. To investigate if this mechanism is correctly reproduced in the model simulation, a chunk of 30-day diurnal variability of the observation and experiments is displayed in Fig. 3.8 together with the corresponding surface wind and incoming solar radiative flux. Both ZB and SG parameterizations reflect the correct phase relationship between SST diurnal cycle and incoming solar radiation. The maximum SST during the daytime appears several hours after the peak of solar radiation, as confirmed by the observations. The parameterizations also correctly respond to the surface wind variation, with stronger wind suppressing diurnal variability, such as that during the period from day 5 to day 17 in the ZB experiment and the period from day 21 to day 30 in the SG experiment. This response of the diurnal cycle to the wind is consistent with the observation. For example, from May 26th to 30th the strong wind reduces the amplitude of the observed SST diurnal cycle although there is no significant change of solar radiation. The wind speed primarily dominates the amplitude of SST diurnal cycle for two reasons: On one hand, stronger wind induces the enhanced heat flux (mainly latent heat flux) from ocean to atmosphere and inhibits the SST increment (Weare et al. 1981). On the other hand, stronger winds cause stronger entrainment of cold water, which also reduces the diurnal warming (Price et al., 1978).

39
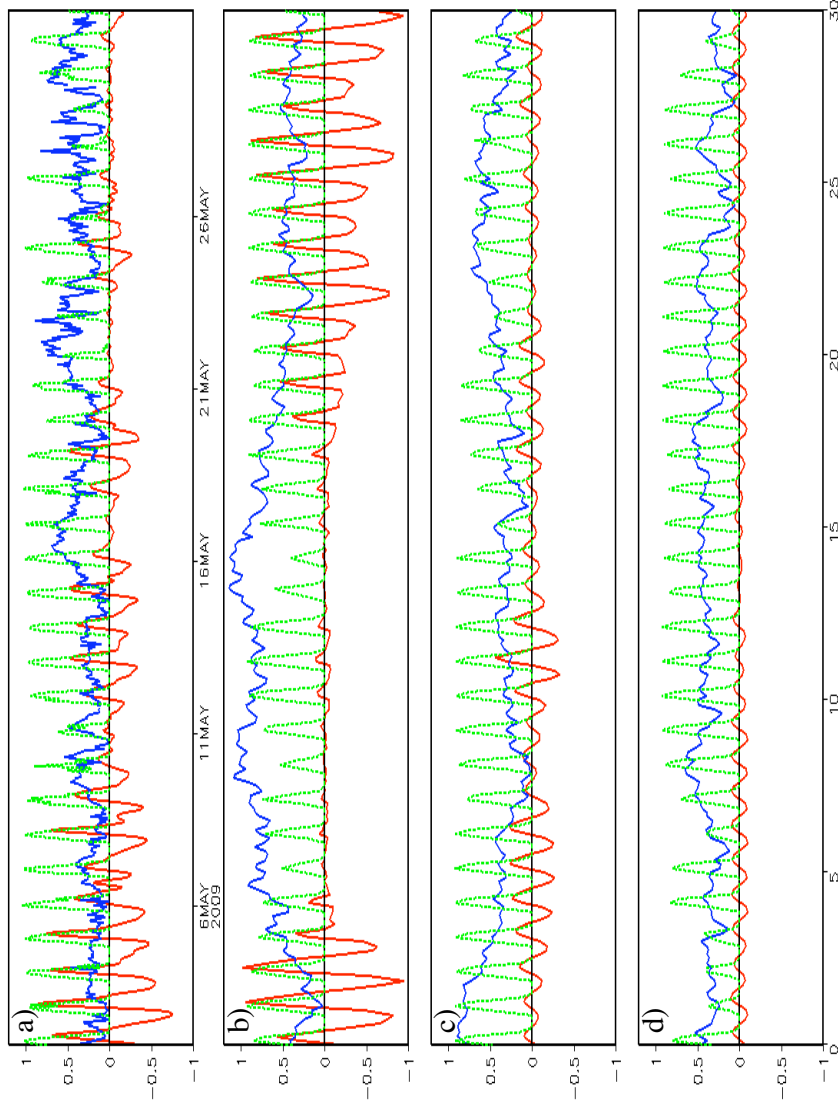
Figure 3.8. Diurnal modes of SST variability (red solid) extracted from a) observation at 0°, 147°E, b) ZB experiment at grid point near the observation, c) SG experiment, and d) CTL experiment. Corresponding net solar radiation (green dot, unit: 10^3 W m^{-2}) and surface wind speed (blue solid, unit: 10 m s^{-1}) were shown.
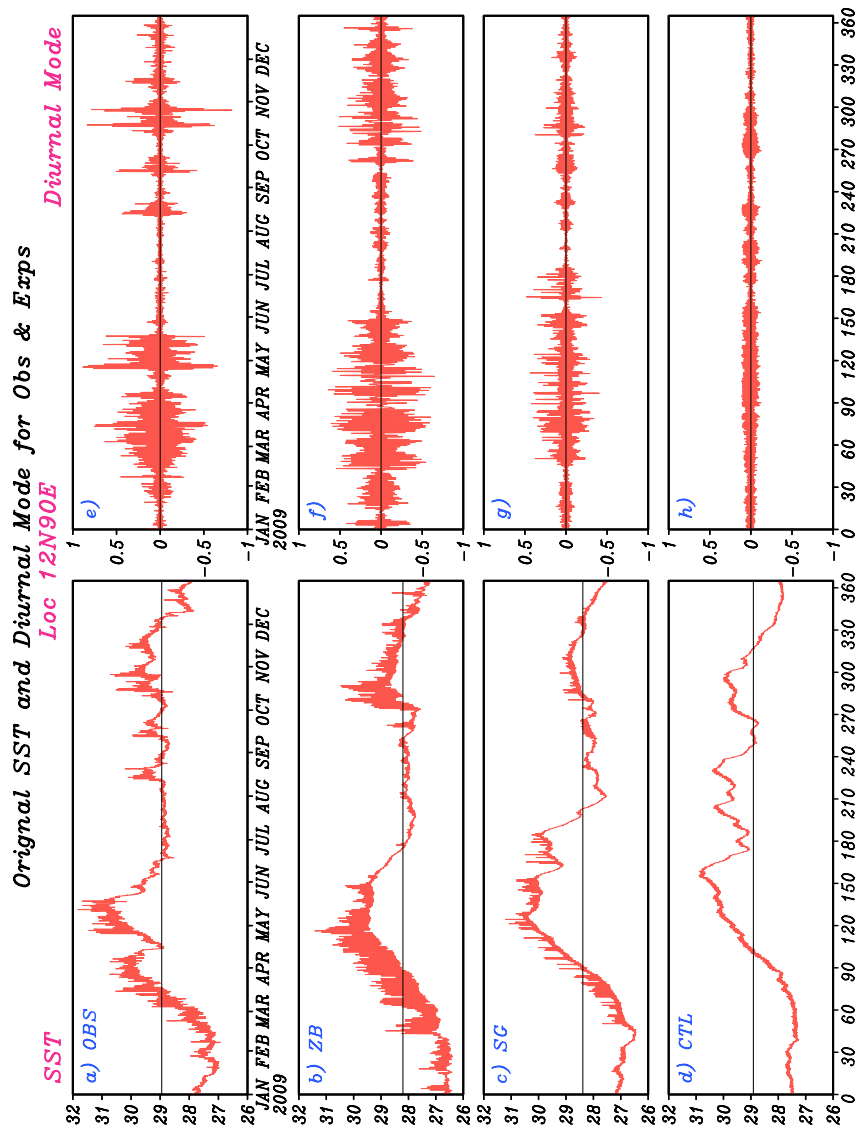
Figure 3.9. As in Fig. 3.7 but for the point in the Bay of Bengal (site: 12°N, 90°E).

Another location in the Bay of Bengal (12°N,90°E) is selected to evaluate the SST simulation in the Indian Ocean (Fig. 3.9). All experiments reproduce the seasonal variability of SST to a large extent in comparison with the observation (Fig. 3.9a). The diurnal variability has been improved largely in ZB (Fig. 3.9f) and SG (Fig. 3.9g), relative to the CTL run(Fig. 3.9h), by applying mixed layer parameterizations. In particular, the ZB scheme gives a realistic estimation of the amplitude of the SST diurnal cycle, while SG scheme underestimates the variability. The signature of the Indian summer monsoon can be observed in the ZB and SG simulations, especially for the diurnal modes. Such modulation featured the suppressed diurnal cycle during the boreal summer due to the enhanced wind and reduced solar radiation (associated with intensified convection), for example, occurs from June to September in ZB and from July to October in SG. The response of SST diurnal variability to the monsoon is also evident that two parameterizations can correctly reflect influences from both the solar radiation and the winds.

3.3.2 Annual mean of the diurnal SST variability in the simulations

It is clear that diurnal mixed layer parameterizations indeed realistically generate the major characteristics of the SST diurnal variability in the model. In particular the ZB scheme has a more realistic amplitude, as indicated in the point-to-point comparison between the observation and the model simulations. In this section, we further investigate the spatial distribution of the mean condition of the simulated SST diurnal variability. For this purpose, we define the amplitude of diurnal SST variability (DSST hereafter) as the difference between SST of the daytime maximum value and the nighttime minimum at each ocean grid point in the experiments.

The annual mean DSST field, averaged over the entire twenty-year simulations for each run, clearly indicates regions with substantial amplitude of diurnal variability (Fig. 3.10). Significant diurnal warming of SST was found throughout most of the tropical oceans in the ZB experiment (Fig. 3.10a). Large DSSTs above 0.7^{o}C are distributed in the northern Indian Ocean, the equatorial Pacific, the eastern equatorial Atlantic, as well as several

coastal regions, such as the western Central America and northwest Australia. DSST values exceeding 1.1^{o}C are also shown in some regions such as the eastern equatorial Pacific and coastal western Central America. Areas of low DSST are generally located in subtropical open oceans between 15°N-20°N except for the Atlantic, where the low DSST regions also extend into the western tropical Ocean close to the western boundary (Fig. 3.10a). The SG experiment produces a similar spatial pattern to that in the ZB experiment, except that the amplitude of the diurnal variability is about the half the magnitude(Fig. 3.10b). In particular, relatively strong diurnal warming is concentrated in the eastern equatorial Pacific and Central America coast with values up to 0.7^{o}C. This is consistent with the results of comparison at selected locations presented in the previous sections. Globally, the spatial distribution of DSST mean state in the ZB and the SG experiments is highly comparable with the observations shown in Clayson and Witlich (2007, their Fig. 9a). In particular, the ZB experiment reproduces the consistent magnitude of DSST over the tropics and subtropics.

The CTL also has some characteristics of the DSST distributions as shown in the two sensitivity runs, such as the generally enhanced diurnal cycle in the equatorial oceans and some coastal areas. The striking difference between the CTL and the other two runs, however, is that the magnitude of DSST is substantially smaller in the former. For the CTL run (Fig. 3.10c), there is no significant diurnal warming for most of the ocean, with DSST generally less than 0.1^{o}C. Even along the equator the day-night differences are less than 0.3^{o}C, while the corresponding values are around 1.1^{o}C in the ZB experiment. These results show that, without a proper parameterization of the diurnal mixed layer, the current configuration of the OGCM cannot resolve the diurnal variability adequately even if the incoming solar radiation contains diurnal variability. More specifically, fully resolving the diurnal mixing processes in the ocean mixed layer is necessary to represent SST diurnal variability. Values of daily peak shortwave radiation (SWR, Fig. 3.11a) and daily averaged wind speed (WND, Fig. 3.11b) show patterns consistent with the DSST distribution. High values of peak SWR located along the equatorial Pacific with the maximum peak in the
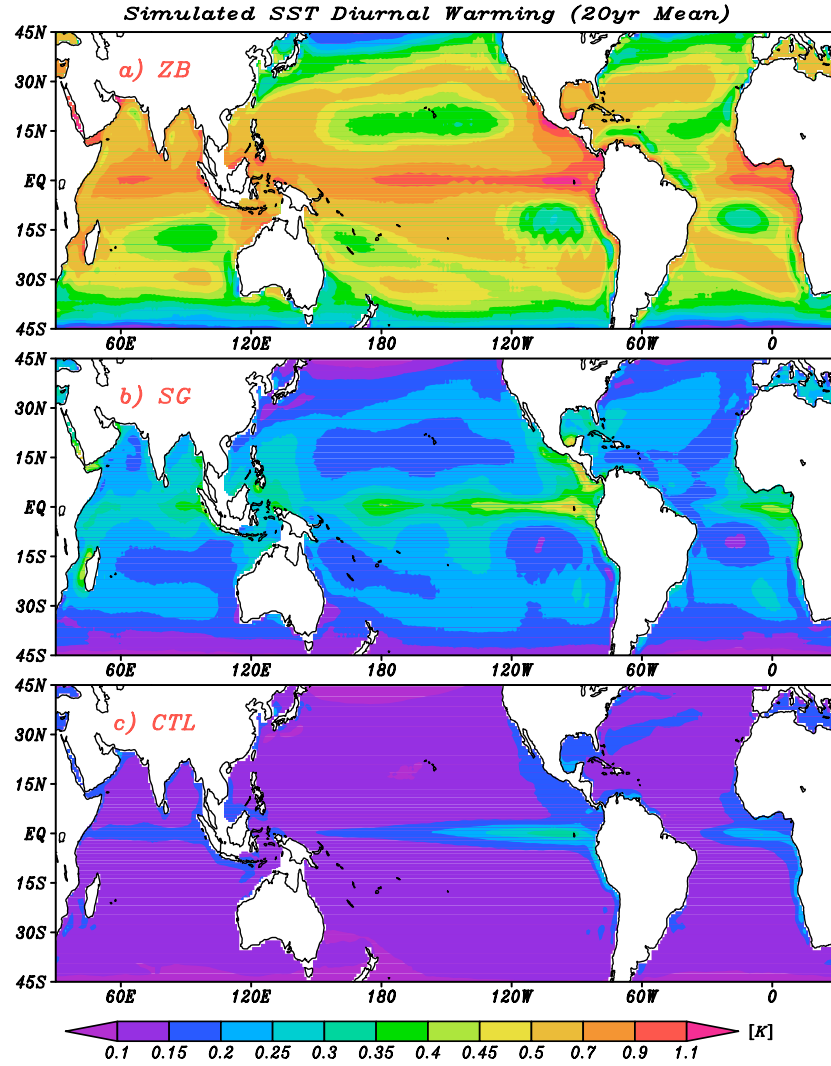
Figure 3.10. The amplitude of the SST diurnal cycle (DSST, defined as the difference between local daytime peak SST value and nighttime SST minimum values) averaged over 20-year simulations for (a) ZB , (b) SG, and (c) CTL. Colors are consistent among experiments.
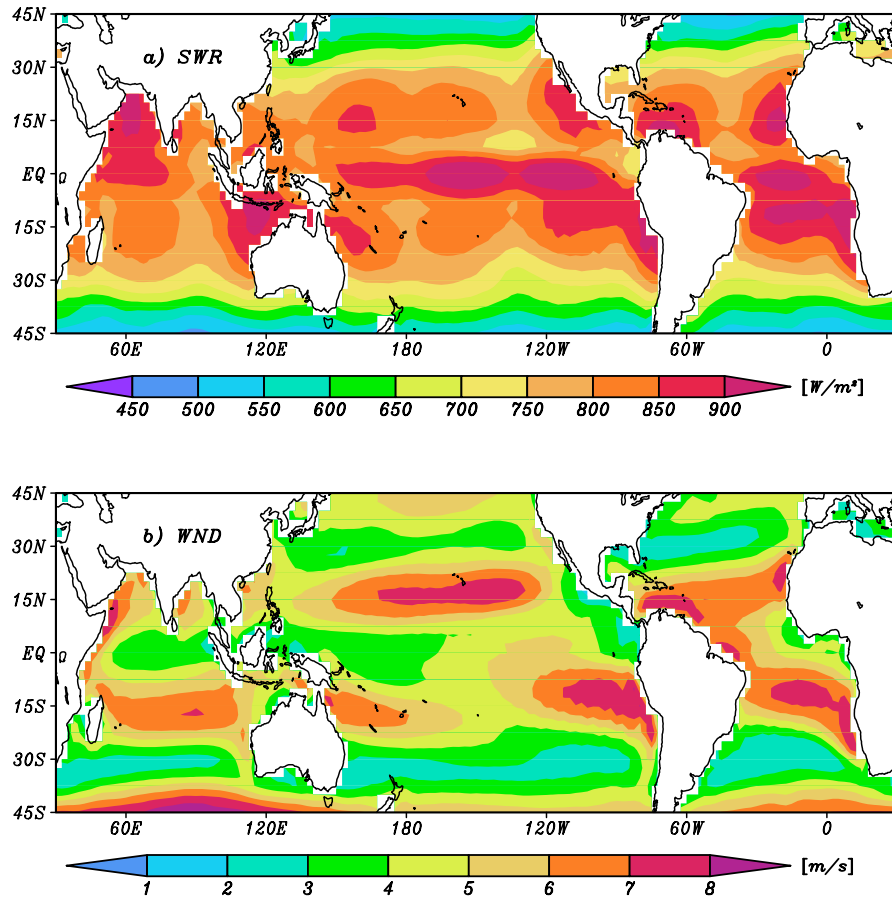
Figure 3.11. 20-year average of (a) daily peak shortwave radiation and (b) daily averaged 10-meter wind speed from the ZB experiment to investigate the meteorological conditions corresponding to the mean DSST distribution. The patterns of solar radiation and wind speed are similar in other two experiments (Figures not shown).

eastern and central Pacific. These high values of peak SWR cause larger average DSST values, which is obvious in both ZB and SG experiments, since the peak SWR determines the maximum value of the SST warming during the daytime and therefore contributes to the magnitude of the DSST. The strong diurnal change of solar insolation also contributes to the diurnal warming in the Arabian Sea and several coastal areas. However, most variation of DSST is best explained by the wind speed variability across the basins. This is due to the fact that, throughout the tropical regions, peak solar radiation shows relatively small variation in the range from 700 W m^{-2} in subtropics to above 900 W m^{-2} along the equator (Fig. 3.11a). Wind speeds, however, may change from 3 m s^{-1} (e.g., equatorial Indian and Western Pacific, west of central America) to 9 m s^{-1} (e.g., tropical central Pacific and southeast Pacific) in the tropical oceans. Therefore, the large variability of wind contributes to a greater portion of the variability in diurnal warming. The average wind speeds are less than 5 m s^{-1} in areas where high average DSST values (above 0.7^oC in ZB and above 0.35^oC in SG) are located, while wind speeds greater than 7m s^{-1} are associated with weak diurnal warming in the places such as tropical north-central Pacific, southeast part of tropical Pacific, south Atlantic Ocean, etc. The coherent patterns are consistent with results of Soloviev and Lukas (1997) and Donlon et al. (2002). They found that the diurnal variability of SST vanishes under windy conditions based on in situ observations. Gentemann et al. (2003) showed from TMI SST data that the diurnal variation clearly depends on solar radiation and wind speed.

3.3.3 Seasonal mean of the diurnal SST variability in the simulations

Observational studies have shown that the amplitude of diurnal SST variability has significant seasonal dependence (Stuart-Menteth et al., 2003; Kawai and Wada, 2007; Clayson and Weitlich, 2007). The seasonal cycle of the DSST is shown in the twenty-year averages for ZB (Fig. 3.12) and SG (Fig. 3.13) experiments respectively. In general, the diurnal variation is relatively large in the tropics through the year for both experiments. However, it is strongest from boreal winter to spring in the eastern part of equatorial Pacific and

Atlantic Oceans when the local SST is warmer. Deser and Smith (1998) and Clayson and Weitlich (2005, 2007) also indicate that the diurnal SST amplitude has a local maximum over the cold tongue in the eastern equatorial Pacific. To a lesser extent, the winter-spring enhancement of the DSST also occurs in the equatorial Indian Ocean. This seasonality can be explained by the seasonal change of the regional wind and net solar flux. Since the incoming solar radiation has a strong semi-annual cycle on the equator, March is one of the seasons when the incoming solar radiation is strongest locally. In addition, local winds are generally weak at this time because the ITCZ is closest to the equator. On the other hand, although the solar radiation is enhanced again on the equator in September, the local wind speeds are larger due to the strong trade winds, which tend to suppress the amplitude of diurnal SST change (Horel, 1982; Phillander and Chao, 1991; Mitchell and Wallace, 1992; Carton and Zhou, 1997).

Globally, the strongest seasonal contrast in DSST occurs in the subtropical oceans between the boreal summer and winter. Specifically, large day-night SST difference appears along 30^oS in austral summer (DJF, Figs. 3.12a and 3.13a) and appears in the northern hemisphere during the boreal summer (Figs. 3.12c and 3.13c). It is no surprise that the large diurnal variability occurring in the subtropics are under the atmospheric subtropical highs, which favors clear sky and weak surface wind conditions. Seasonally, the net solar radiation is strongest in summer. All these factors favor enhanced SST diurnal variability in the subtropical oceans during summer in both hemispheres. In addition, the whole North Indian Ocean also experiences strong seasonal change of the DSST. In boreal spring before the Indian monsoon, the DSST is enhanced throughout the basin. In particular, the day-night difference in the Bay of Bengal and the Arabian Sea becomes largest, reaching a maximum value at 1.2^oC for ZB (Fig. 3.12b) and 0.5^oC for SG (Fig. 3.13b). In this season, due to the relatively clear sky, the incoming solar radiation is strongest, which raises the net surface heat flux into the northern Indian Ocean to the level between 75 and 100 W m^{-2} in comparison with the 10-20 W m^{-2} in the western Pacific with deep convective clouds (Loschnigg and Webster, 2000). It is apparent that the strong incoming solar heat flux
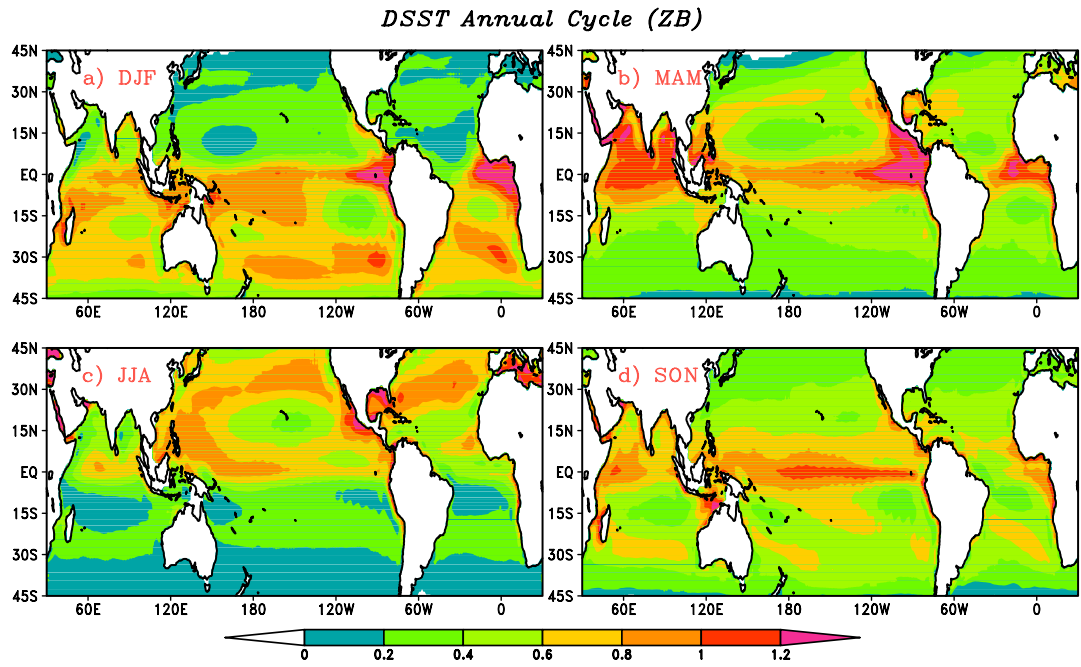
Figure 3.12. Average DSST values for (a) DJF, (b) MAM, (c) JJA, and (d) SON based on 20-year simulation of the ZB experiment to illustrate the seasonal variation of DSST in tropical and subtropical oceans. The range of DSST is set from 0°C to 1.2^{o}C at interval of 0.2^{o}C
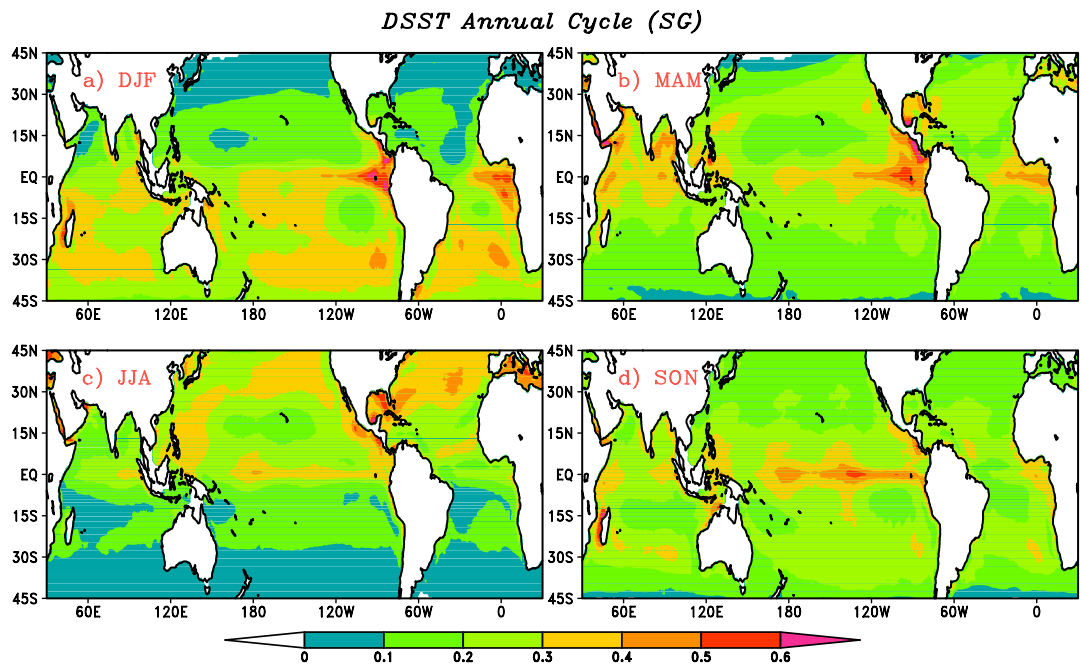
Figure 3.13. As in Fig. 3.12 but for SG experiment. But the range of DSST is set from 0°C to 0.6^{o}C at interval of 0.1^{o}C.

with its own strong diurnal cycle drives the DSST. Whether the strong diurnal cycle of the SST during the pre-monsoon season has any feedback to the upcoming rainy season is a topic worth further examination. The diurnal variability is suppressed in boreal summer (Figs. 3.12c and 3.13c) as the outbreak of Indian summer monsoon induces strong tropical convection and increased surface wind speed. This temporal evolution is consistent with the analysis of TOGA/TAO buoy observation (seen in the previous section) that revealed the relationship between the Indian monsoon and diurnal SST variability. Diurnal warming is enhanced again in the northern Indian Ocean from September to November (SON) in both runs (Figs. 3.12d and 3.13d), though at lesser magnitudes than their MAM counterparts. The SON enhancement of the DSST is related to the suppressed phase of monsoon in autumn when northern Indian Ocean has similar meteorological conditions including clear sky and relatively small wind speed, similar to the spring inter-monsoon but with weaker incoming radiation (Dickey et al., 1998).

Stuart-Menteth et al. (2003) first showed the global distribution of the day-night SST difference using six years of AVHRR SST data. They reported the large DSST in the tropics through the year, and the strong diurnal warming in subtropics associated with the high-pressure system. Seasonal variations of DSST were also observed in the Indian Ocean and the western Pacific warm pool related to the seasonal migration of the monsoon. In particular the noticeable warming appeared in the warm pool, and the northern Indian Ocean around April and October due to the Indian spring inter-monsoon and autumn inter-monsoon, respectively. Kawai and Wada (2007) also revealed consistent characteristics of the spatial distribution and seasonal variation of the day-night SST difference based on AMSR-E dataset. They also pointed out the significantly strong DSST in the eastern equatorial Pacific, which reaches a maximum in boreal spring and a minimum in boreal autumn. All of these spatial and temporal features of the DSST seasonal variability are adequately represented in the model simulations. Both parameterization schemes show the capability to respond to the seasonal variation of the atmospheric conditions.

3.3.4   EOF analysis of the diurnal SST variability in the simulations

Using a regression equation, Clayson and Weitlich (2007) have created a dataset consisting of daily SST diurnal warming values from 1996 through 2000 covering the global tropics. The inputs to the equation include the peak solar radiation from International Satellite Cloud Climatology Project (ISCCP) data and daily averaged wind speed from Special Sensor Microwave Imager (SSM/I) data. The dataset provides an observation basis to evaluate the model simulations.

Based on the analysis of diurnal sea surface temperature of Webster et al. (1996), Clayson and Curry (1996) suggest a regression equation to calculate the amplitude of diurnal SST variability (DSST) that uses the variables including peak insolation, daily averaged wind speed, and daily averaged precipitation:

$$\text{DSST} = f + a(PS) + b(P) + c\ln(U) + d(PS)\ln(U) + e(u) \tag{3.1}$$

where PS is the peak solar insolation (W m^{-2}), U is the daily averaged 10-m wind speed magnitude(m s^{-1}), and P is the daily averaged precipitation (mm h^{-1}). The coefficients a through f are determined differently for low wind speed ($U < 2$m s^{-1}) and high wind speed ($U > 2$m s^{-1}).

When reconstructing a diurnal SST dataset (Clayson and Weitlich 2007), the precipitation term is set to zero because the complete precipitation field is not available. They argue that the precipitation has the smallest influence on the SST diurnal cycle: According to the Webster et al.(1996) calculations, the maximum effect on DSST will be about 0.3^{o}C under most influential conditions of high precipitation and low winds.

To better visualize the spatial patterns of DSST fluctuation on seasonal and longer time scales in the simulation, an EOF analysis of the reconstructed DSST field is performed for the Indian, Pacific and Atlantic Oceans, respectively (Clayson and Weitlich, 2007). Similarly, we conduct an EOF analysis on 20-year DSST data from ZB experiment to evaluate the model performance. The leading EOF modes and a portion of principle components

(From 6th to 10th model year) will be compared with the results from DSST dataset of Clayson and Weitlich.

The Indian Ocean

The three leading EOF modes of the ZB experiment for Indian Ocean basin are shown in Fig. 3.14. The spatial pattern of the first mode (Fig. 3.14a) has the same sign across the basin. Its time series (Fig. 3.14b) shows that the strongest daytime warming occurs around March and April and second peak around October and November while the DSST values are at the minimum from May to August. Such pattern is consistent with the seasonal mean state of DSST in the previous section that indicates the enhanced DSST appearing twice during boreal spring and fall (Figs. 3.12b, 3.12d), while a suppressed pattern appears during boreal summer (Fig. 3.12c). The temporal variability reflects the influence of Indian summer monsoon at different phases. As we discussed before, the reduced solar insolation due to active convection and strong surface wind for the prevailing monsoon in boreal summer leads to a decline of DSST. While in the suppressed phase of the monsoon (boreal spring and autumn), the clear sky associated with the strong incoming shortwave radiation and relatively low wind speed favor significant diurnal SST variability. The first mode of simulated DSST over Indian Ocean shows the similar pattern with those of the reconstructed data on both spatial distribution and the time evolution (Fig. 13 from Clayson and Weitlich, 2007). The notable difference of the simulation from the reconstructed data is that model overestimates the DSST variation over the area south of the equator crossing the basin, particularly in the region north of the Madagascar. In the contrast, the variation in the Arabian Sea and the Bay of the Bengal is less significant. The model biases of the SST mean state, especially a significant warm bias in the southwest part of the Indian Ocean most evident during boreal winter season, may contribute to the southward shifting of the DSST variation. The details of the mean state errors will be discussed further in the next chapter.
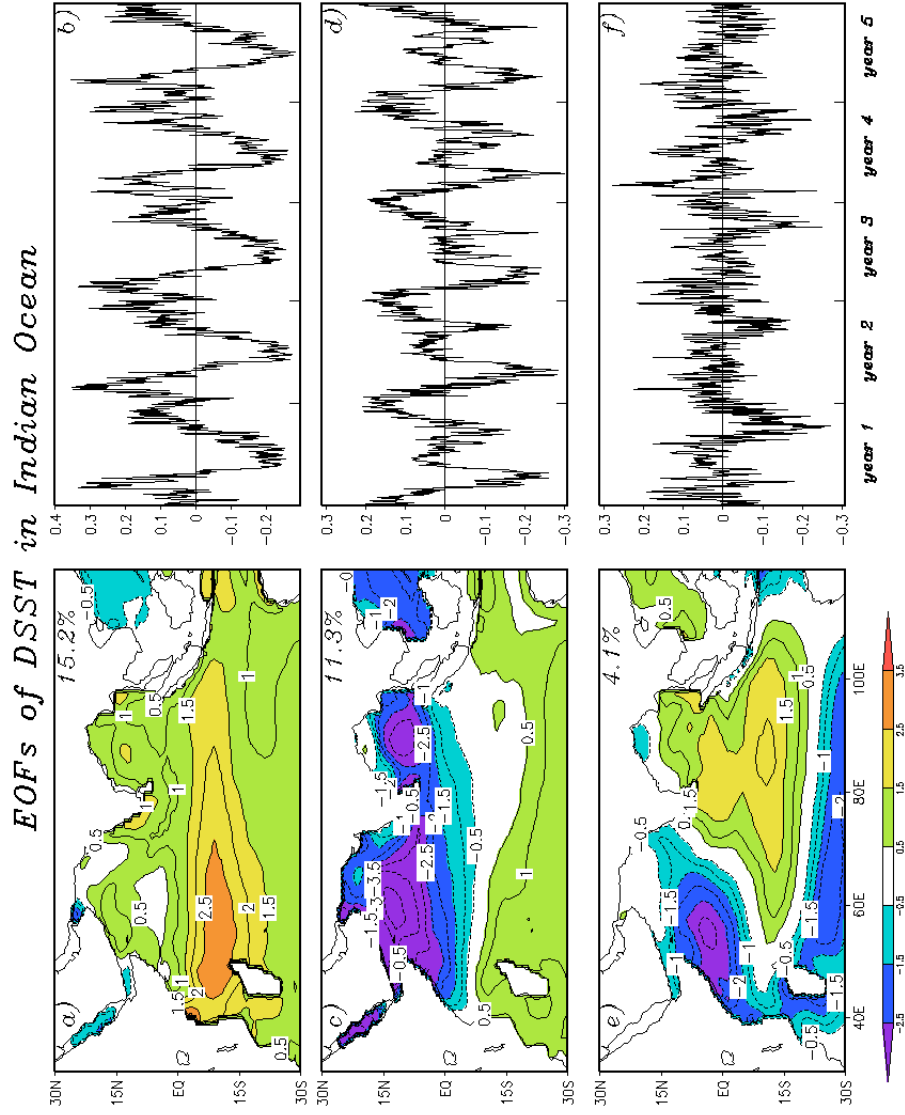
Figure 3.14. Leading EOF spatial patterns and principal components for (a), (b) mode 1. (c),(d) mode 2. and (e), (f) mode 3 in the tropical Indian Ocean. EOF analysis is conducted on 20-year DSST from ZB experiment. A 5-year-length portion of total 20-year principle-component time series is selected.

53

The second mode (Fig. 3.14c) features a general asymmetry between the northern and southern hemispheres. Its time series (Fig. 3.14d) is characterized by both annual and semi-annual components, showing that the DSST in the northern ocean is at its minimum (maximum) during boreal winter (spring), while a pair of secondary peak (weak DSST over northern ocean) and trough (strong DSST over northern ocean) appears in boreal summer and fall. The seasonal contrast of the incoming solar radiation that features strong annual and semi-annual cycles in tropics primarily determines the spatial distribution of DSST. Meanwhile Indian monsoon may also play secondary role in modulating the amplitude of DSST semi-annually, especially during boreal summer. Compared with the corresponding mode of the reconstructed data, the seasonal contrast of the DSST is well simulated by the model. It successfully represents the magnitude of the variation, as well as the relatively stronger DSST variability in northern Indian Ocean, is successfully represented by the simulation. Meanwhile, the model shows sensitivity to the semi-annual cycle of the solar radiation, which is reflected as the secondary peak and trough in the time series of the mode. Such feature is not clear in the reconstructed data.

The third mode (Fig. 3.14e) shows an east-west dipole pattern that the positive weights are found in the eastern Indian Ocean near the Sumatra and the negative weights with the higher magnitude are around the African coast. The periodic signature of the third time series is not so clear as those of the other modes, but generally positive coefficients dominate in the first half of the year and negative coefficient occur around the latter half of the year. Therefore around the first six months the higher diurnal SST variability tends to appear in the eastern basin accompanied by lower variability in the western part, with the pattern reversing in the last six months (Fig. 3.14f). On top of the variation within a year, the time series also shows some year-to-year fluctuations. For instance, in comparison with the other years, the 2nd and 5th year of the selected period show the reduced DSST variability, especially during the latter half of the year. The east-west dipole also occurs in mode 3 of reconstructed DSST with the similar temporal variation as shown in the simulated DSST, but the centers of DSST variation are more constrained along the equator

in the reconstructed data, while the DSST variation in the simulation has spread south of the equator and formed an additional center in the eastern Indian Ocean. The southward shifting of DSST variability may be related to the mean state bias of SST in the basin.

The spatial pattern of DSST displays the similar variability of a longer interannual dipole mode of SST found in the tropical Indian Ocean, the so-called Indian Ocean dipole (IOD, Saji et al., 1999). The positive phase of IOD is an anomaly with cooler than average SSTs in the eastern Indian ocean off the west coast of Sumatra and warmer than average SSTs in the western Indian Ocean with associated convection and precipitation. The negative phase of the IOD reverses the SST gradients, and therefore greater convection and precipitation forms over the warmer waters of the eastern Indian Ocean. The IOD tends to have biennial tendency tied to monsoon ocean feedback (Wang et al., 2003). The SST gradient along the equator associated with the different phases of IOD has contradicting effects on the diurnal SST variability. On one hand, the above-average SST is favorable condition for strong variation of SST from day to night as seen in the TOGA buoy observations, but enhanced convection may inhibit daytime warming of SST due to the decreased incoming solar radiation. Thus, the overall effects of IOD on the dipole mode of DSST need to be diagnosed in a future study.

The Pacific Ocean

For the Pacific Ocean, the seasonal contrast mode (Fig. 3.15a) explains the most variance of DSST over the basin which has mostly negative weights dominated the northern hemisphere and positive weights over the southern hemisphere. The corresponding principle component (Fig. 3.15b) shows the positive coefficient from October to March and negative from April to September, indicating above-average DSST values in the northern hemisphere and below-average DSST values in the southern hemisphere for boreal winter, with the opposite ocurring for boreal summer. The pattern is consistent with the seasonal variability of the DSST mean state from boreal winter to boreal summer (Figs. 3.12a, 3.12c) and reflects the influence of annual cycle of solar radiation as discussed previously. Some

features of spatial distribution of DSST are also captured in this mode, such as the high DSST variability that often occurs in the region from western to middle equatorial Pacific, especially over the Maritime Continent, as well as the large variability in eastern Pacific cold tongue area. The weak DSSTs are found in tropical north-central Pacific and southeastern Pacific area due to the large local wind speed (Fig. 3.11b). All these characteristics revealed in the first EOF mode are highly comparable with the mode 1 of the reconstructed (Fig. 14 of Clayson and Weitlich, 2007). The first EOF mode of simulation fully represents the seasonal contrast of DSST in the Pacific Ocean on both magnitude and spatial/temporal variations.
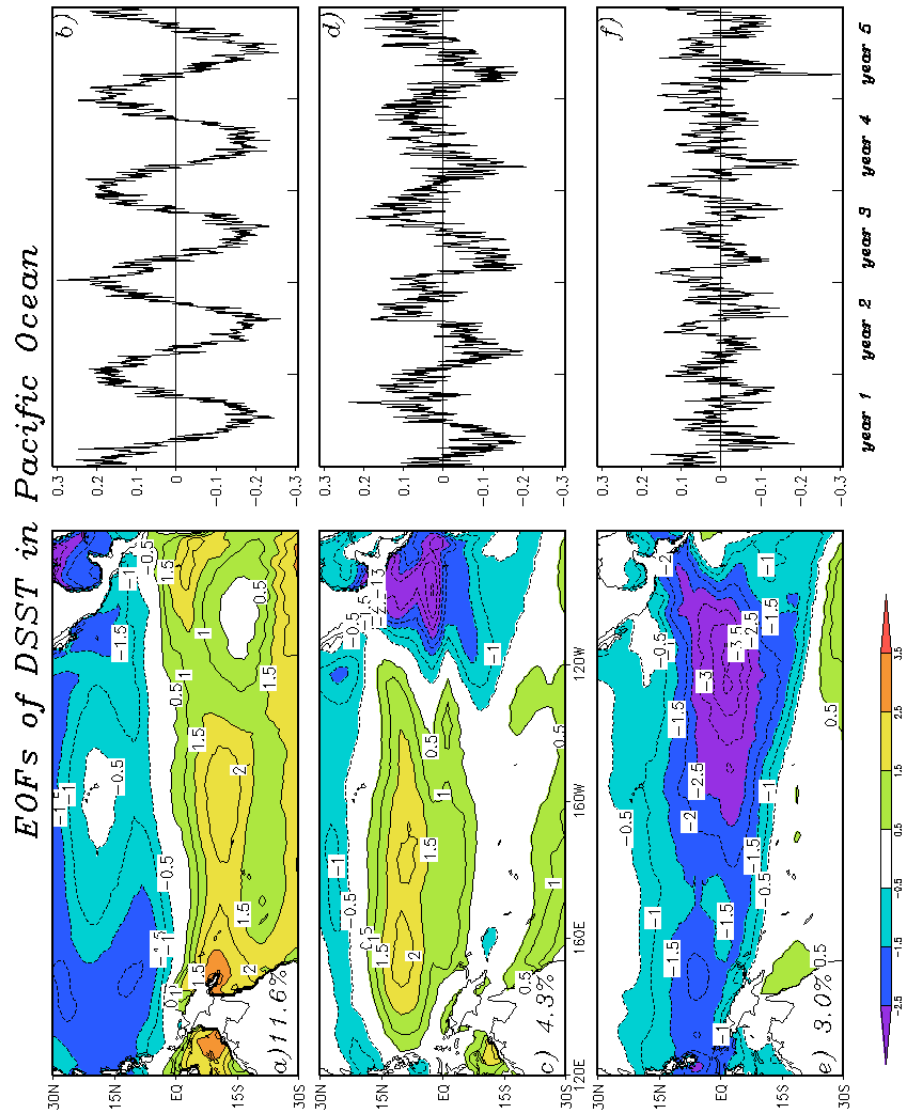
Figure 3.15. As in Fig. 14 but for tropical Pacific Ocean.

An east-west dipole pattern is observed in the third EOF mode of the simulation (Figs. 3.15e, 3.15f), and a similar structure appears in the second mode of reconstructed DSST. The spatial pattern has strong negative weights in the eastern Pacific and positive weights extending from the western to the central Pacific. Combined with the principal-component time series, the dipole mode shows that the above-average DSST is located in the eastern Pacific and below-average DSST in western Pacific in the first half of the year, and a reversed pattern appears in the later half of the year.

Compared with the dipole mode in the reconstructed DSST, the simulation shifts the center of strong DSST variability to the north of the equator in the western Pacific. Meanwhile, the DSST variation over the cold tongue area shows a wider spatial extent in the eastern Pacific and less extension to the west along the equator compared to the reconstructed data. Such differences may relate to the mean state biases of the CFS model such as the warm biases in the eastern Pacific, etc., which is discussed in the next chapter.

The DSST dipole mode in the Pacific can be modulated by the ENSO patterns. The analysis of Cronin and Kessler (2002) (Who used buoy data from the eastern Pacific) shows that in an El Nio year the Eastern Pacific has increased SSTs in cold tongue but reduced diurnal warming from winter to the next spring. Oppositely, for La Nia years, the diurnal warming increases in the cold tongue from the winter to spring. The opposite trend in DSST compared to SSTs for ENSO is mainly due to the variations in the solar radiation and wind speeds associated with the different phases of ENSO. During a La Nia year, maximum trade winds and deep convection shift westward, resulting in clear skies and relatively weak winds and consequently large SST diurnal cycle in the eastern equatorial Pacific. During El Nino, the reverse occurs. Further investigation is needed to confirm such interannual variability of DSST in our simulations.

The second mode of experiment (Figs. 3.15c, 3.15d) shows similarity with the mode 3 of reconstructed data, except that the DSST variation is shown over a much broader area in the experiment due to the mean state biases of SST. This mode indicates the tendency for the DSSTs to follow the same variation in most of tropics with the largest variation in the

eastern Pacific. The semi-annual cycle of the trend can be observed in its time series (Fig. 3.15d). The above-average DSST in tropical Pacific tends to occur twice around March and September, respectively. As seen in the previous section, the semi-annual cycle of the solar radiation in the tropical area contributes to this pattern.

The Atlantic Ocean

EOFs modes of the Atlantic Ocean (Fig. 3.16) are similar to those of the Pacific. The first mode (Figs. 3.16a, 3.16b) represents the seasonal contrast of DSST variability, featuring the asymmetry patterns in northern hemisphere and southern hemisphere. Its principle component shows a clear annual cycle with little interannual variation, indicating a greater SST diurnal variability in Northern (Southern) hemisphere during boreal summer (winter). The pattern is consistent with the seasonal variation of the DSST mean state (Figs. 3.12 and 3.13), and it is comparable with the reconstructed DSST (Fig. 12 of Clayson and Weitlich, 2007) although the simulation overestimates the magnitude of the DSST variability in the eastern Atlantic Ocean, possibly related to the warm SST model biases in the region. The second mode (Figs. 3.16c, 3.16d) shows DSST with the same sign in almost the entire Atlantic, and the time series shows no clear period of the variation. A similar pattern also appears in the reconstructed data. Such a DSST pattern might reflect the influences of atmospheric variability on the multiple timescales such as the semi-annual cycle of solar radiation and the migration of Atlantic ITCZ, but the mechanisms need further study.
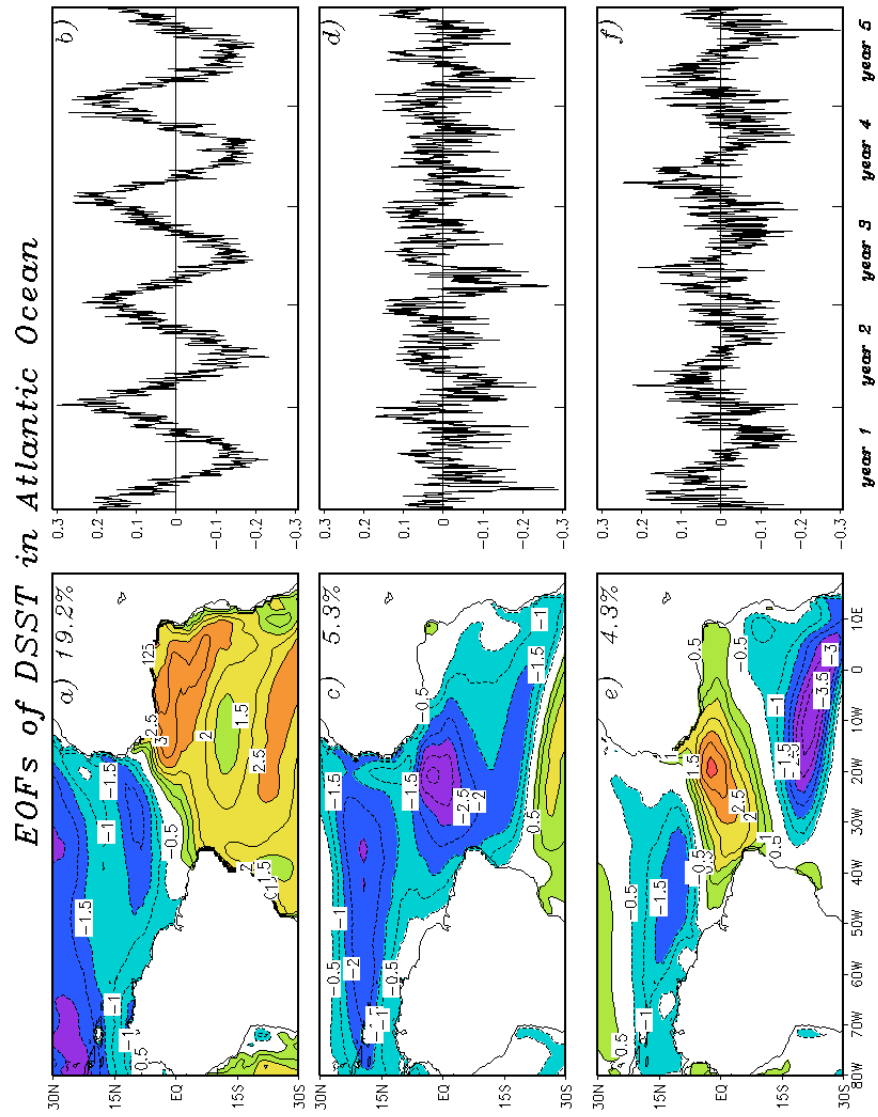
Figure 3.16. As in Fig. 14 but for tropical Atlantic Ocean.

A triple mode is shown as the spatial pattern of the third EOF in Atlantic Ocean (Fig. 3.16e) with positive weights centering at equatorial eastern Atlantic and extending westward throughout the equatorial region. Lower magnitude negative weights are found northwest along 15°N, and stronger negative weights lie in the 15°S to 30°S band. The principle component (Fig. 3.16f) shows a general annual cycle, with the coefficients that are usually positive from February to May and negative in boreal summer (JJA). Accordingly, the SST diurnal variability in equatorial eastern Atlantic is weakened during boreal summer, because of the outbreak of the Western Africa monsoon in this season. In the boreal summer intense heating of the Sahara creates a meridional pressure gradient from the Gulf of Guinea to the Sahara, and the associated westerly jet with the maximum wind speed exceeding 7 m s^{-1} dominates the region and causes the small values of DSST (Carlson, 1969; Grodsky et al., 2003).

The south subtropical Atlantic SST anomalies (SSA, Huang et al., 2004) pattern may affect the DSST pattern over the 15°S to 30°S. Based on the mode 3 time series (Fig. 3.16f), the DSSTs over south subtropical Atlantic have smaller values in the austral summer and fall while the SSA pattern (positive SST anomalies) is significant during the period (Huang and Shukla, 2005). This opposite trend in DSST compared to SSTs in south subtropical Atlantic is similar to the relationship of DSST and SST in the eastern Pacific for ENSO.

3.4 Summary

In this chapter, we have evaluated the SST diurnal variability of the model simulations from several aspects. The point by point comparison between model results and TOGA buoy observations is conducted, and the diurnal mode of SST variation is extracted by employing a novel data analysis method which is efficient and suitable for non-stationary nonlinear data such as SST time series. The results indicate that the SST diurnal variability shows great improvement in the experiments with the diurnal mixed layer parameterizations compared with the CTL run. In particular, the ZB experiment produces a diurnal cycle

with realistic amplitude very similar to the observations.

The annual mean and seasonal variation of the amplitude of the diurnal SST (DSST) are investigated. The experiments show the coherent spatial distribution and temporal variation, except that the magnitude of DSST is different due to the selection of the different parameterization schemes. More importantly, compared with the satellite observations and reconstructed DSST based on observations, the critical features of diurnal SST have been well reproduced in the experiments. These features reflect the influences of the local meteorological conditions with the solar radiation and surface winds as the dominant factors. The agreement between the model simulations and observations proves that the parameterizations, once implemented in a coupled model, are able to correctly resolve the physics that determine the SST diurnal variability.

Notably, through EOF analysis, we observe patterns of diurnal SST variability that are related to some interannual variability patterns of SSTs, such as the IOD in the Indian Ocean, ENSO in the Pacific Ocean and subtropical Atlantic SST anomalies. These connections imply the possible modulation or even feedback between DSST and SST on longer time scales. It is worth further investigation of the interaction between the SST diurnal cycle and climate variability on different time scales. We also notice that the model mean state may have a significant influence on the simulation of the diurnal SST variability in particularly its spatial distribution. It is necessary to estimate the CFS model bias and its potential influences.

Chapter 4: The influence of SST diurnal variability on the mean states

Diurnal SST variation is strongly affected by meteorological conditions as we discussed in the previous chapter. On the other hand, many previous studies suggested the diurnal SST variation significantly affects the properties and processes of the atmosphere. Webster et al. (1996) pointed out the change of 1^oC in SST can lead to an 27 W m^{-2} change in the net surface heat flux in the tropical western Pacific. Dai and Trenberth (2004), using a fully coupled climate system model without the diurnal SST variation, indicated that simulated diurnal cycles in surface air temperature, pressure and precipitation over the oceans were much weaker than the observed values. They inferred that the lack of the diurnal cycle in SST was a significant deficiency in current climate models. Slingo et al. (2003) suggested the possibility that the diurnal SST rise may act as a trigger for the shallow cloud convection. Li et al. (2001) performed numerical experiments using a global atmospheric model with and without the diurnal variation of SST. They found that, for the intraseasonal variability, the phase relationship between surface flux and precipitation simulated with diurnal SST variations were closer to the observed one in the warm pool region during COARE than that simulated without the diurnal SST varations. The diurnal SST also brought an increase in the tropical precipitation, especially over the Indian and the western Pacific Oceans, although the increase was no more than 10%. Using the buoy measurements from the TAO array, Deser and Smith (1998) found that the mean diurnal amplitude of SST showed a local maximum over the cold tongue in the eastern equatorial Pacific and suggested that it may generate a diurnal cycle of the wind divergence near the equator. These previous studies demonstrated that the diurnal SST variability affects significantly the atmospheric circulation on different spatial and time scales. However, as far as we know, there has not

been a systematic analysis on the potential effects of the diurnal SST variability on the mean climate state and its major variability.

In Chapter 3, we have demonstrated that the SST diurnal variability can be successfully simulated in the CFS model with the parameterizations of the diurnal mixed layer near the sea surface. In this chapter, we will discuss the influence of the diurnal SST on the mean climate over the tropical oceans and the interannual variability. We will further discuss its potential effect on the intraseasonal occillation over tropical oceans in Chapter 5. Our discussion proceeds as the following: In next section, we will present a general description of the mean climate simulated by the CFS control run (CTL), with an emphasis on the model systematic errors through a comparison between the CTL and observations. Section 2 investigates the impact of the diurnal SST variability on the mean state by comparing the CTL and the experiments with parameterized oceanic diurnal mixed layer. Section 3 further discusses its influence on the interannual variability in the eastern Pacific, the ENSO variability.

4.1   CFS model biases

As shown in the Chapter 3, although the diurnal SST variability is significantly improved in the sensitivity experiments, some inconsistency of the spatial distribution of the diurnal SST is still observed over certain areas in the simulations by comparison with the available observations. For instance, the diurnal SST variability is overestimated in the western Indian ocean near Madagascar (Fig. 3.14a). We believe that such errors may relate to the biases of SST mean state in the simulation. Therefore, its necessary to thoroughly investigate the model biases of different variables in the experiments, which can help us to correctly evaluate the influences induced by the diurnal SST variability. On the other hand, we expect the sensitivity experiments with the diurnal SST variability can provide a rectification of the model biases to some extent because the interactions between atmosphere and ocean are supposed to be more realistic by considering the diurnal cycle of SST. For these purposes, we will briefly describe the CFS model biases of the CTL run in the rest of

the section

A general discussion of the CFS mean error has been given by many previous studies (Saha et al., 2006; Wang et al., 2005; Zhang et al., 2006; Pegion and Kirtman, 2008). These error patterns also exist in our CTL experiment, which increases the coupling frequency to a 3-hour interval. We will summarize the model mean state biases of fields including sea surface temperature, precipitation and 850hPa wind by comparing the model results with observations.

The large-scale features of the observed tropical SST is captured by model simulation (Fig. 4.1b) in comparison with OISST (Fig. 4.1 a) (Optimum Interpolation Sea Surface Temperature, Reynolds, 1988, 1993; Reynolds and Marsico, 1993; Reynolds and Smith, 1994), such as the comparable magnitude and spatial pattern of the warm pool in the Indian and the western Pacific Oceans, and the eastern-western gradient of SST in the Pacific and Atlantic Oceans. However, SST biases are seen in the tropics and subtropics (Fig. 4.1c) which is defined as the difference between the average of the 1981-2000 OISSTs and the 20-year average of the CTL run. For example, the model shows the largest warm biases reach about 2-3°C over the eastern Pacific cold tongue area. This is a common problem among the coupled GCMs and is likely due to weak equatorial zonal winds, the insufficient stratus clouds over the southeastern Pacific, weak coastal upwelling, and unresolved eddy transport near the eastern coast (e.g. Mechoso and Coauthors, 1995; Pegion and Kirtman, 2008; Manganello and Huang, 2009; Pan et al., 2010). A similar error pattern prevails in the eastern Atlantic cold tongue region, as also described by Huang et al. (2007) and Hu et al. (2008). Meanwhile, the cold biases tilting poleward from western to central tropical Pacific in northern and southern hemispheres are apparent in the simulation. The magnitude of cold biases is generally 1°C, except for the northern Pacific where there is a cold bias of larger than 1°C. There are also large errors in the Gulf Stream region, which are likely due to insufficient resolution of the ocean model. All of these biases are evident in the CFS forecast with 6-month lead shown by Saha et al. (2006)

The errors of simulated precipitation are evaluated by comparing the 20-year (1981-2000)
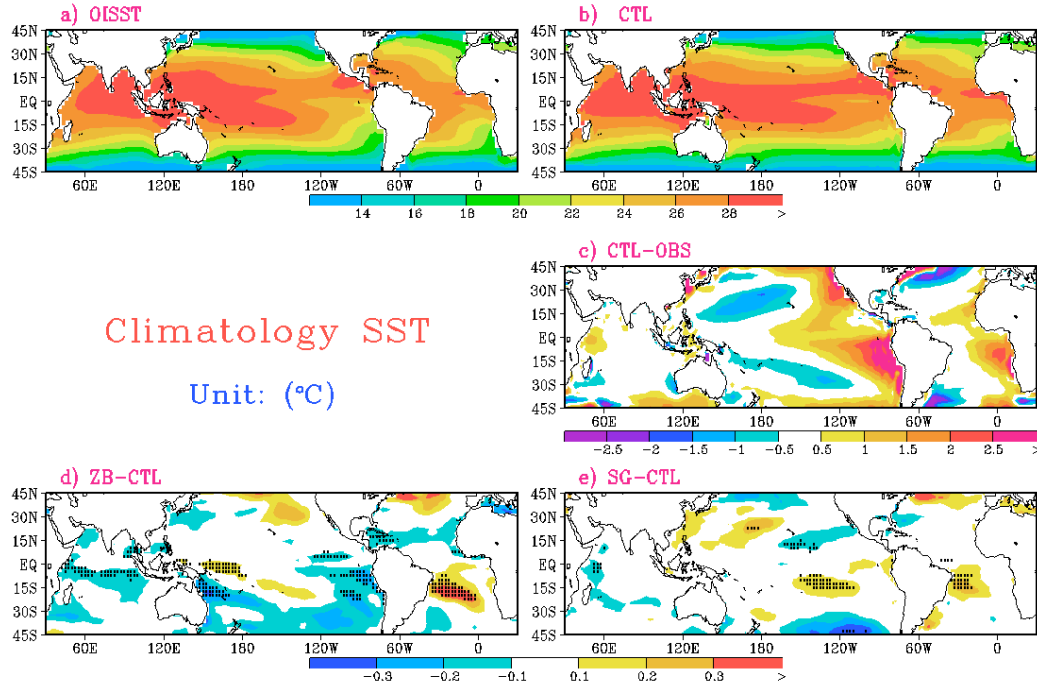
Figure 4.1. 20-year average of sea surface temperature from (a) OISST and (b) CFS control run (CTL), their differences are shown in (c). The modulation of the mean state caused by SST diurnal variability shown in (d) for ZB and (e) for SG with dotted area significant at 0.1 level (t-test). Mean SSTs are plotted every 2^oC, starting at 12^oC. The differences between CTL and OISST are plotted with interval of 0.5^oC, and the differences induced by diurnal SST are plotted with interval of 0.1^oC

66
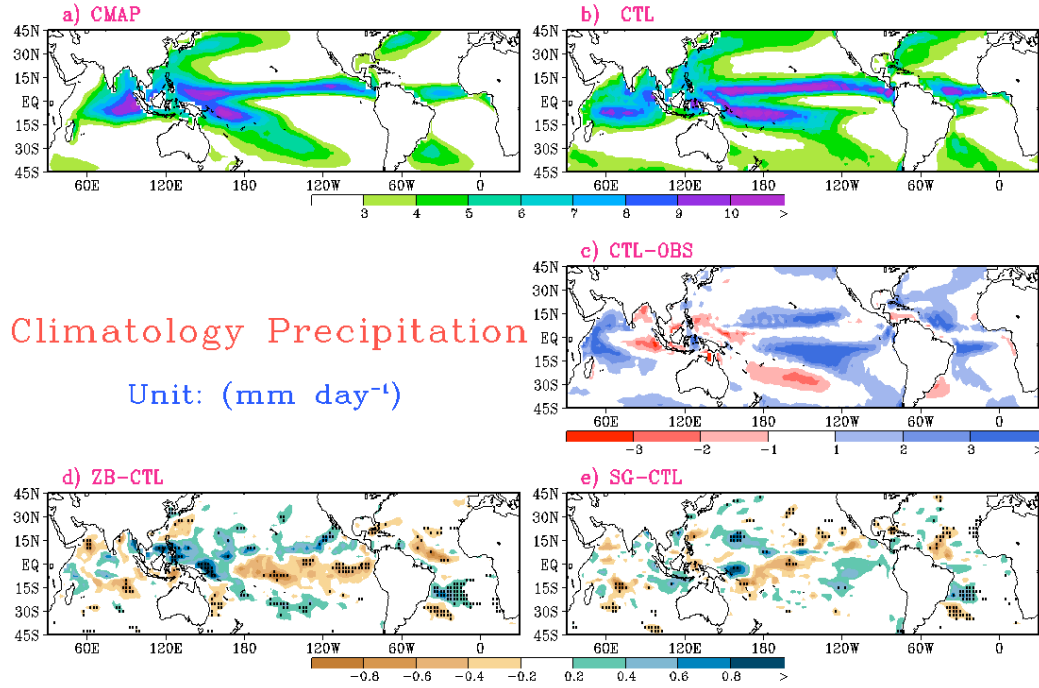
Figure 4.2. 20-year average of precipitation from (a) CMAP and (b) CFS control run (CTL),their differences are shown in (c). The modulation of the mean state caused by SST diurnal variability shown in (d) for ZB and (e) for SG with dotted area significant at 0.1 level (t-test). Mean precipitations are plotted every 1 mm day^{-1}, starting at 3 mm day^{-1}. The differences between CTL and CMAP are plotted with interval of 1 mm day^{-1}, and the differences induced by diurnal SST are plotted with interval of 0.2 mm day^{-1}

averaged CMAP data (CPC Merged analysis of Precipitation, Xie and Arkin, 1997)(Fig. 4.2a) with the annual mean of the model results (Fig. 4.2b). The most notable bias of the precipitation from the CFS CTL run is the double Intertropical Convergence Zone (ITCZ) due to a too zonally oriented South Pacific Convergence Zone (SPCZ), which extends too far eastward and northward and generates excessive precipitation both north and south of the equator throughout the central and eastern Pacifc Ocean(Fig. 4.2c). As a result of the shifted SPCZ, a bias of drought appears in area over the southern Pacific between 15°S to 30°S. Similar patterns featuring the overestimated precipitation off the equator are also seen in the equatorial western Atlantic Ocean.

The double-ITCZ is a persisting problem in the last several generations of coupled
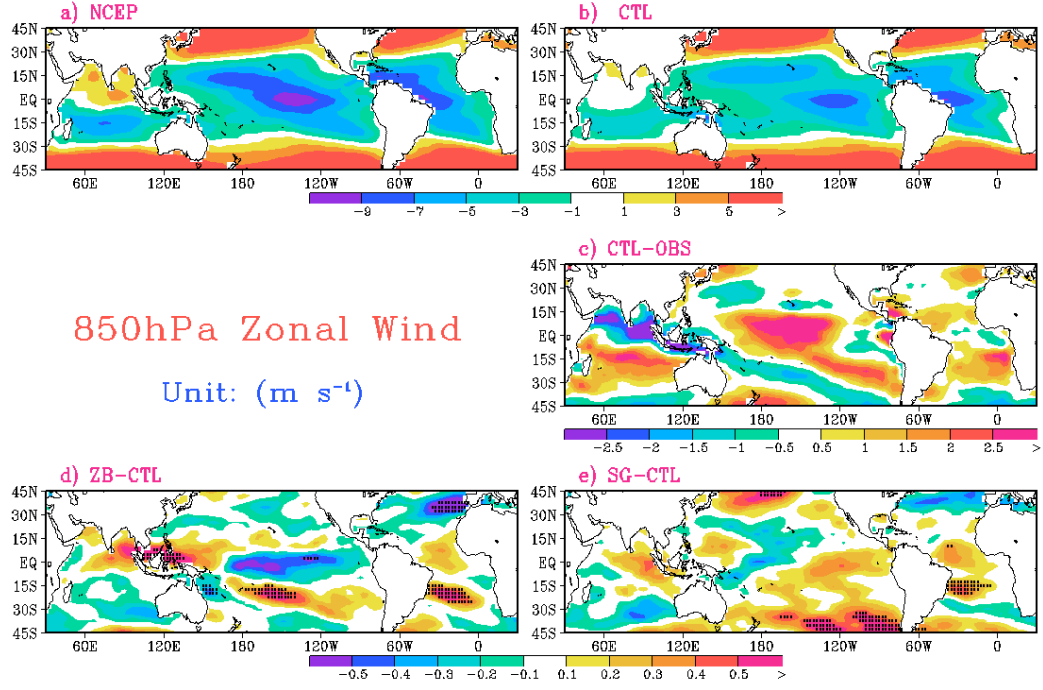
Figure 4.3. 20-year average of 850hPa zonal wind from (a) NCEP reanalysis and (b) CFS control run (CTL),their differences are shown in (c). The modulation of the mean state caused by SST diurnal variability are shown in (d) for ZB and (e) for SG with dotted area significant at 0.1 level (t-test). Mean state are plotted every 2 m s^{-1}. The differences between CTL and NCEP are plotted with interval of 0.5 m s^{-1}, and the differences induced by diurnal SST are plotted with interval of 0.1 m s^{-1}

GCMs (e.g. Mechoso and Coauthors, 1995; Lau et al., 1996; Latif and Coauthors, 2001; Davey and Coauthors, 2002; Meehl et al., 2005). Previous CGCM sensitive experiments suggest that the issue is mainly caused by the AGCM rather than the OGCM (Schneider, 2002). Other studies also show that the bias can be reduced to some extend by increasing the horizontal and vertical resolutions of the atmospheric model (Mechoso, cited 2006), changing the closure or trigger assumptions of convection scheme (Frey et al., 1997; Zhang and Wang, 2006), or improving the simulation of the surface wind stress (Luo et al., 2005; Manganello and Huang, 2009). Besides the double-ITCZ, the model simulated too much rainfall over the western Indian Ocean along the coastal region of Africa that is associated with the SST warm bias in that area (Fig. 4.1c). However, the deficient precipitation is located in the eastern Indian Ocean and Maritime Continent (Fig. 4.2c).

Low-level zonal wind plays an important role in the tropical climate variability. Specifically several studies have demonstrated that the failure of a GCM to simulate the basic-state westerlies in the Indian Ocean and western Pacific Ocean affects the strength and propagation of tropical intraseasonal oscillation in the model (Inness and Slingo, 2003; Inness et al., 2003; Hendon, 2000). By comparing with the NCEP reanalysis data (Fig. 4.3a), the winds from the CTL (Fig. 4.3b) are generally weaker by about 2m s^{-1}, such as the weaker easterlies in the central Pacific to eastern Pacific area(Fig. 4.3c). Such errors are associated with the SST warm biases in the eastern and southeastern Pacific. These SST biases decrease the sea level pressure over eastern and southeastern Pacific. As a result, winds tend to have erroneous convergence over the region and weaken southeast trades. A similar mechanism can also be applied to explain the weaker easterlies over the tropical Atlantic Ocean.

4.2 The influence of the SST diurnal variability on the mean state

Based on the analysis in the Chapter 3, the significant diurnal warming of SST is found over the tropical oceans in two sensitivity experiments. The magnitude of diurnal SST is relatively large (more than 0.7^oC in ZB and 0.3^oC in SG) over the northern Indian Ocean, the equatorial Pacific Ocean, the eastern equatorial Atlantic, and several coastal regions which generally have strong solar radiation and weak winds. When such enhanced diurnal SST variability exists throughout the year, it may affect the mean states of SST, precipitation, lower-troposphere zonal wind, and heat flux in the simulations. We will discuss the details in this section.

4.2.1 SST

By comparing the differences of SST mean states among the CTL simulations and the two sensitivity experiments, the influences from the SST diurnal variability on the mean climate are investigated. The changes of 20-year averaged SST with amplitude more than 0.1^oC are evident in both ZB(Fig. 4.1d) and SG (Fig. 4.1e) experiments.

In the ZB experiment (Fig. 4.1d), the climatological SST is colder than that in CTL for most of ocean basins, including the tropical and southern Indian Ocean, the Arabian Sea, the southeastern Pacific, the east of Japan, and in the tropical Atlantic along 15^oN. However, regions of warmer SST also appear in limited areas of the basins, especially in the subtropical South Atlantic near 15^oS and the Gulf Stream extension. Other regions of weaker warming include the western and central Pacific Ocean to the south of the equator and the eastern part of the North Pacific Ocean.

Although the SST differences from the CTL in the SG simulation have smaller magnitude than in the ZB, similar influence of the diurnal SST on the mean state is also noticeable there (Fig. 4.1e). For example, the SST cooling is founded in the Indian Ocean and in the South Pacific between 30^oS-45^oS, while SST warming is seen in the central Pacific

along 15°S, the southern Atlantic Ocean to the east of Brazil, and the northern Atlantic Ocean along the Gulf Stream. The consistent spatial distribution of the SST mean state differences with the CTL run in both experiments indicates that the influences of diurnal SST variability over these regions are robust. But in other regions, especially for the eastern equatorial Pacific and the western part of the North Pacific, the ZB and SG simulations show the different effects on the SST mean state. The SST cooling is observed in the ZB over the equatorial eastern Pacific and northwestern Pacific Ocean, while the SG experiment displays an opposite sign over these areas. Such different responses possibly relate to the different strength of the diurnal SST variability simulated by ZB and SG schema, but the mechanisms of the responses need further investigation.

Overall, the colder mean SST is a primary feature in both the ZB and SG experiments in comparison with the CTL run. A possible reason is that the heat balance between the atmosphere and the ocean is modified by the implementation of the diurnal mixed layer parameterizations. Especially, the evaporative heat loss from the ocean to the atmosphere may be significantly increased by the diurnal SST variation because the SST becomes a lot warmer in the local afternoon due to the formation of the diurnal mixed layer. Zeng and Beljaars (2005) reported that incorporating their parameterization scheme into ECMWF model enhanced ensemble annual mean surface latent heat flux by more than 10W m^{-2}. Schiller and Godfrey (2005) examined the effect of the diurnal variability of SST on surface latent heat flux using their one-dimensional coupled model with their sublayer scheme. Including this scheme increased the latent heat flux during the daytime by 10-20W m^{-2} and reduced it in the nighttime by 0-5 W m^{-2}, because the scheme reproduces the significant daytime warming of SST. A similar variation of the latent heat flux may also take place in the CFS model with the implementation of the diurnal mixed layer parameterizations. Therefore, it may lead to the mean SST decline over several regions associated with the enhanced heat lost from the ocean. This initial SST change will inevitably cause the adjustment in the other components of the surface heat flux, such as the sensible and long-wave radiative heat fluxes. As a result, a new heat balance is achieved with somewhat lower SST

71

in most part of the ocean. We should note that the SST change generated by local surface heat fluxes may also change the atmospheric circulation on larger scales, which may in turn feedback to the oceanic circulation. This may partly explain the fact that the mean SSTs in the sensitivity runs still become warmer than that in the CTL run in some places. The further task is to quantitatively evaluate the magnitude of these processes.

The different model design between CTL and ZB/SG may also contribute to the SST modulation. In the aspect of the ocean model, the oceanic component of CFS has the first model layer of 10-meter depth, which implies the heat and momentum obtained from the atmosphere uniformly affect in the whole model layer of water. In the contrast, ZB/SG parameterizations reproduce the equivalent effects of the formation/decaying of the thin diurnal mixed layer; therefore more heat and momentum are trapped in the diurnal mixed layer and are inhibited from penetrating deeper during the daytime, thus the heat distribution in the 1st model layer is not uniform. The trapped energy leads to dramatic diurnal SST variations and affects the atmosphere-ocean heat exchange on a daily-scale. After a long-term accumulation, the atmosphere and ocean reach a new energy balance. Its noted that the regions with the significant modulation of SST mean state are related to but not superposed on those regions that have largest SST diurnal variability (Fig. 3.10). The inconsistency suggests that the SST diurnal variability is not a localized phenomenon but may also have profound influences on a broad area through its influences on the atmosphere and/or ocean general circulations.

4.2.2 Precipitation

The changes to the precipitation mean state caused by the diurnal SST variation are mainly located over the tropics and subtropics as shown in ZB and SG simulations (Figs. 4.2d, 4.2e). Compared with the CTL run, both ZB and SG show decreased precipitation in the Indian Ocean, as well as the central Pacific and tropical Atlantic Oceans to the north of the equator. Over the Maritime Continent and western Pacific the precipitation has increased in both experiments, which is especially significant for the ZB simulation and

consistent with the enhanced mean zonal SST gradient near the equator(Fig. 4.1c).

Another enhanced precipitation center is located in the southern Atlantic Ocean east of Brazil that may enhance the southeastward orientation of the SACZ. This change is coherent with the increased mean SST over the region. But in the eastern Pacific Ocean, ZB and SG produce different patterns of the mean precipitation, which can largely be explained by the corresponding modulations of the SST mean state. The ZB experiment generates lower mean SST than does the CTL run over the eastern Pacific; this contributes to the reduction of the precipitation over the area. The opposite case is true for the SG experiment.

In the Indian Ocean and western Pacific, the modulation of mean precipitation due to the diurnal SST variability tends to reduce the biases in the CTL run. As we have pointed out in Section 4.1, the CTL run shows the lack of precipitation over the maritime continent and western Pacific Ocean (Fig. 4.2c). Both ZB and SG experiments tend to intensify the rainfall over the regions although the increase around 1 mm/day is still too small to reduce the local errors significantly. On the other hand, the CTL run produces too much precipitation over the western Indian Ocean between the equator and 15^oS, which is also rectified to some extent in the ZB and SG experiments. Such rectifications suggest that the diurnal SST variability over these regions is one of the factors for the correct simulation of the precipitation. We also notice that the compensation induced by the diurnal SST variability only account for about 10% of the model biases, which indicates that the CFS model needs further analysis in order to understand the cause of the rest of the biases.

4.2.3   850hPa zonal wind

The changes of zonal winds in the ZB and SG experiments from CTL are shown in Figs. 4.3d, 4.3e, respectively. In particular, the westerlies become stronger between the equator and 15^oN from the Bay of Bengal to the dateline in the ZB in comparison to CTL. This change of zonal winds partially reduces the bias in the CTL run in the Indian Ocean, the Maritime Continent and the Western Pacific (Fig. 4.3d). From the central Pacific to the eastern Pacific along the equator, the ZB experiment also shows stronger easterlies that

cancel out the part of biases in the CTL run over the region. To some extent, this wind response is expected because warm SST biases over the region in CTL are reduced in the ZB experiment (Fig. 4.1d). However, in the SG simulation, warm SSTs in eastern Pacific are added on top of model biases (Fig. 4.1e), which further weaken the easterlies in this region. In the southern Pacific (15ºS-30ºS), variations of winds may also relate to the SST modulations in the area. Warm SST bias generally decreases regional sea level pressure and the southeast trade winds, which reflects on zonal wind field as easterly anomalies collocated with a warm SST modulation.

The resulting convergence in the western Pacific also explains the enhanced precipitation there (Fig. 4.2d). Another major mean change is the enhanced westerly winds over the central South Pacific and Atlantic Oceans associated with slightly improved SPCZ and SACZ positions (Fig. 4.2d), consistent with the mean SST change (Fig. 4.1d). Similar wind changes also appear in the SG experiment (Fig. 4.3e).

4.2.4 Heat flux

Since the tropical atmosphere and ocean form a coupled system, the surface heat flux as a source of energy exchange between the two media plays an important role in the atmosphere-ocean interaction. Here we focus on the changes of the net surface heat flux through the air-sea interface (i.e., the latent, sensible and net longwave heat loss from the ocean minus the net shortwave radiation into the ocean) due to the diurnal SST variability. The differences of averaged net heat flux between simulations with and without diurnal SST variability have been shown in Fig. 4.4.

The ZB and SG show a consistent increase of oceanic heat loss in the southeastern Indian Ocean, the tropical Pacific to the east of New Guinea, and the tropical eastern Atlantic along the coastal area, while the reductions of heat lost are observed to the west of Sumatra, northeast of Madagascar, in the central Pacific, and the tropical Atlantic south of the equator. However, for the eastern and southeastern Pacific, the two experiments show opposite signs of heat flux changes associated with the two parameterizations of diurnal
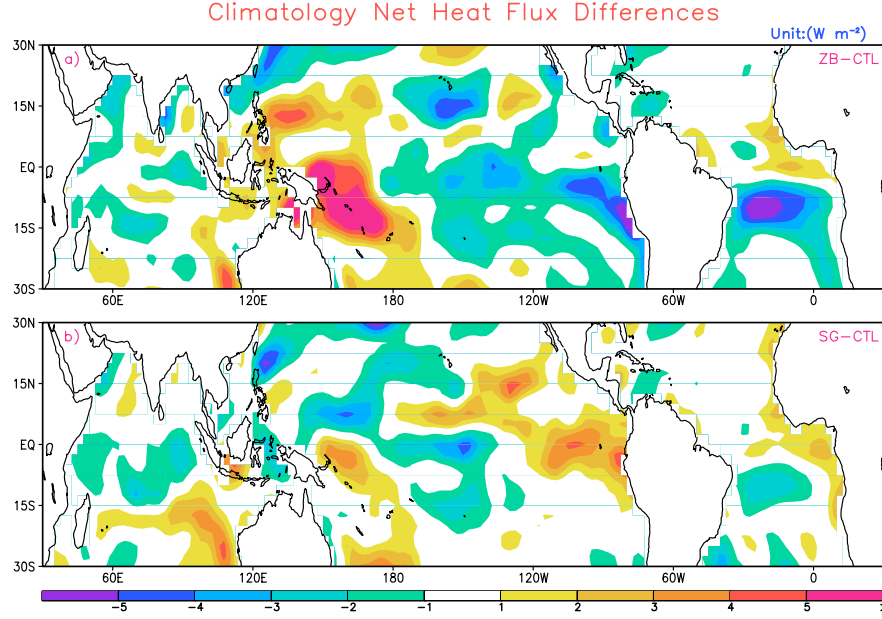
Figure 4.4. Differences of 20-year averaged net heat flux between (a) ZB and CTL and (b) SG and CTL; Positive value for upward heat flux; 9-point smooth applied Unit: W m^{-2}

mixed layer. Compared with the SG experiment (Fig. 4.4b), the ZB run generates more systematic variations of the net heat flux, showing the maximum heat loss greater than 5W/m^2 in the western Pacific between the equator and 15°S and from the western boundary to the dateline. On the other hand, major heat gains appear in the equatorial eastern Pacific and southern tropical Atlantic (Fig. 4.4a).

The variations of latent heat flux contribute to the most of the changes in the net heat flux (Fig. 4.5). The ratio of explanation (i.e. portion of latent heat flux variation in the variations of net heat flux) can be more than 60% in regions such as the western and eastern Pacific and the tropical Atlantic (figures not shown). The patterns of the latent heat variations are highly correlated with the modulation of the wind and SST fields described in the previous sections. The weakening of trade winds and reduced SST lead to the reductions of latent heat flux, while an increase in the wind speed and SST induces more heat loss from the ocean.

75
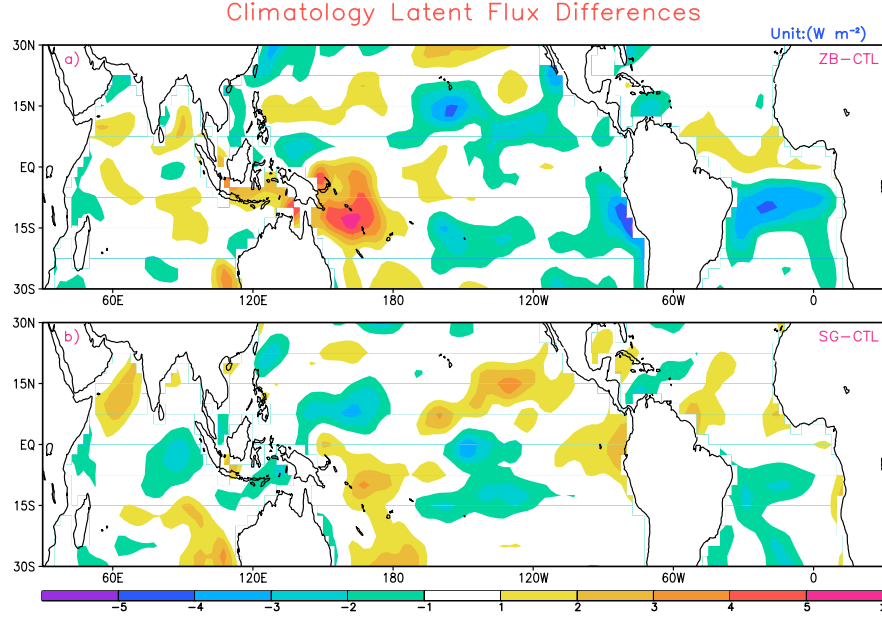
Figure 4.5. As in Fig. 4.4 but for latent heat flux only

According to the variables examined above, we can draw the conclusion that the SST diurnal variability influences the mean state of the tropical climate. The variations in the fields of sea surface temperature, precipitation, zonal wind and net heat flux are reasonable and consistent with each other. Between the two experiments with diurnal mixed layer parameterizations, the coherent modulations are observed in most of ocean basins with relative large amplitude in ZB run due to the fact that ZB schemes produced stronger signals of SST diurnal variability. However, there is a noticeable inconsistency of modulations in the eastern and southeastern Pacific between the ZB and SG runs, because the two schemes generated opposite changes of the mean SST in these regions, which may be due to the different design of the parameterization schemes. It is interesting that there are sensitive regions of mean atmospheric response, such as the western Pacific and marine continent, where the wind and precipitation, as well as the ocean-atmosphere heat exchange, are modified by the diurnal SST change significantly. These changes seem to be mainly a response of the coupled system to the mean SST change induced by the SST diurnal cycle.

The specific feedback processes need to be further explored through additional sensitivity experiments.

4.3 The influence of the SST diurnal variability on the SST interannul varability over the eastern Pacific Ocean

From the previous analysis of the model results, we notice that the significant diurnal SST variability and its influences on the atmospheric circulation occur over both the western and eastern equatorial Pacific where the El Nio-Southern Oscillation (ENSO) dominates. It is worth discussing whether the high frequency variability of the SST diurnal cycle has any influence on the ENSO related SST variability. For this purpose, we have examined the interannual variability in the tropical Pacific Ocean from the CTL run and the sensitivity experiments using the monthly mean fields. The monthly anomaly fields are calculated by subtracting a monthly climatology from the total length of respective runs.

The Hovmoller diagrams for time-longitude are created for the monthly SST anomalies along the equatorial Pacific (averaged within 10^oS to 10^oN) from CTL, ZB and SG experiments respectively (Fig. 4.6). The model results show that the ENSO-like oscillation in all three experiments occurs five times during the 20-year integration. On average, alternating warm and cold events occur every 4 years, the period of the oscillation shows more regularity in the CTL run (Fig. 4.6a) compared with the simulations including the diurnal SST variability (Figs. 4.6b, 4.6c). Starting from the same initial state, the diurnal SST changes in the ZB and SG experiments seem to prolong the equatorial cold event and cause a delay of the occurrence of the first warm events. In general, the warm events in the sensitivity runs tend to last longer.
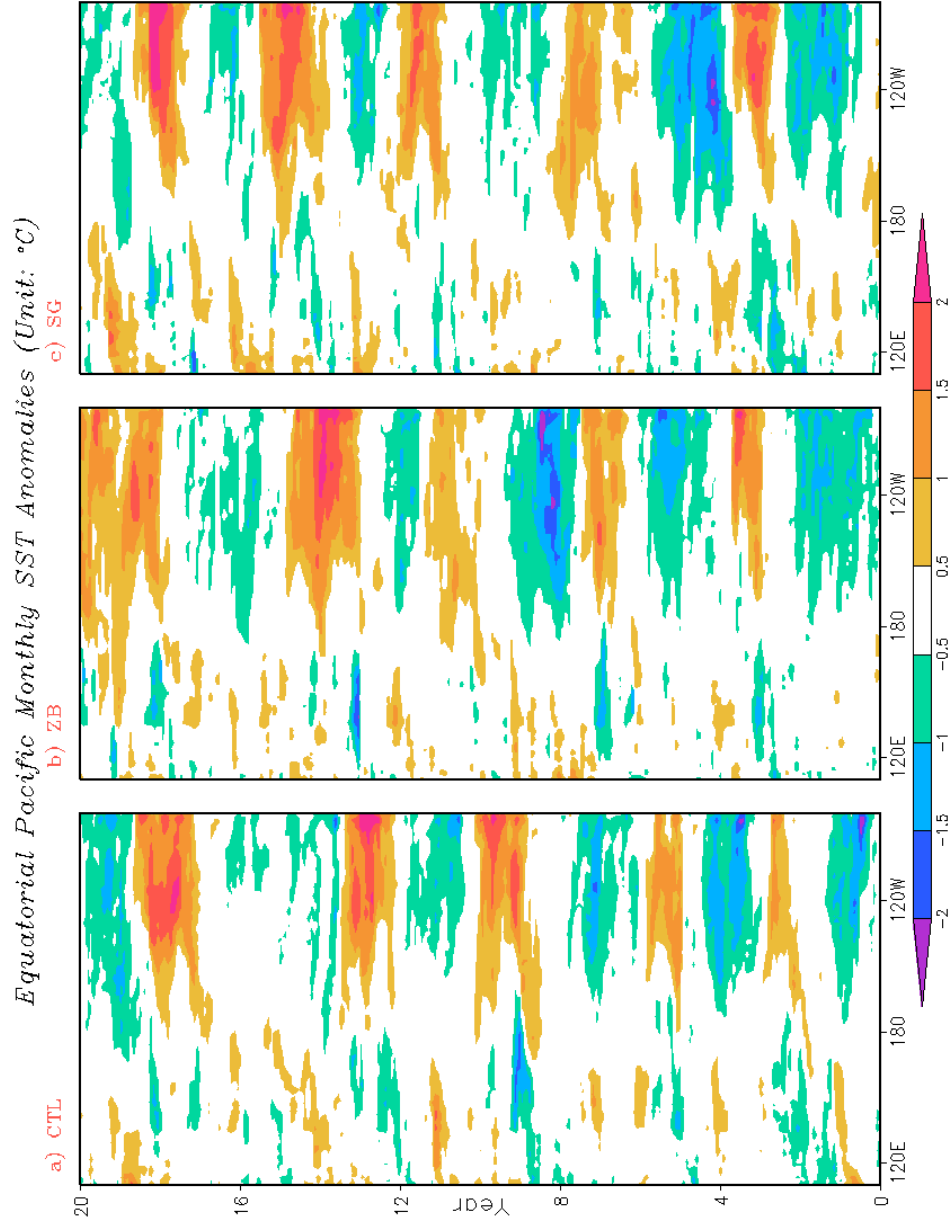
Figure 4.6. Time-longitude diagram of monthly SST anomalies along the equatorial Pacific (110°E-80°W) for a) CTL run, b)ZB run, and c) SG run, respectively. Unit: °C

Since the averaged SST anomaly over the region (5°S-5°E, 170°-240°W), defined as the NINO3.4 index, is a good index of ENSO variability (Barnston et al., 1997), the time series of Nino3.4 SST anomalies for the simulations are presented in Fig. 4.7. The amplitude of several cold/warm events in ZB and SG are larger than those of the CTL run. For instance, the cold anomalies in the 8th year for the ZB and 4th year for the SG reach above 2°C, and the similar magnitude is also observed during some warm events in ZB/SG but not appearing in the CTL run. Although there is certain shift of the occurrence of ENSO in different simulations, the power spectrum analysis shows no significant change of the dominated period of the oscillation among the simulations.

The standard deviation of monthly mean SST over Pacific Basin based on all three simulations is shown in Fig. 4.8. The spatial patterns are comparable among the simulations, and the SST variance larger than 1.4^{o}C is located over the eastern equatorial Pacific Ocean. The magnitude of standard deviation is slightly changed in ZB and SG simulations compared with the CTL run (Fig. 4.8a). The SG (Fig. 4.8c) displays the larger variance over the cold tongue area while ZB (Fig. 4.8b) presents a slight decline of the magnitude.

By introducing the diurnal SST variability, ZB and SG show some effects on the amplitude of the interannual SST anomalies. The alternating phase of the cold/warm events in ZB/SG is not as regular as in the CTL run. But based on the available model results, we cannot rule out the possibility that such change of ENSO related SST are purely due to the model adjustment to the high frequency noise. A longer integration is necessary to confirm if there is eventually a modulation of the SST interannual variability eventually by the diurnal SST change.
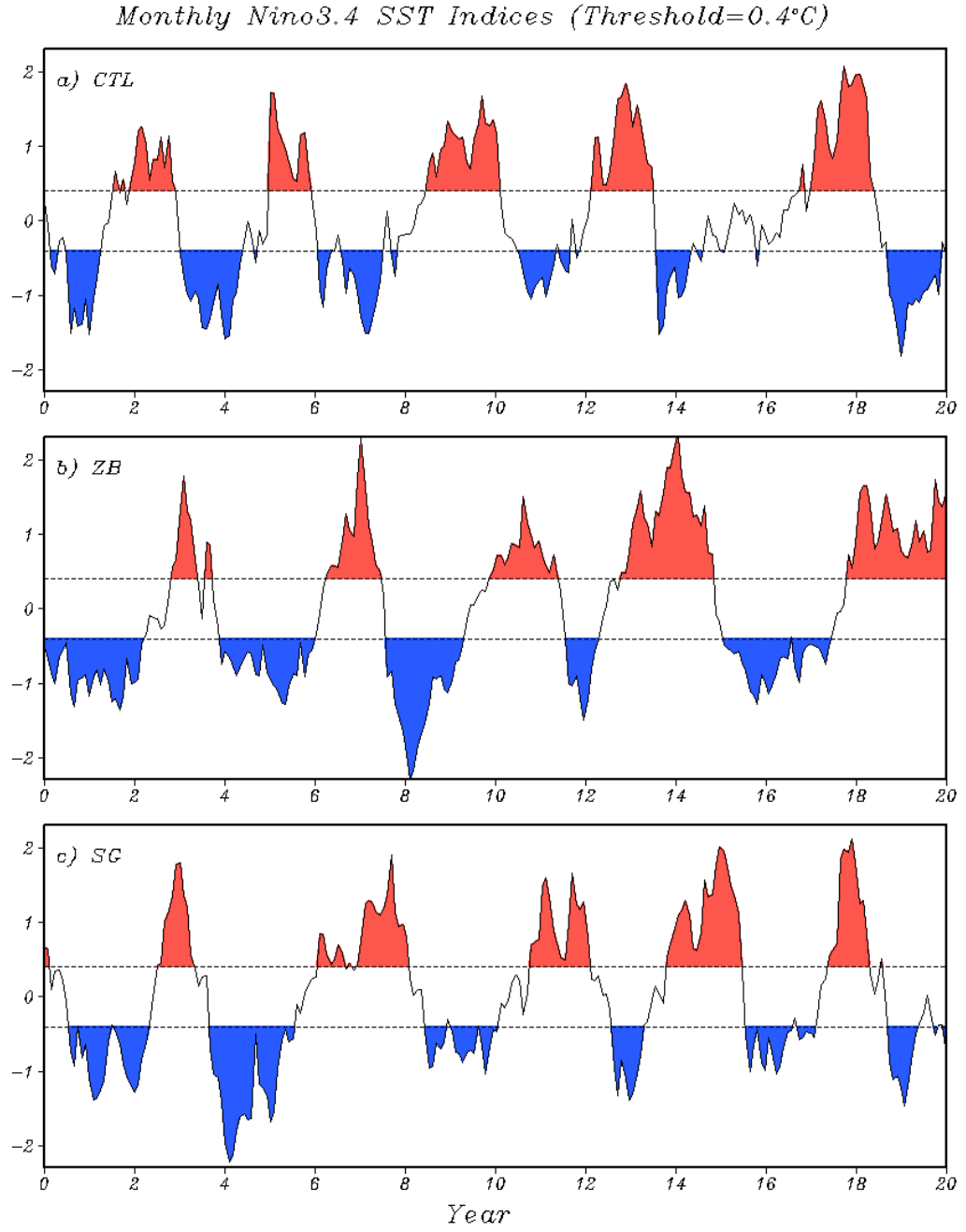
Figure 4.7. Nino3.4 SST indices (The average of SST anomalies over 5ºS-5ºN and 170ºW-120ºW) for a) CTL run, b) ZB run, and c) SG run, respectively. Values exceeding thresholds of ±0.4ºC are stippled to indicate ENSO events.

Figure 4.8. Standard deviation of SST anomalies over the Pacific ocean for a) CTL run, b) ZB run, and c) SG run, respectively. Unit: ^{o}C.

Chapter 5: The influence of diurnal SST variability on the intraseasonal oscillation

As we discussed in previous chapters, the diurnal SST variability exhibits large amplitude in the tropics. Daily SST rise in late afternoon can increase the surface net heat loss from the ocean to the atmosphere, which is a non-negligible component for air-sea exchange processes. Many studies reveal the importance of the diurnal SST variations on the tropical atmospheric variability, specifically on the tropical intraseasonal oscillation (ISO). Slingo et al. (2003) proposes that stronger SST diurnal cycle in the suppressed phase of ISO leads to an enhanced convection. In turn the relatively shallow convection gradually moisten the atmospheric boundary layer and prepare a favorable condition for deep convection. Woolnough et al. (2007) found that resolving diurnal SST variations in a coupled model leads to an improvement in its prediction skill, especially during the ISO phase of enhanced convections over the Indian Ocean and the western Pacific Ocean.

The purpose of this chapter is to investigate how the diurnal SST variability affects the tropical intraseasonal variability in the CFS model. We first evaluate the tropical intraseasonal oscillation in the model simulations. Then, the influence of the diurnal SST variability on the ISO is investigated. According to the analysis in Chapter 3, the ZB and SG parameterization schemes produce similar patterns of diurnal SST variability over the Indian and western Pacific oceans, but the ZB experiment has a more realistic magnitude of the SST diurnal cycle. Therefore, the following diagnosis and comparison are mostly based on a comparison between the results from the CTL and ZB experiments.

5.1 Diagnosis of the intraseasonal oscillation in model simulations

The intraseasonal oscillation (ISO), as an important component of the tropical climate variability, exhibits large-scale convection anomalies that interact strongly with the tropospheric circulation and surface fluxes of mass, heat, and momentum.(Madden and Julian, 1971, 1994; Rui and Wang, 1990; Hendon and Salby, 1994; Matthews, 2000; Sperber, 2003; Kiladis et al., 2005). During a typical ISO event, a positive convection anomaly develops over the western Indian Ocean and tends to propagate slowly eastward to the central Pacific. At its peak phase, the most intense convection anomalies associated with ISO events are usually located over the warmer tropical water in the central/eastern Indian Ocean and western Pacific Ocean, and the convection is often suppressed over the Maritime Continent. Once the convection anomalies reach the date line, the disturbance will be suppressed due to the cooler water underneath.

The observed ISO shows a distinct seasonal contrast, especially for the eastward propagation of convection/circulation anomalies. During boreal winter (November-April), when the Indo-Pacific warm pool is centered near the equator, the eastward propagation tends to be most strongly exhibited along the equator. In the boreal summer (May-October), the meridional asymmetry of the mean state associated with the Asian summer monsoon tends to result in northeastward propagation from the equatorial Indian Ocean into Southeast Asia, while at the same time exhibiting eastward propagation along the equator (Yasunari, 1981; Wang and Rui, 1990; Annamalai and Sperber, 2005; Waliser, 2006).

According to the observational characteristics of the intraseasonal oscillations, our diagnosis on the model simulations will mainly focus on the tropical area over the Indian and Western Pacific oceans. To identify the intraseasonal oscillation in model results, unfiltered anomalies of variables are first computed by subtracting the climatological daily mean calculated over all years of the data. Then, an intraseasonal (20-100-day) bandpass filtering is applied on the anomalies using a 201-point Lanczos filter (Duchon, 1979), which has

half-power points at 20- and 100-day periods. We adopt several diagnostics developed by the CLIVAR Maddend-Julian Oscillation Working Group (Waliser and Coauthors, 2009). The strategy provides a consistent method to evaluate the model simulated intraseasonal oscillations with respect to the observations, and it also provides the possibility of further intercomparison among the models. We will diagnose the ISO in the simulations from several aspects, including the evaluation of the variance on the intraseasonal time scale, the eastward and northward propagation of the ISO, the multivariate EOF analysis and the phase-based life cycle composite of the ISO.

5.1.1 The seasonal variation of the mean state

Capturing seasonal variation of the background states is a crucial starting point for the assessment of the ISO simulation. As we discussed in the previous chapter, the CFS model has significant mean state biases. In this section we will briefly present the model biases in the SST, the precipitation and the 850hPa zonal wind in different seasons because the observed ISO has a distinct seasonal variations based on the observations. The seasonal means of these variables for boreal winter (November-April) and summer (May-October) are calculated for the CTL run (Fig. 5.1). The biases of each field are evaluated by comparing with the 20 year averaged observations (Fig. 5.2).

During the boreal winter (Figs. 5.1a, 5.2a), the model incorrectly produces the warmest SST in the Indian Ocean over the western part of the basin. While the observed high SST over the eastern Indian Ocean in the observation is underestimated in the CTL run. The simulated SST pattern near the Maritime Continent and in the western Pacific Ocean is comparable with the observations. In the boreal summer (Figs. 5.1d, 5.2d), the SST is generally overestimated in the Indian Ocean. The warm pool over the western Pacific Ocean displays less of a meridional expansion, but extends too much eastward into the central Pacific. Since the convection associated with tropical intraseasonal variability is confined to the regions of the warmest SST, the SST biases could have an adverse impact on the simulation of ISOs.
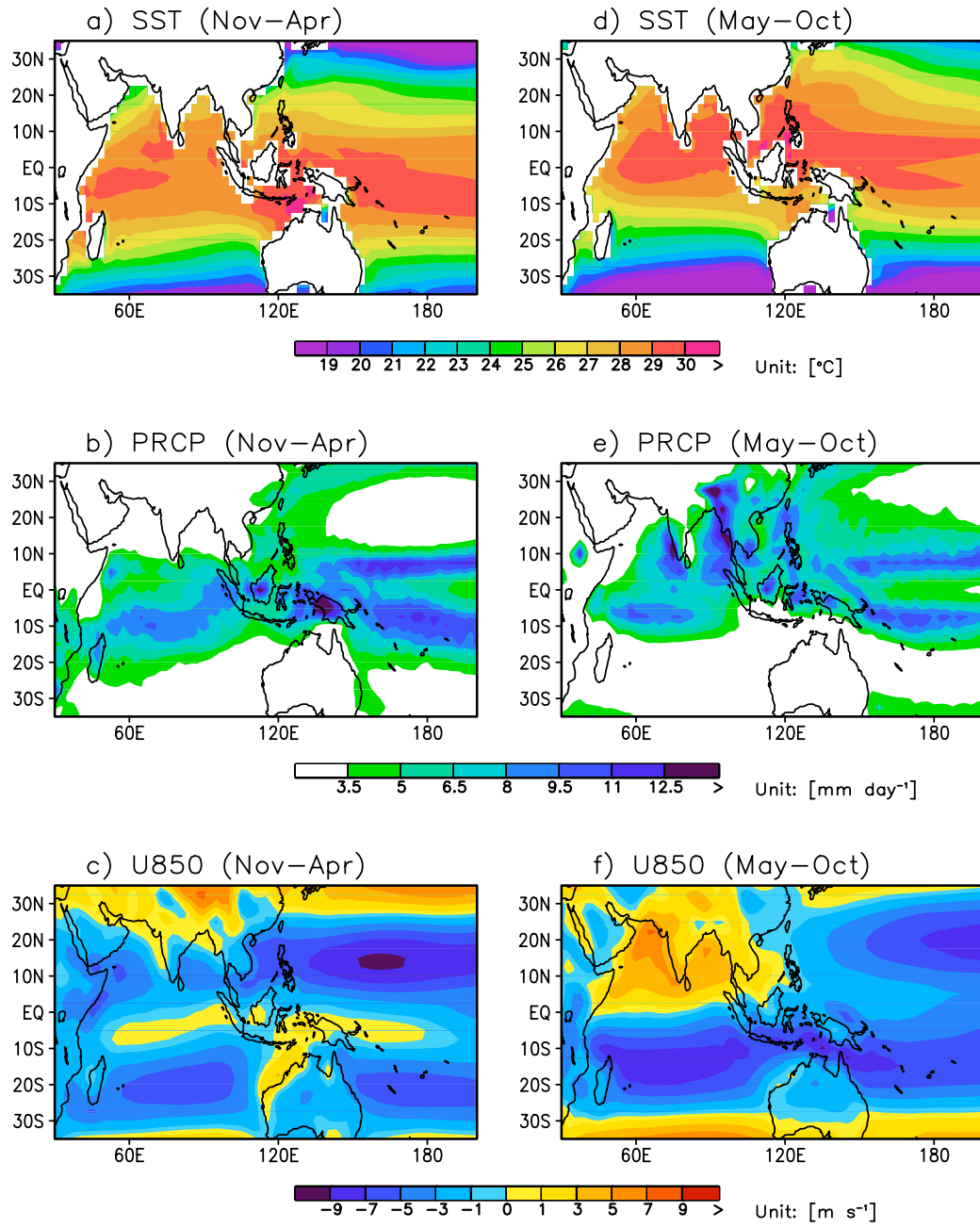
Figure 5.1. 20-year average of SST (a,d), precipitation (b,e) and 850-hPa zonal wind (c,f) of CTL run for boreal summer (May to October, left column) and boreal winter (November to April, right column)
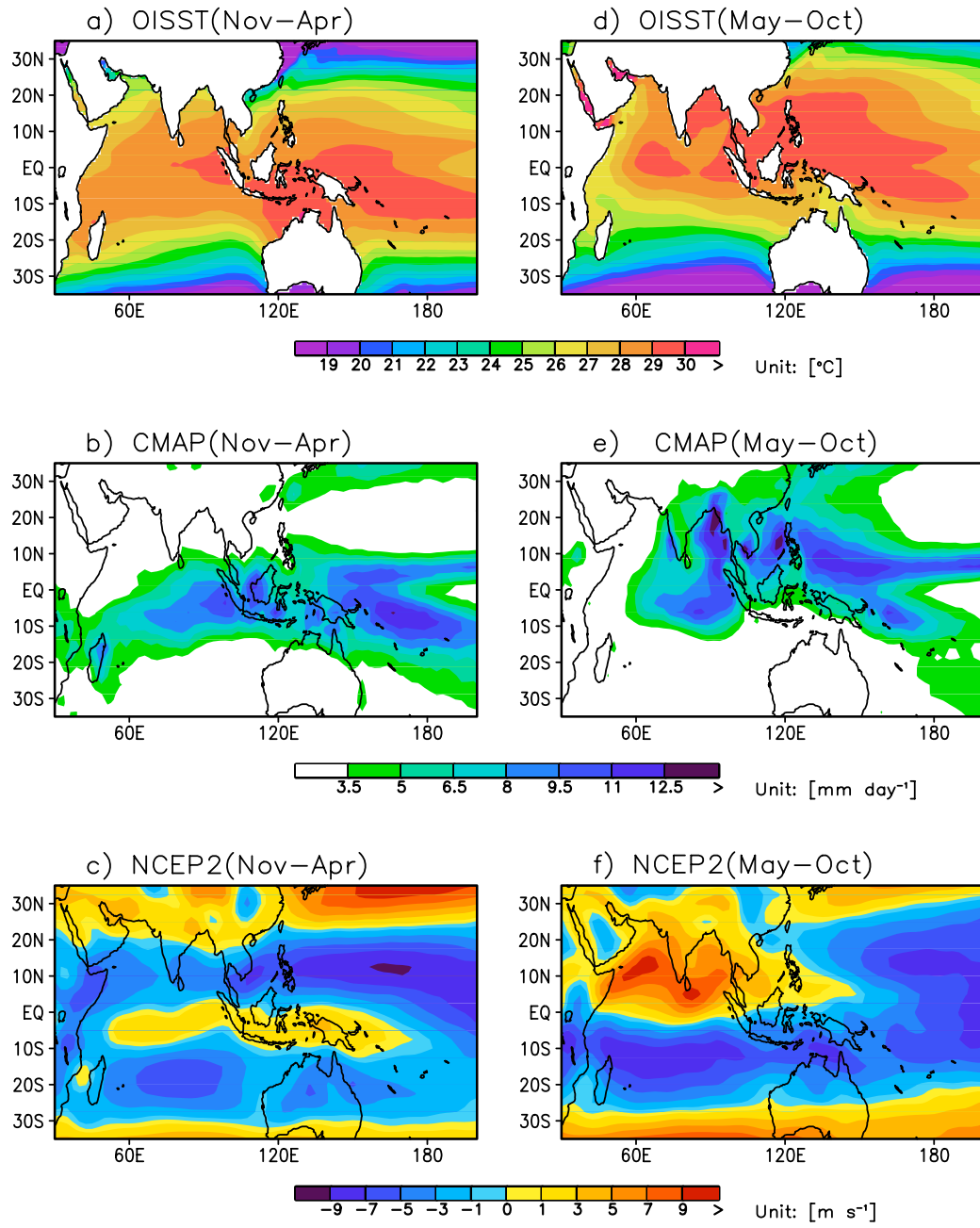
Figure 5.2. Observations of climatology SST (OISST, a,d), precipitation (CMAP,b,e) and 850-hPa zonal wind (NCEP2 c,f) for boreal summer (May to October, left column) and boreal winter (November to April, right column)

The biases of the rainfall mainly correspond to the SST biases mentioned above. For instance, the model generates too much rainfall in the western Indian Ocean and too little rainfall over the eastern part of the basin during the boreal winter (Figs. 5.1b, 5.2b). This is due to the respective warm and cold SST biases in the regions, respectively. For the summer season (Figs. 5.1e, 5.2e), the overestimated rainfall in the southwest of the Indian subcontinent and the double ITCZ problem in the western Pacific Ocean are also related to the SST biases in the simulation.

The mean state of 850hPa zonal winds, especially the westerlies in the Indian Ocean and western Pacific, can affect the magnitude and its propagation of the ISOs (Inness and Slingo, 2003; Inness et al., 2003; Hendon, 2000). Overall, the model mean westerlies tend to be weaker by at least 2m/s than the reanalysis winds in both the winter and summer seasons. The westerlies along the equator are disconnected over the maritime continent during the boreal winter, while in the boreal summer the zonal winds over the Arabian Sea and the Bay of Bengal are reduced by more than 4m s^{-1}.

The ZB experiment generally presents similar biases on all fields to those shown in the CTL run (Fig. 5.1), but the implementation of the diurnal SST variability in the ZB tends to compensate for the model biases over several regions for different variables; however, the ratio of the rectification to the errors is relatively small. To illustrate such modification, the differences of seasonal climatology of SST, precipitation and 850hPa zonal winds between ZB and CTL runs are presented in Fig. 5.3. An improvement of the seasonal mean states is observed. For instance, the boreal winter mean SST in ZB is reduced by 0.2-0.3^{o}C over the western Indian Ocean (Fig. 5.3a). Correspondingly, the rainfall is decreased by about 0.4-0.6 mm day^{-1} in the region (Fig. 5.3b), while the CTL run produces too much precipitation(Figs. 5.1b, 5.2b). The noticeable improvement of the precipitation is also displayed in the Maritime Continent and the western Pacific Ocean during the boreal summer. The ZB run produces more than 0.8 mm day$^{(-1)}$ precipitation over these regions in comparison with the CTL run, which leads to a more realistic precipitation distribution over the area. The low-level westerlies are also greatly improved in the ZB during the boreal
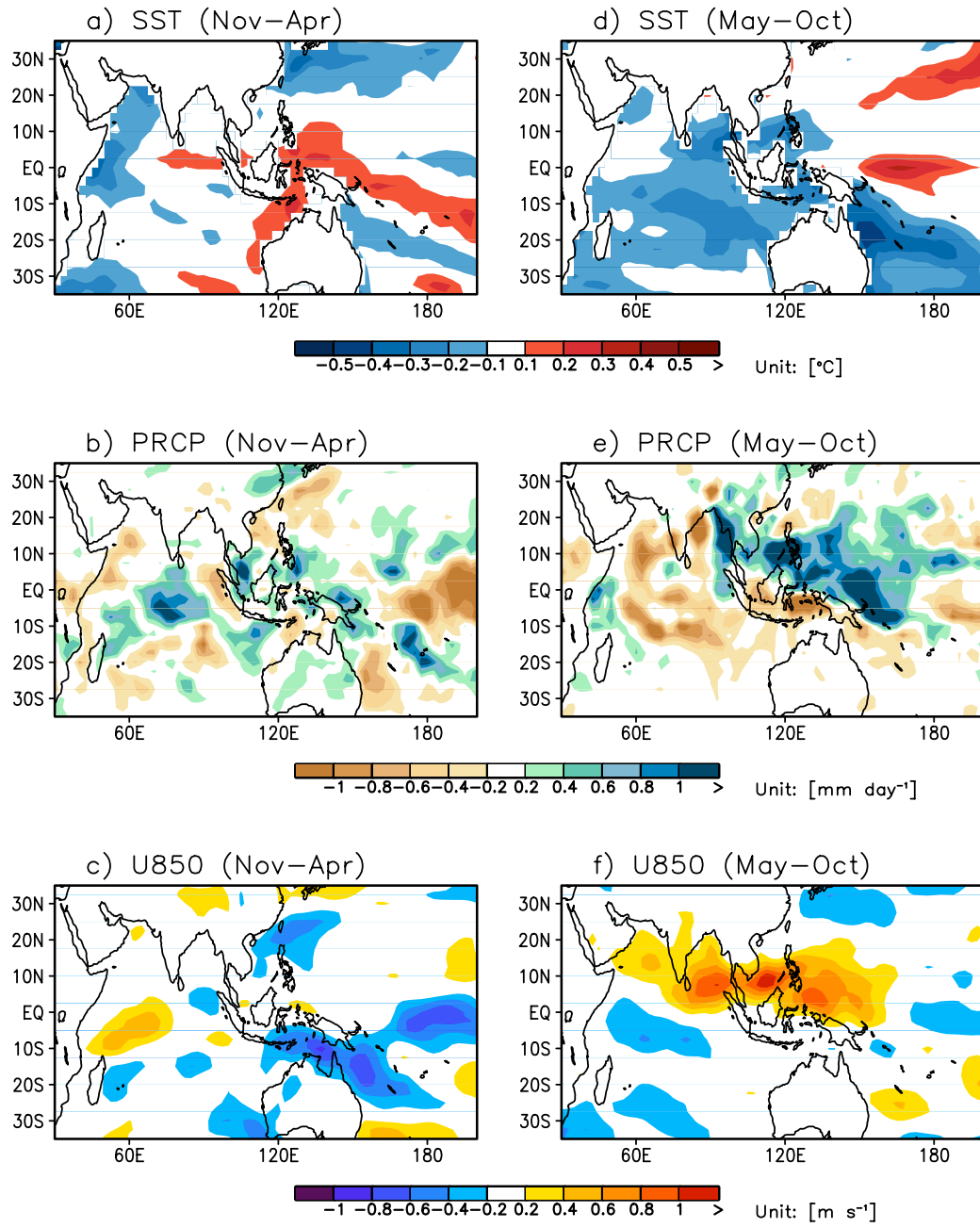
Figure 5.3. Differences of seasonal climatology of SST (a,d), precipitation(b,e), and 850hPa zonal wind(c,f) between ZB and CTL runs. 20-year average of CTL run was subtracted from 20-year average of ZB run for boreal summer (a,b,c) and boreal winter (d,e,f)

summer. The zonal winds are generally intensified by above 0.4m s^{-1} from the Indian Ocean to the western Pacific Ocean. All of these rectifications may contribute to the improvement of the ISO simulation.

5.1.2 The intraseasonal variations

The intraseasonal oscillation (ISO) over the tropical area features large-scale convection anomalies. Therefore, the outgoing longwave radiation (OLR) anomalies are calculated to reveal the convective activities for the CTL and ZB experiments. A 20-100-day bandpass filtering is conducted on the anomalies to emphasize the variations of the intraseasonal scale. Fig. 5.4 and Fig. 5.5 show the standard deviation of the filtered OLR anomalies of observation (AVHRR) and model simulations for boreal winter and boreal summer, respectively.

The maps of the standard deviation illustrate that the variances of the tropical intraseasonal variations tends to be concentrated in the summer hemisphere. Compared with the observation (Figs. 5.4a, 5.5a), CTL and ZB generate exaggerated intraseasonal variability of the convection throughout the tropical area, especially over the regions of the maximum intraseasonal variance. These model results also show some problems in the location of the connective centers over the Indian Ocean for both seasons. The maxima in the model simulation are shifted erroneously to the western basin in the boreal winter(Figs. 5.4b, 5.4c). During the summer, the model simulations produce too strong variance in the Arabian Sea and the Bay of Bengal (Figs. 5.5b, 5.5c). These biases are partly due to the errors of the SST mean state as we discussed in the previous section. The model has a warm bias in the western Indian Ocean for the boreal winter, and it overestimates the SST in the northern Indian Ocean during the boreal summer.

A comparison of ZB and CTL illustrates a certain improvement of intraseasonal variability over the western Pacific by introducing the diurnal SST variability. For the boreal winter, the ZB run (Fig. 5.4c) shows smaller variance than the CTL run (Fig. 5.4b) does to the north of New Guinea. The large variance in the ZB run is more concentrated to
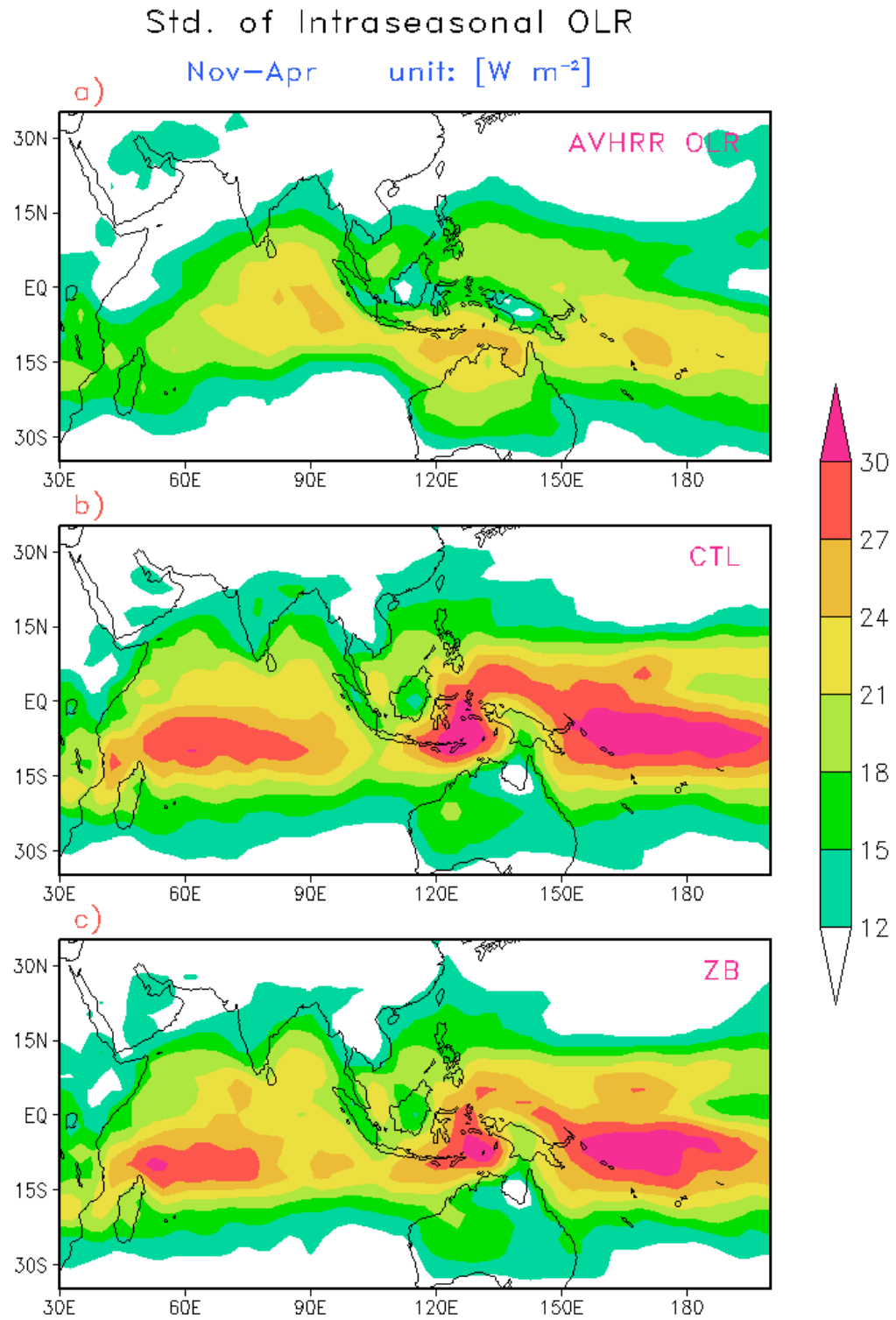
Figure 5.4. Standard deviation of intraseasonal outgoing long-wave radiation (OLR). 20-100-day band-pass filter was applied on daily averaged OLR and standard deviation was calculated for a) AVHRR observation, and simulations of b) CTL run and c) ZB run
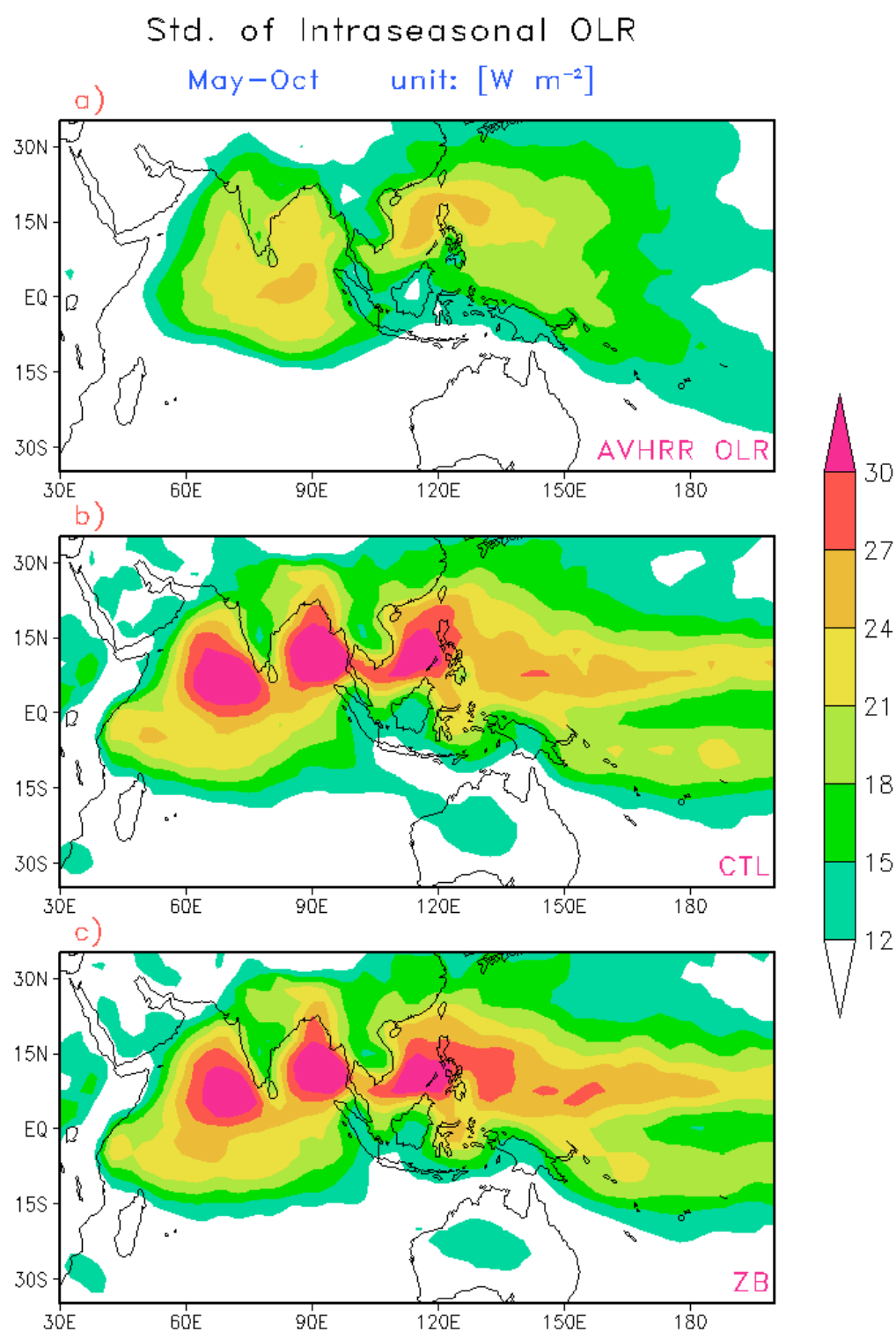
Figure 5.5. As in Fig. 5.4 but for boreal summer (May-October)

the west of the date line in the ZB run, which are more consistent with the observations (Fig. 5.4a). During the boreal summer, the intraseasonal variance of OLR in the ZB run exhibits the maxima to the east of Philippines, which are also apparent in the observations but missed in the CTL run.

5.1.3 Eastward and northward propagation

The propagating nature of the ISO is investigated for the CTL and ZB experiments through several lag-longitude correlation analyses for regions that can be observed in Fig. 5.4 and Fig. 5.5. The analyses are performed for boreal winter and boreal summer separately to illustrate the distinctive features of the ISO propagation in different seasons. Fig. 5.6 shows lag-longitude diagrams of intraseasonal OLR(shading) and 850-hPa zonal winds(contour) correlated against OLR at the reference point in the Indian Ocean (OLR time series; area averaged 10^oS-5^oN, 75°-100^oE) for boreal winter. In general, the simulations (Figs. 5.6b, 5.6c) are able to capture the characteristics of the eastward propagation for convection (OLR) and zonal winds (U850), although the correlation coefficient is not as large as that shown in the observations (Fig. 5.6a). It takes about 40-50 days for the OLR anomaly to propagate across the Eastern Hemisphere. For both simulations, such eastward phase speed is consistent with the observations for both simulations. Another feature of the ISO revealed by observations is that the zonal wind anomaly lags behind the OLR anomaly by about 5-7 days, which is also represented in the simulations to some extent. Qualitatively similar behaviors are also shown in the boreal summer lag-longitude analysis (figures not shown).

Besides the eastward equatorial propagation, a distinctive northward propagation is the dominant character of the boreal summer intraseasonal variability (Yasunari, 1979; Wang and Xie, 1997). Similarly to the method described above, the lag-latitude correlations are calculated to diagnose northward propagation in the Indian Ocean. In this case, the reference domain is also selected as 10^oS-5^oN, 75°-100^oE in the Indian Ocean, but the 850hPa zonal wind and OLR averaged over 80°-100^oE are regressed onto the time series of
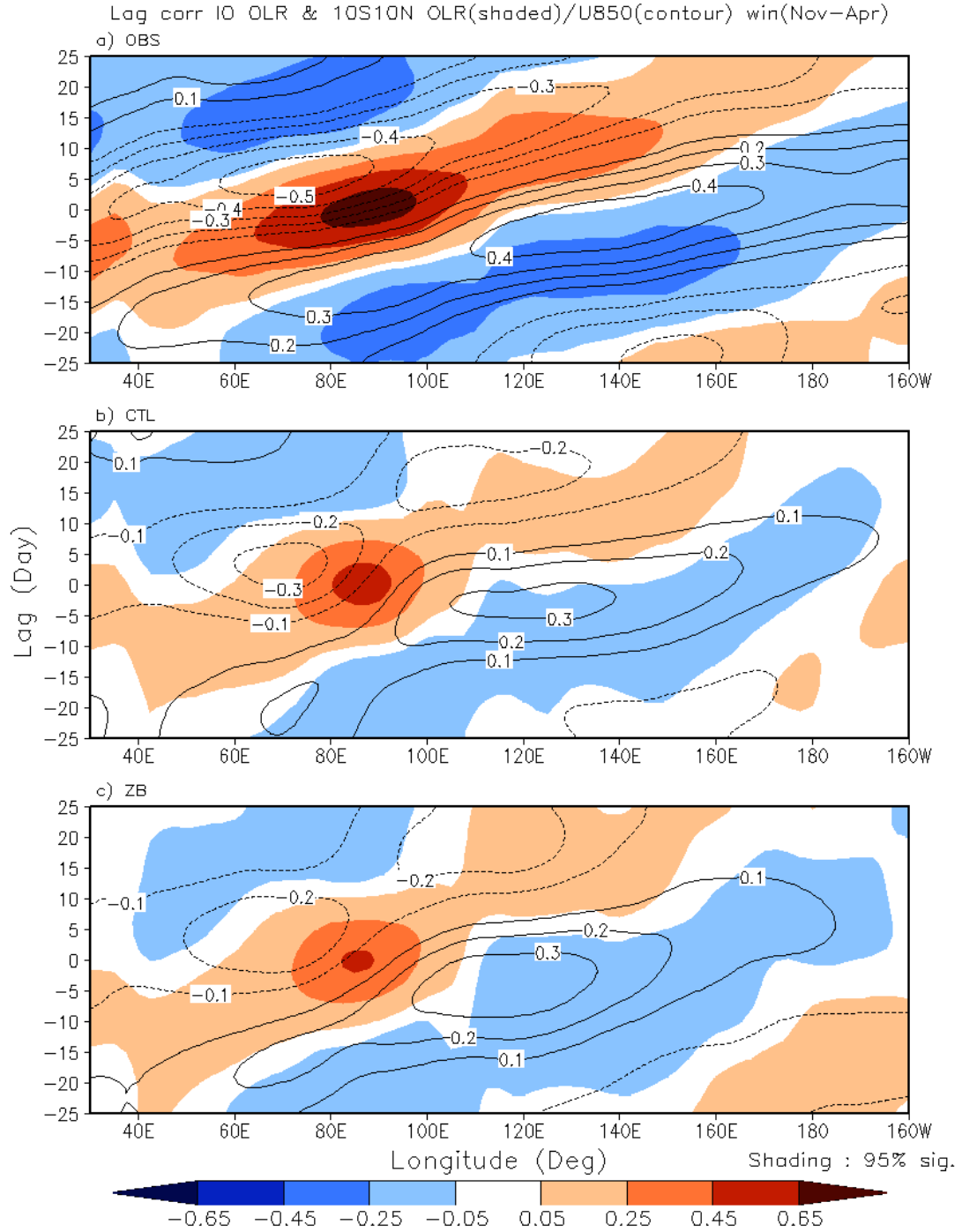
Figure 5.6. November-April lag-longitude diagrams of 10^oS-10^oN averaged intraseasonal OLR anomalies (shaded) and intraseasonl 850hPa zonal wind anomalies (contour) correlated against intraseasonal OLR at the Indian Ocean reference point (75°-100^oE, 10^oS-5^oN). Correlations were calculated for a) observation (AVHRR OLR and NCEP1 U850), and simulations of b) CTL run and c) ZB run

Figure 5.7. May-October lag-latitude diagrams of 80°-100°E averaged intraseasonal OLR anomalies (shaded) and intraseasonl 850hPa zonal wind anomalies (contour) correlated against intraseasonal OLR at the Indian Ocean reference point (75°-100°E, 10°S-5°N). Correlations were calculated for a) observation (AVHRR OLR and NCEP1 U850), and simulations of b) CTL run and c) ZB run

the averaged OLR within the reference domain. As shown in Fig. 5.7, the model shows a deficiency of the northward propagation; this is apparent in observations from the equator into the northern hemisphere for both OLR and zonal wind (Fig. 5.7a). Interestingly, the southward propagation from the equator into the southern hemisphere is evident in the simulations (Figs. 5.7b, 5.7c), which is consistent with the observations (Fig. 5.7a) and has been reported by Lawrence and Webster (2002) and Annamalai and Sperber (2005).

5.2   Life cycle composite of the ISO

To explore more detailed features of the intraseasonal oscillation, we adopt the all-season multivariate index described by Wheeler and Hendon (2004), which is a widely used index to inspect the evolution of the intraseasonal variability (Zhang, 2005; Weare, 2006; Lin and Coauthors, 2006; Pegion and Kirtman, 2008; Vitart, 2009). Their method is based on based on the multivariate EOF analysis using equatorial averaged (within 15^oS-15^oN) equatorial anomalies of 850hPa zonal winds, 200hPa zonal winds, and OLR. The wind and OLR anomalies are individually filtered to the 20-100-day band and normalized by the square roots of the zonally averaged variances respectively before being input into a covariance matrix used to conduct the EOF analysis.

We conduct the diagnostics of the intraseasonal filtered NOAA OLR, and NCEP1 850- and 200-hPa zonal winds data as a benchmark. Fig. 5.8 shows the EOF1 and EOF2 derived from all seasons of observations during 1979-2005. The EOF modes of model simulations are also presented (Fig. 5.9, CTL and Fig. 5.10, ZB) to test the phase relationship between equatorial convection and wind anomalies. Compared with the observations, model simulations capture several important features of ISO. For instance, the out-of-phase relationship between lower- and upper-tropospheric zonal winds anomalies is correctly represented in both CTL and ZB runs. The strong amplitude of wind anomalies across both the Eastern and Western Hemisphere is reproduced in both simulations. Especially, the ZB run provides wind anomalies more comparable with the observations. We also note that the

lower-tropospheric westerlies are near and to the west of the enhanced convection according to the observations, and such a phase relationship is consistently reproduced by the simulations.

However, there are some deficiencies of the model-simulated ISO as indicated in these figures. The overall variance accounted for by each EOF is relatively small in the simulations, which is about 15% in ZB and CTL runs but can be more than 20% for the observation. Moreover, the model simulations produce weaker convection anomalies along the equator compared with the observation, which can be quantitatively measured by calculating the variance of the individual field accounted for by each EOF. In observations the leading pair of EOFs account for 13%-16% of the variance of the intraseasonally filtered OLR, while only about 5% of OLR variance is explained by the leading EOFs of model simulations. It is a common issue of climate simulations to underestimate the strength of the ISO (Waliser and Coauthoers, 2003; Zhang et al., 2006).

Fig.5.11 shows the lag correlation between the principle components (PCs) of the first two multivariate EOFs for observations, CTL and ZB, respectively. The PCs are maximally correlated at greater(less) than 0.7 (-0.7) when PC1 leads (lags) PC2 by about 10 days. Therefore, the leading multivariate EOFs are a quadrature pair, representing coherent eastward-propagating intraseasonal variability in precipitation and winds along the equator with a period near 40 days. To test if the leading multivariate EOFs derived from bandpass-filtered data represent a physically meaningful mode of variability, we project the leading EOFs derived from the filtered data onto unfiltered data, and then compute the frequency spectrum of the resulting unfiltered PCs (Maloney and Hartmann 1998). The power spectra for observations and simulations are displayed (Fig. 5.12, Fig. 5.13 and Fig. 5.14) It is noted that the observed power spectrum clearly shows a prominent peak at 30-80 days. For the simulations, the dominant power is concentrated within the band of 30-80 days though with a relatively small magnitude. Therefore, the leading EOFs represent a meaningful intraseasonal mode of variability.
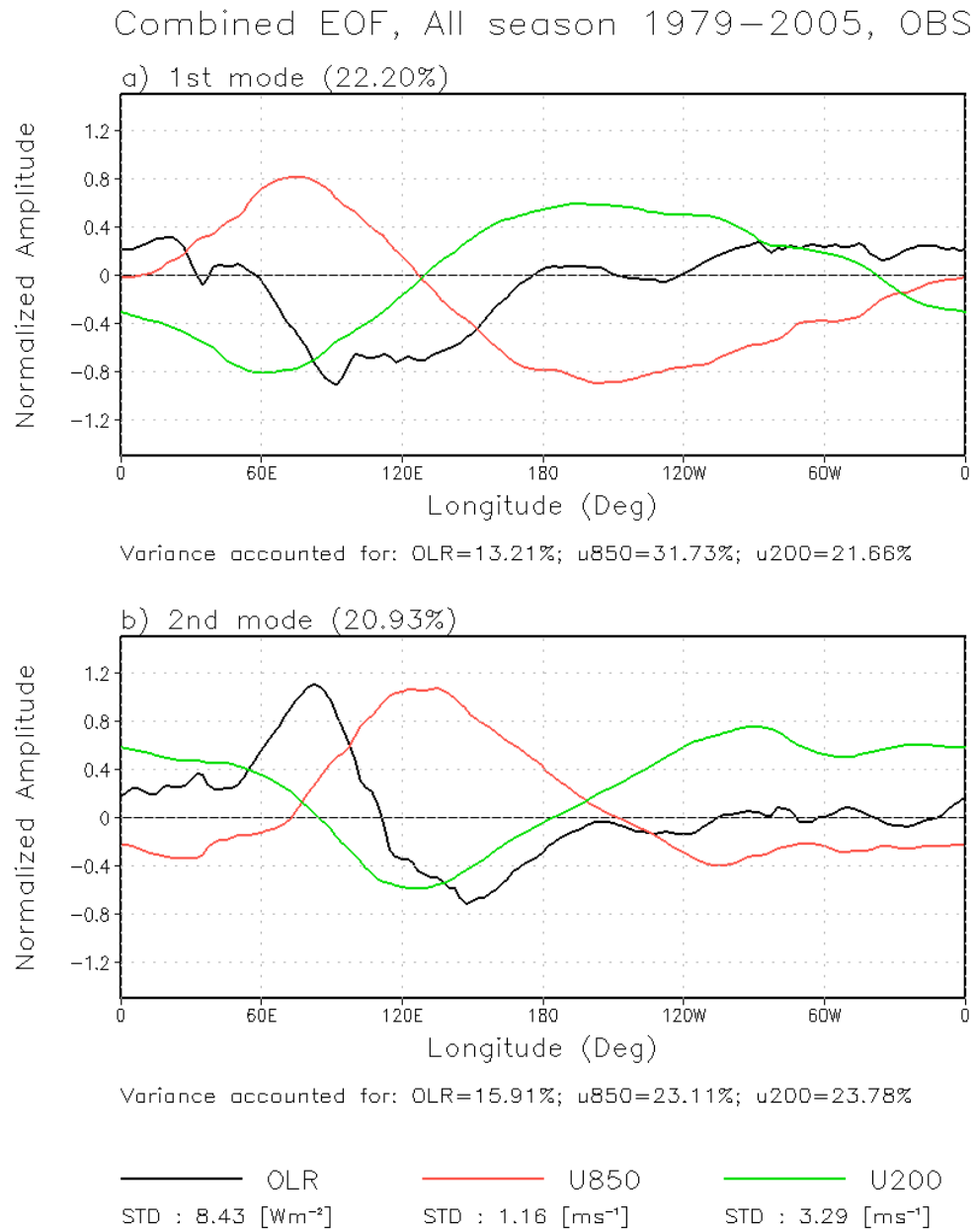
Figure 5.8. All season multivariate combined EOF a) first and b) second modes of 20-100-day 15ºS-15ºN averaged NCEP1 850hPa(red) and 200hPa (green) zonal wind and AVHRR OLR(black). The total variance accounted for by each mode is shown in the top, the variance of each individual field that is accounted for is shown at bottom

Combined EOF, All season, CTL

a) 1st mode (16.14%)

Variance accounted for: OLR=4.82%; u850=25.05%; u200=18.54%

b) 2nd mode (14.15%)

Variance accounted for: OLR=4.92%; u850=21.86%; u200=15.68%

OLR — STD : 10.63 [Wm⁻²]   U850 — STD : 1.56 [ms⁻¹]   U200 — STD : 3.76 [ms⁻¹]
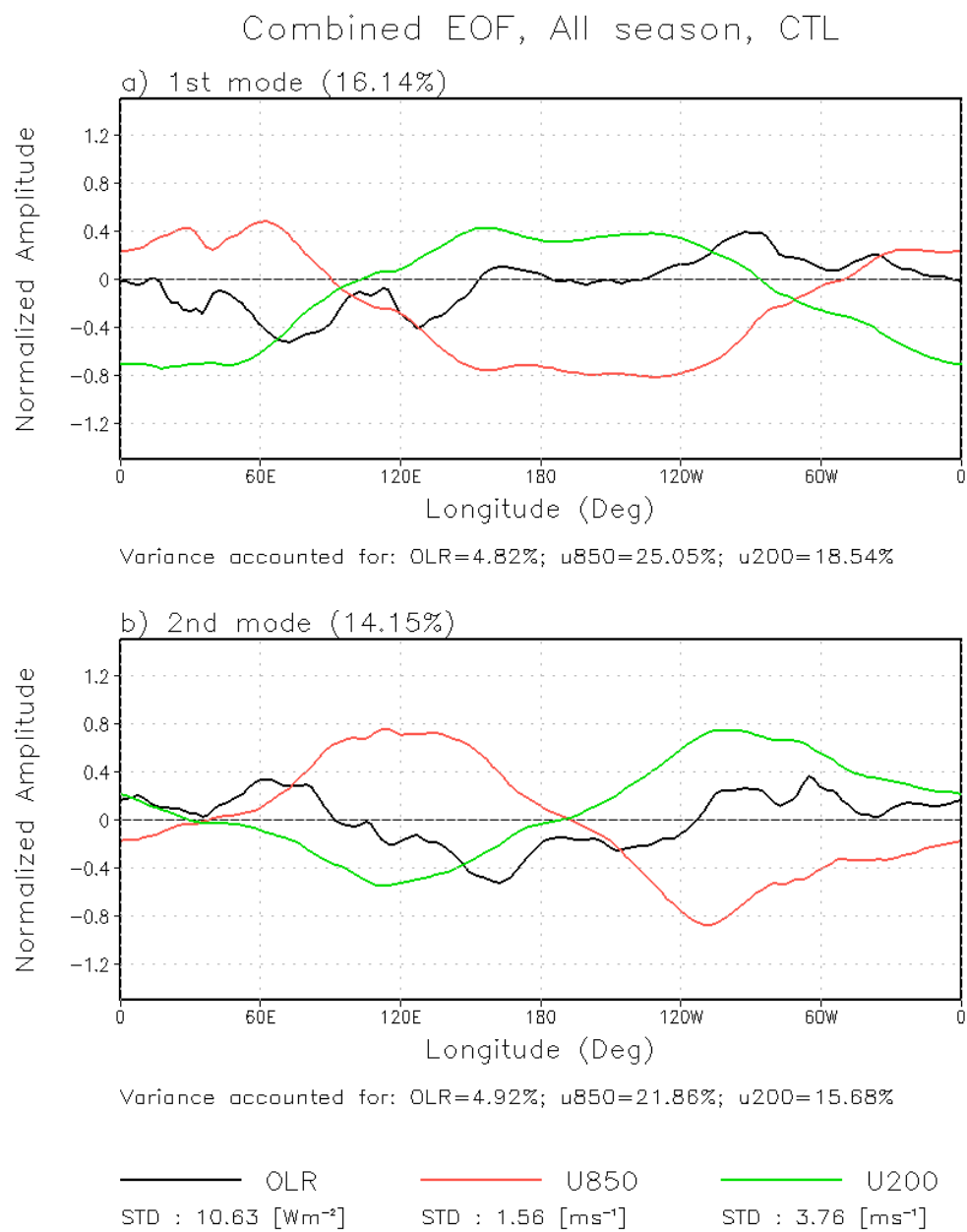
Figure 5.9. As in Fig. 5.8 but for CTL run

Combined EOF, All season, ZB

a) 1st mode (16.49%)

Variance accounted for: OLR=5.35%; u850=27.65%; u200=16.46%

b) 2nd mode (14.36%)

Variance accounted for: OLR=5.06%; u850=20.75%; u200=17.27%

—— OLR	—— U850	—— U200
STD : 10.24 [Wm^{-2}]	STD : 1.52 [ms^{-1}]	STD : 3.67 [ms^{-1}]
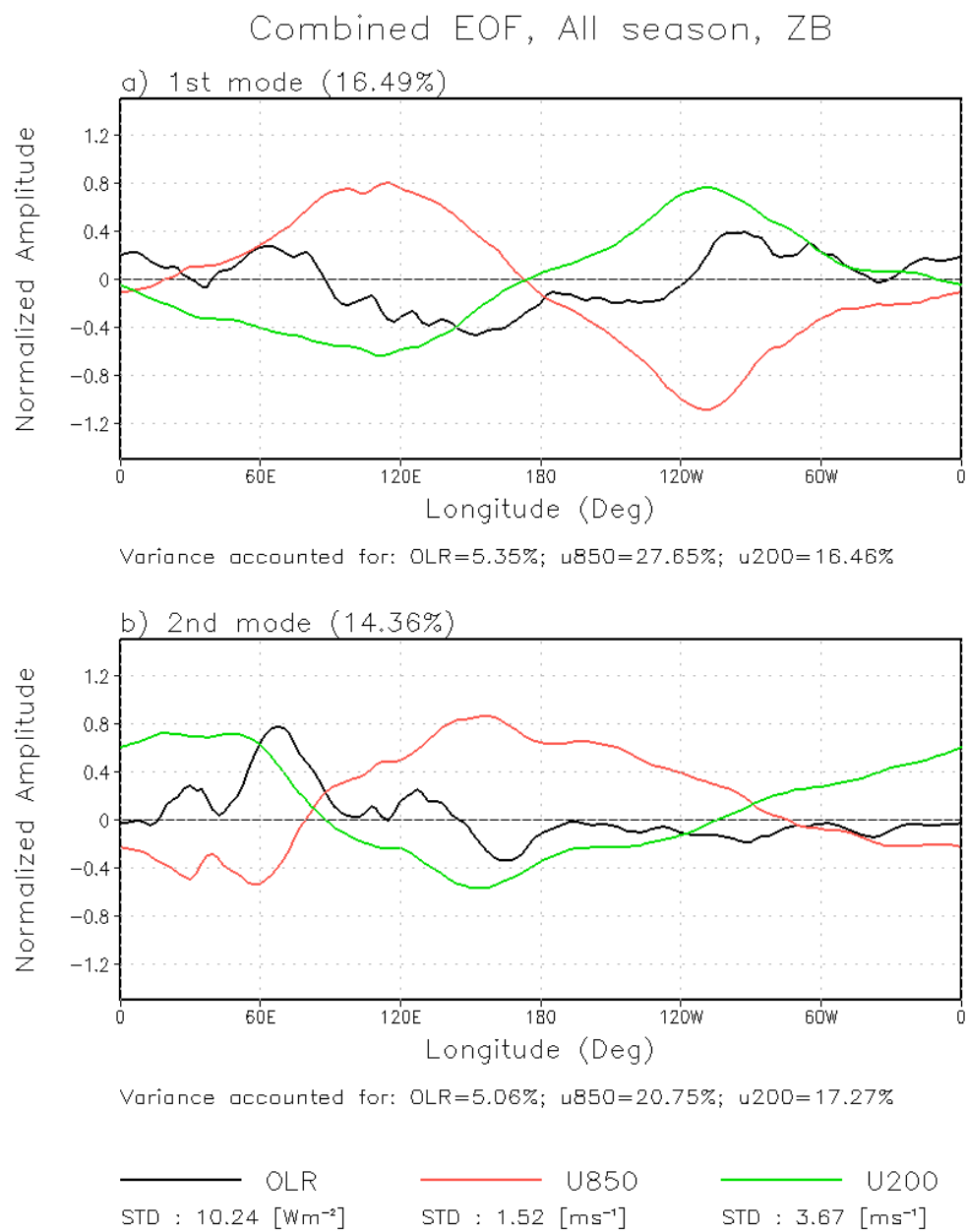
Figure 5.10. As in Fig. 5.8 but for ZB run
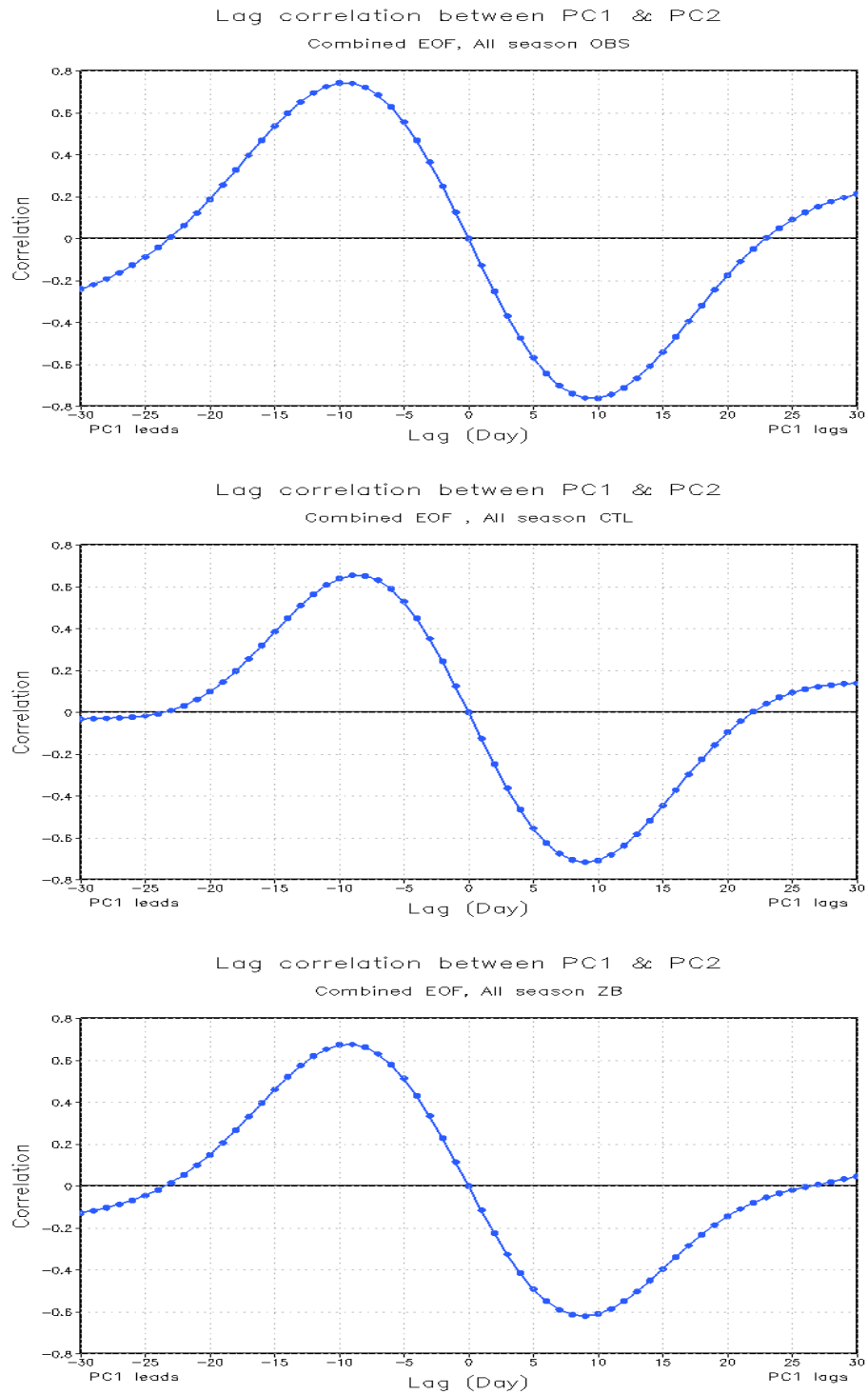
Figure 5.11. The lag correlation of the leading pair of principle components of multivariate combined EOF for a) observations, b) CTL run, and c) ZB run
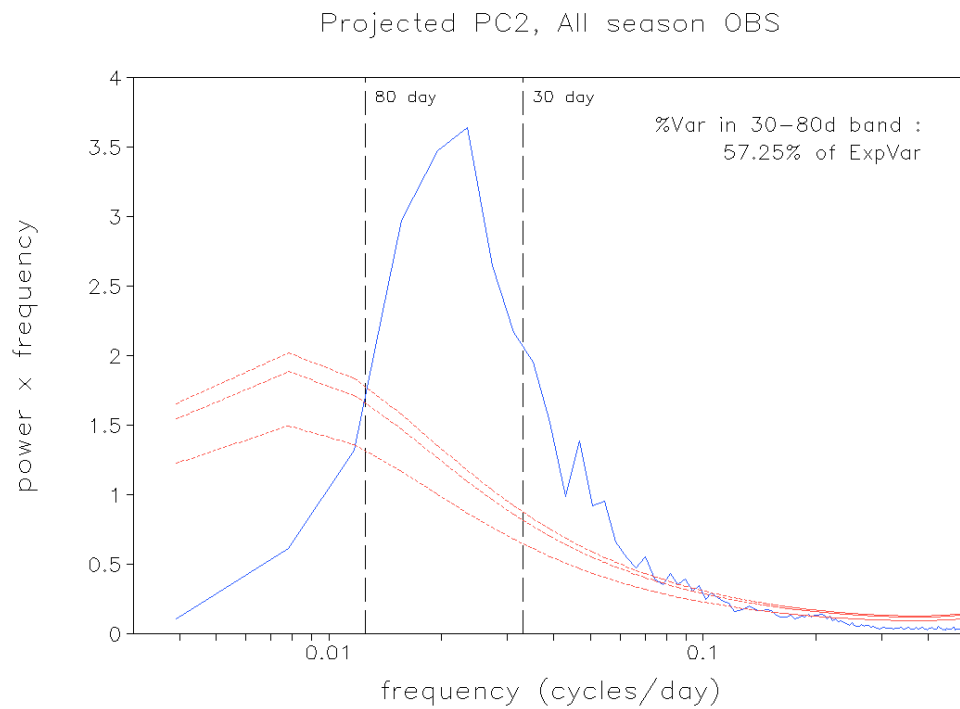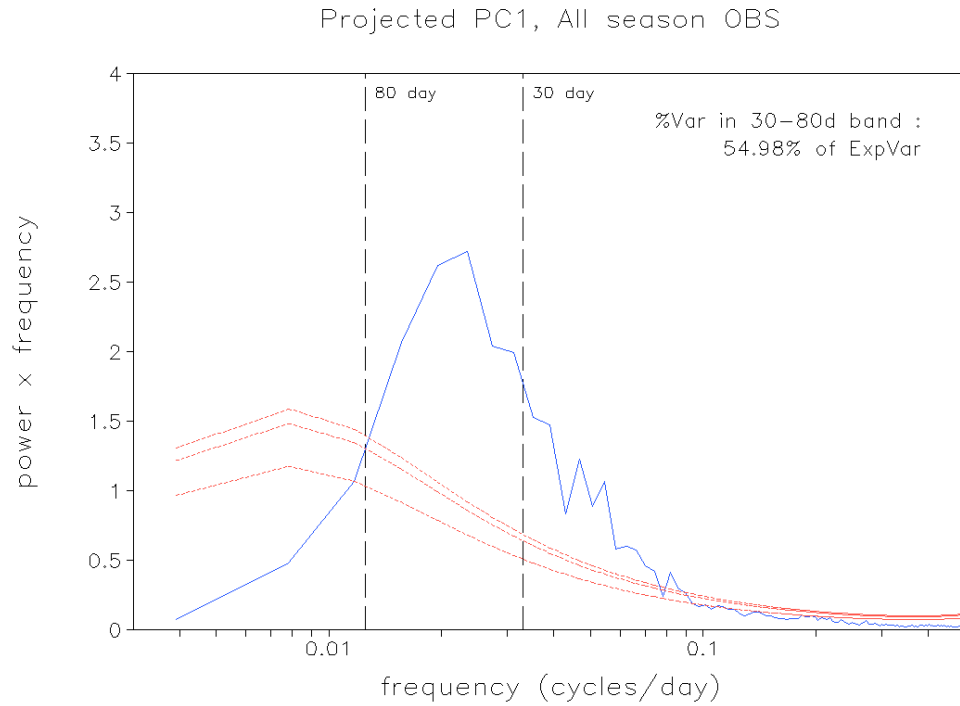
Figure 5.12. The power spectrum of the unfiltered a) PC1 and b) PC2 derived by projecting combined EOF onto the unfiltered data matrix of observations. Red lines show the red noise spectrum and upper 90% and 95% confidence levels.

101

Projected PC1, All season CTL

80 day   30 day

%Var in 30−80d band :
47.06% of ExpVar

Projected PC2, All season CTL

80 day   30 day

%Var in 30−80d band :
39.26% of ExpVar
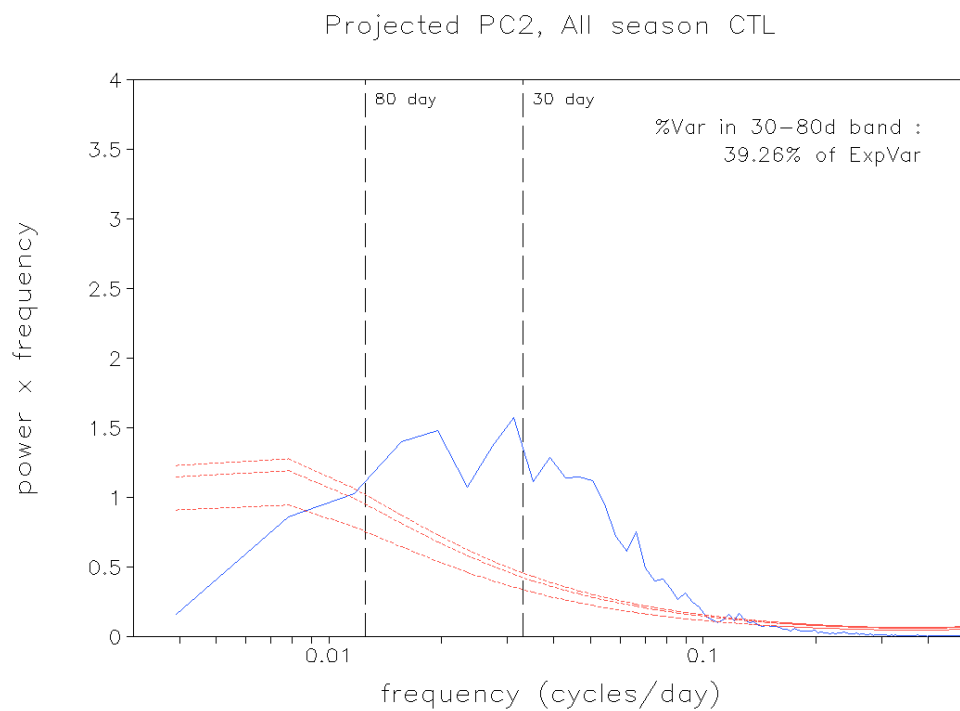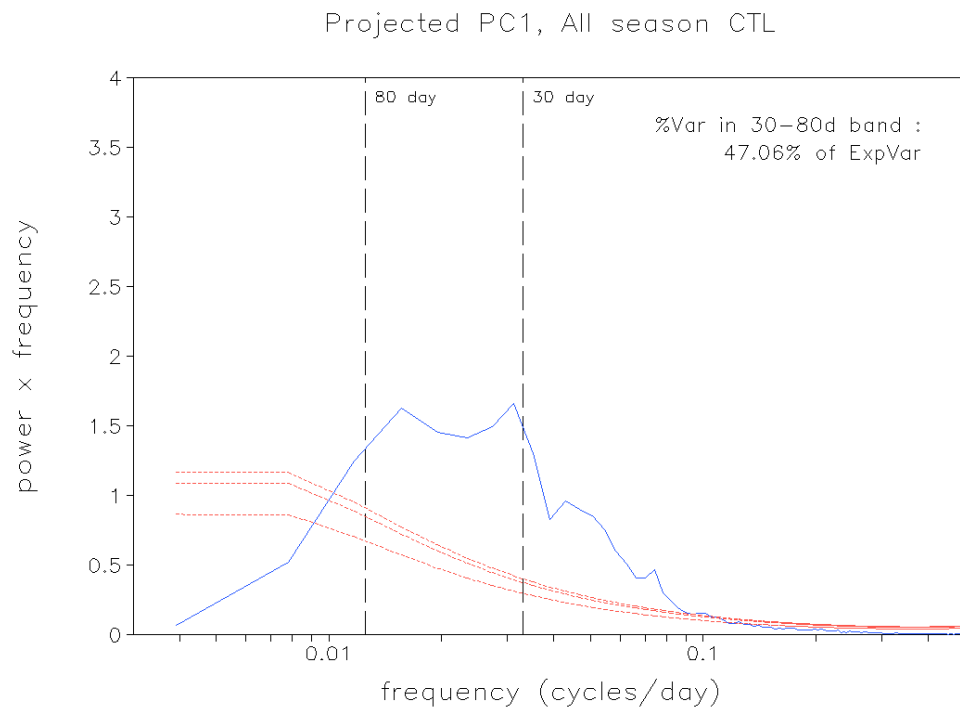
Figure 5.13. As in Fig. 5.12 but for CTL run

Projected PC1, All season ZB

%Var in 30−80d band :
41.28% of ExpVar

Projected PC2, All season ZB

%Var in 30−80d band :
44.26% of ExpVar
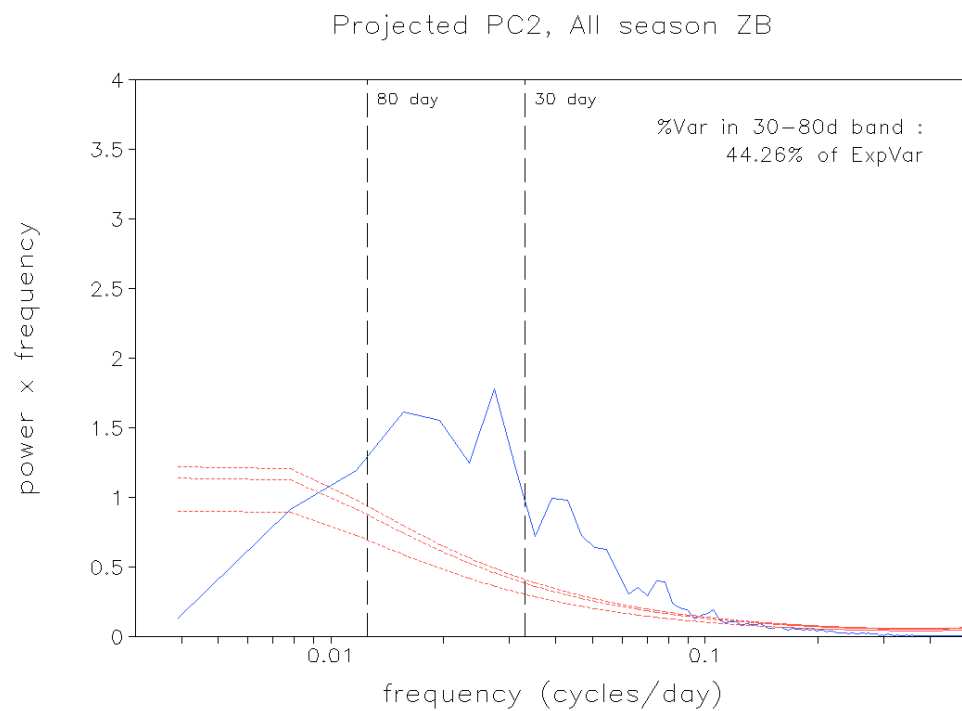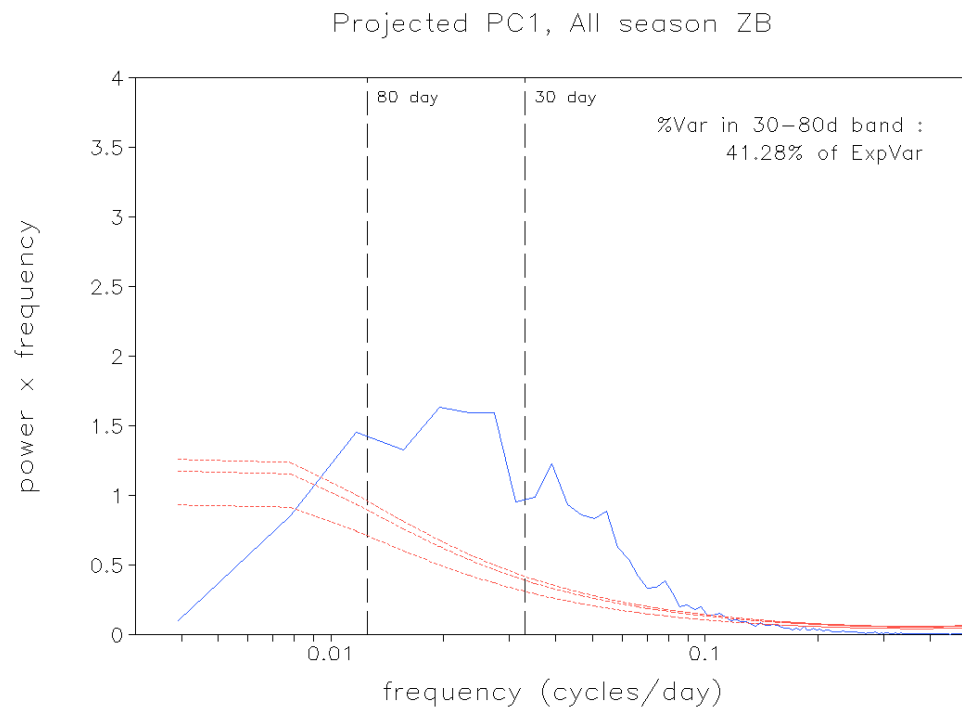
Figure 5.14. As in Fig. 5.12 but for ZB run

Based on the multivariate EOF analysis, we can further derive an ISO life cycle composite of model results for boreal winter or boreal summer to explore the spatial-temporal structure of intraseasonal variability. The life cycle of ISO can be divided into eight phases based on the inverse tangent of the ratio of PC2 to PC1 of multivariate EOFs. For each phase, a composite is generated by averaging across all days that exhibit a relatively strong ISO signal, and the ISO is defined to be significant during periods when $PC1^2+PC2^2$ is above 1 (where PC1 and PC2 each have unit standard deviation) (Wheeler and Hendon, 2004).

A composite life cycle of intraseasonal OLR and 850hPa wind anomalies from ZB and CTL runs for boreal summer is shown in Fig. 5.15, and the corresponding boreal winter composite is displayed in Fig. 5.16. The average duration for each phase is about 6 days. Although the composite is based on the PCs that are independent of season, the pronounced seasonality of ISO is still apparent in off-equatorial fields.

The boreal-summer composite (Fig. 5.15) mainly features the northward and eastward propagation of the convection in the Indian Ocean basin. In phase 1, a decaying convection (positive OLR anomalies) is present in the southern Indian Ocean, while enhanced convection (negative OLR anomalies) the Arabian Sea, the Bay of Bengal and its extension into the western Pacific Ocean. Over subsequent phases, the convection further decays in the Indian Ocean and moves to the east, and the value of positive OLR anomalies is increasing until spreading over the regions including the Indian and western Pacific Oceans (phases 2 to 4). Then, the enhanced convection (negative OLR anomalies) is triggered over the southern Indian Ocean (phase 5). The convection is further developed and propagates (phases 6 to 8) to form a whole life cycle of ISO activity. Both simulations show a reasonable phase relationship between the spatial structures of the convection and lower-tropospheric wind (Kemball-Cook and Wang 2001; Lawrence and Webster 2002; Wheeler and Hendon 2004). This can be seen in the easterly wind anomalies into India and the Bay of Bengal ahead of the convection (phases 5 to 8), and the westerlies within and behind the enhanced convection (phases 7,8 and 1).
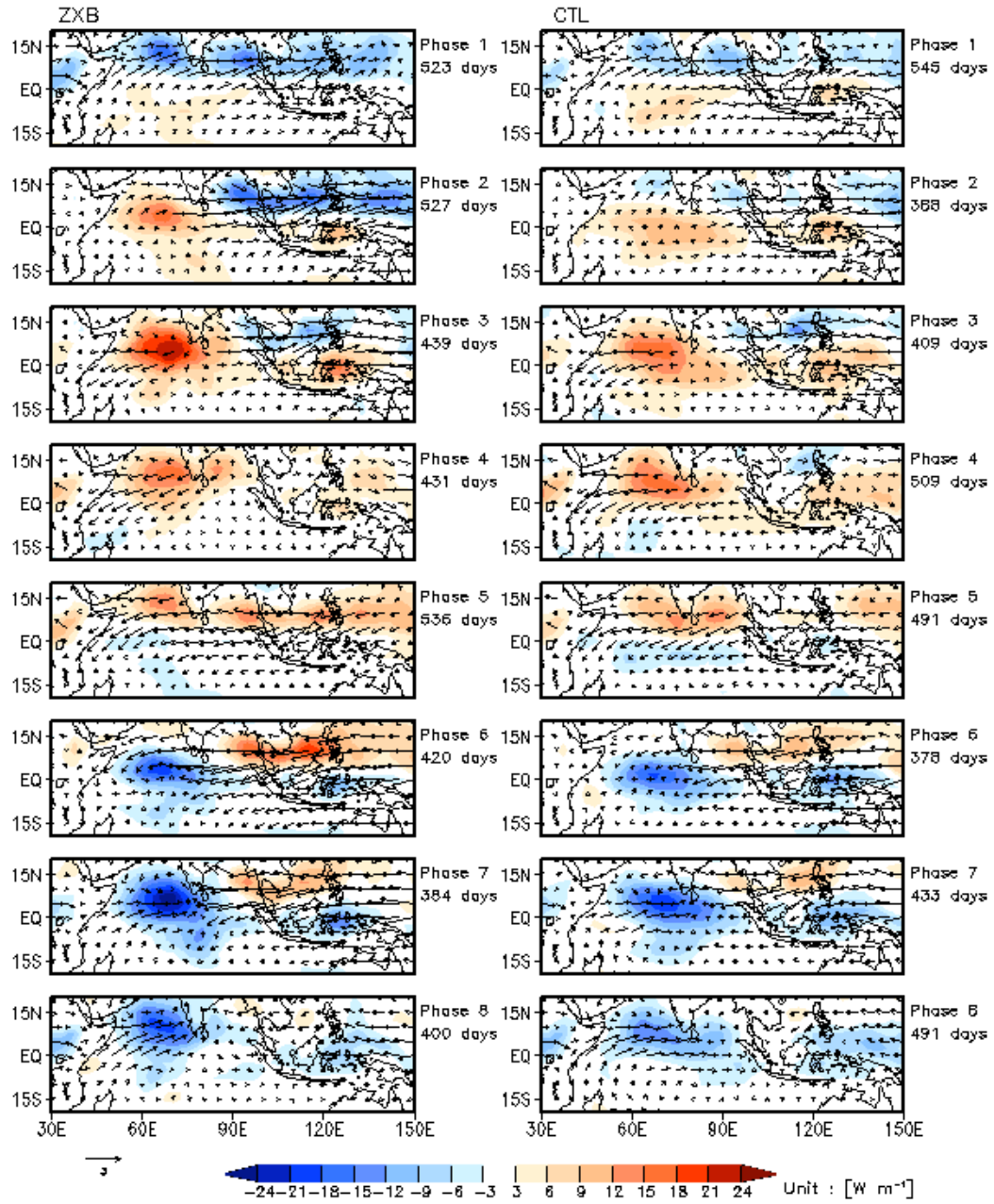
Figure 5.15. May-October composite of 20-100-day OLR (shaded) and 850hPa wind anomalies (vector) as a function of MJO phases for ZB run (left column) and CTL run (right column). The number of days used to generate the composite for each phase is shown to the right of each panel
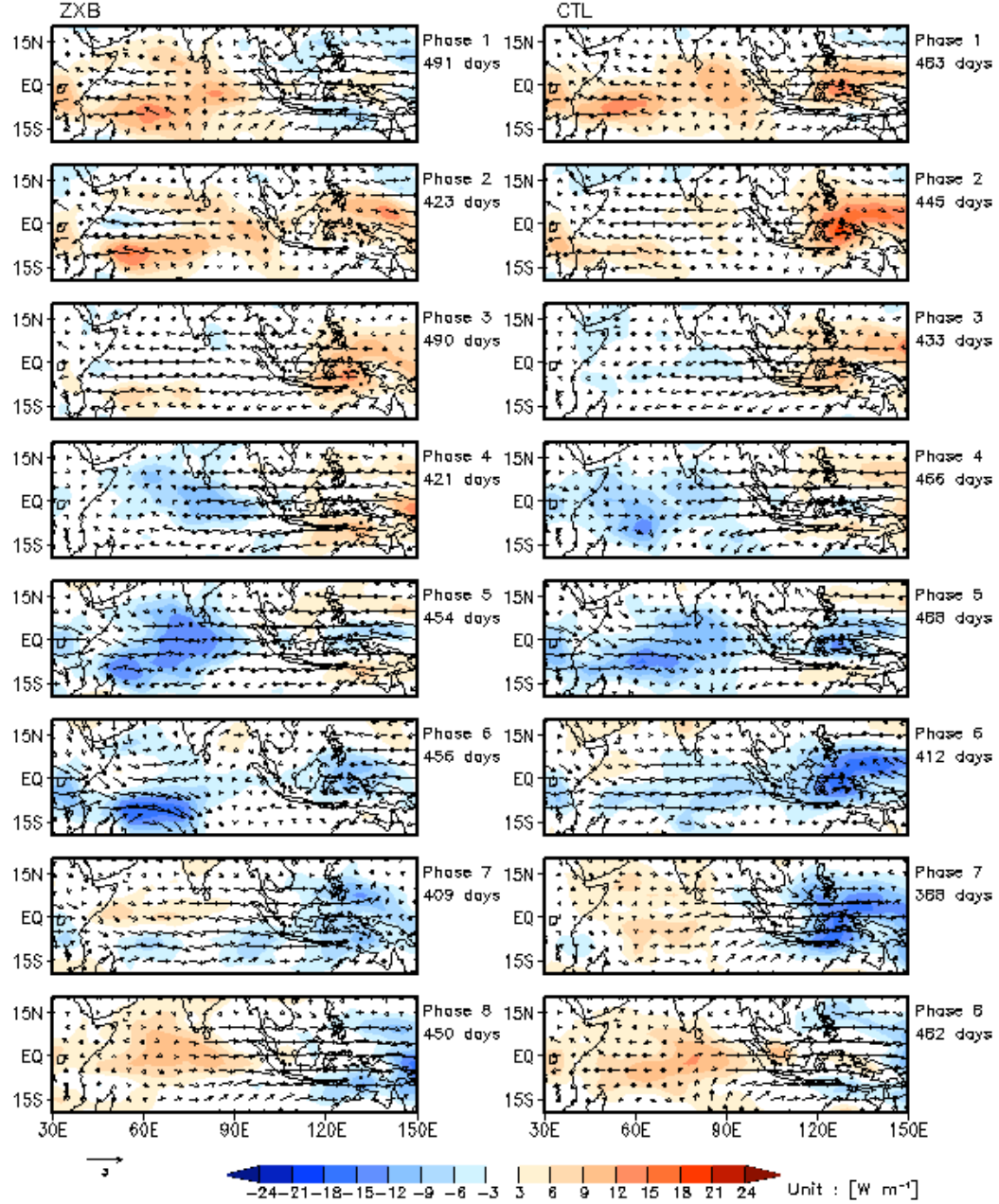
Figure 5.16. As in Fig. 5.15 but for boreal winter (November-April)

The winter-season composite reveals the decay and enhancement of convection over the Indian Ocean and the Maritime Continent, mostly near the equator (Fig. 5.16). However, the eastward propagation as a primary observed characteristic of the ISO is lacking of representation in the model simulations, especially over the Indian Ocean. The enhanced convection anomalies form at the south of the Indian semi-continent in phase 4. Then the anomalies intensify, and move southwest to produce an artificial center near the Madagascar where the convection has a larger amplitude than the convection over the Maritime Continent. Therefore, the eastward propagation of the convection is visually concealed in the composite. We hypothesize that the erroneous enhancement of the convection over the western Indian Ocean is likely due to errors in the model mean state of SST which shows the warm bias over the region during the boreal winter (Fig. 5.1a).

Besides the common features of ISO revealed in both the ZB and CTL runs as mentioned above, we also notice the influence of diurnal SST variation on the amplitude of intraseasonal variability. The OLR anomalies are generally larger in the ZB run than that in the CTL run, which indicates the diurnal SST variability simulated by the ZB experiment tends to enhance the convection anomalies on the intraseasonal time scale. The intensification occurs prominently in boreal summer, as every phase of the life cycle composite have larger anomalies in the ZB run (Fig. 5.15). It is also observed in phase 5 and phase 6 of the boreal winter composite (Fig. 5.16). Consistent with the intensification of the intraseasonal convection anomalies, the composites of precipitation and 10-meter wind speed (Figures not shown) also indicate the larger anomalies in the ZB run comparable to the result from the CTL run. Therefore the confidence is increased that the diurnal SST variability in the ZB experiment systematically modifies the atmospheric variability on the intraseasonal time scale.

To further investigate the possible mechanism of this influence, we conduct the composite on other variables such as the diurnal SST variability (DSST, Fig. 5.17 and Fig. 5.18) and sea surface temperature (SST, Fig. 5.19 and Fig. 5.20). As expected, the DSST shows little intraseasonal anomalies in the CTL run since the SST diurnal cycle is not represented
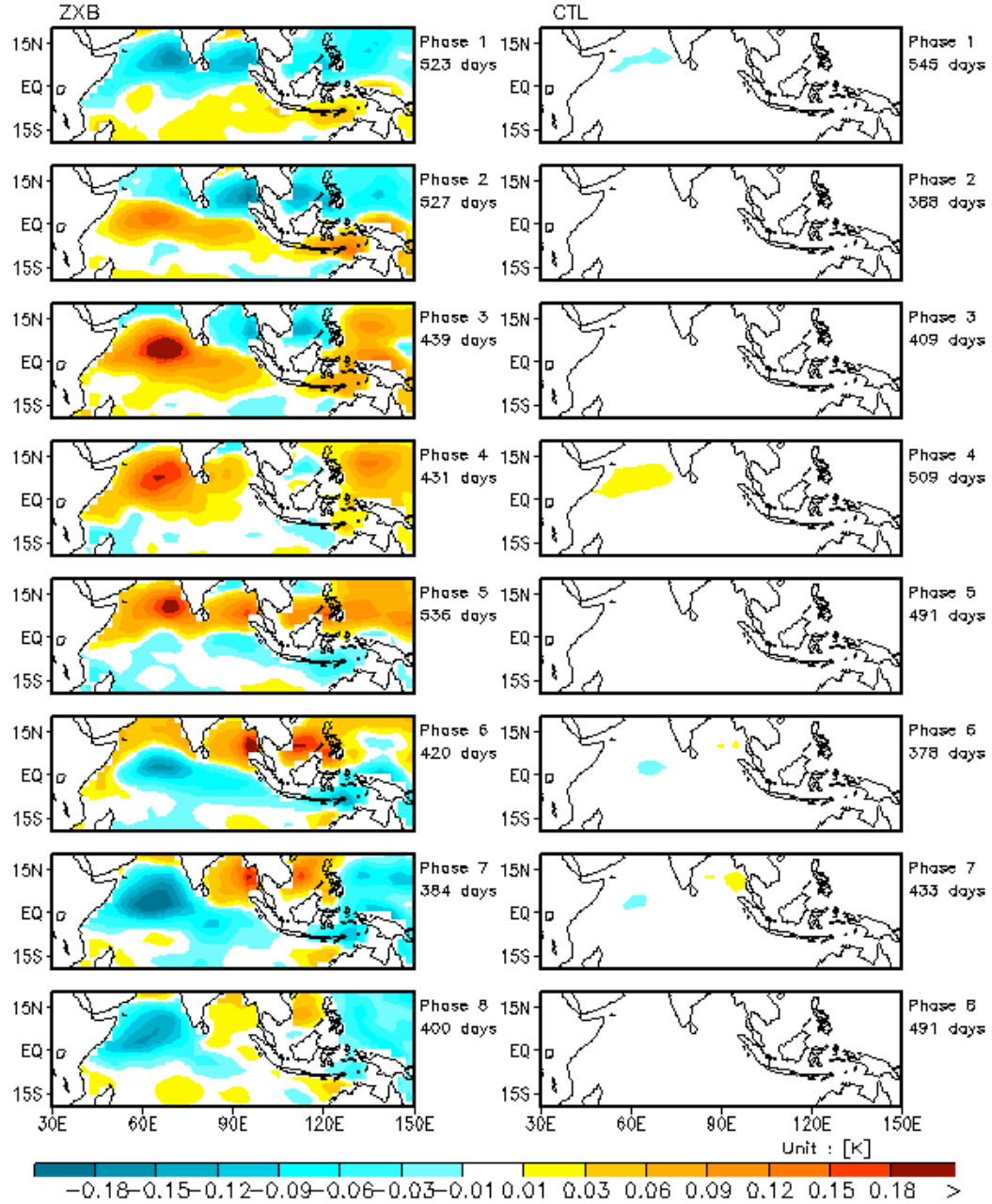
Figure 5.17. May-October composite of 20-100-day diurnal SST (DSST) anomalies as a function of MJO phases for ZB run (left column) and CTL run (right column). The number of days used to generate the composite for each phase is shown to the right of each panel
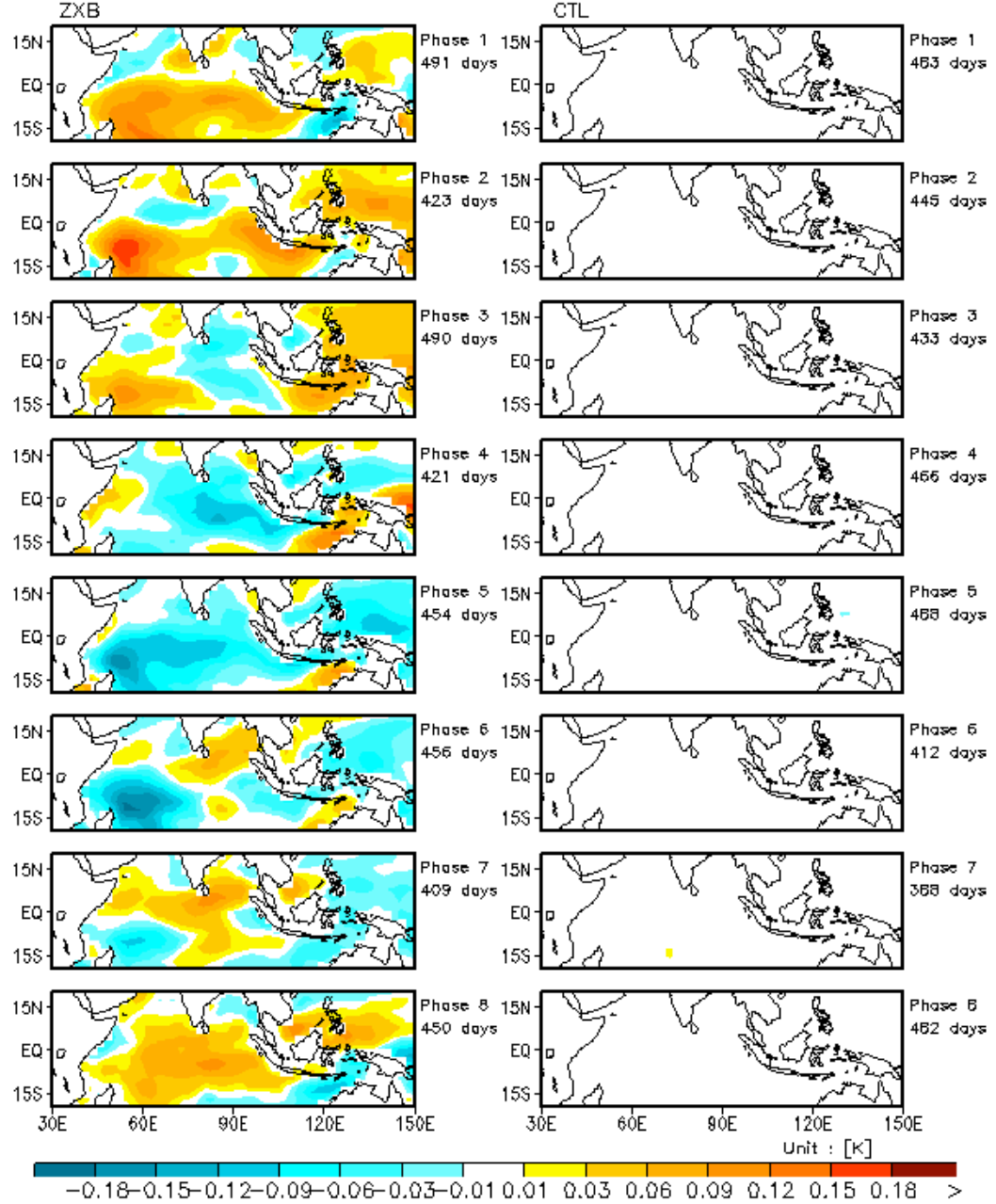
Figure 5.18. As in Fig. 5.17 but for boreal winter (November-April)
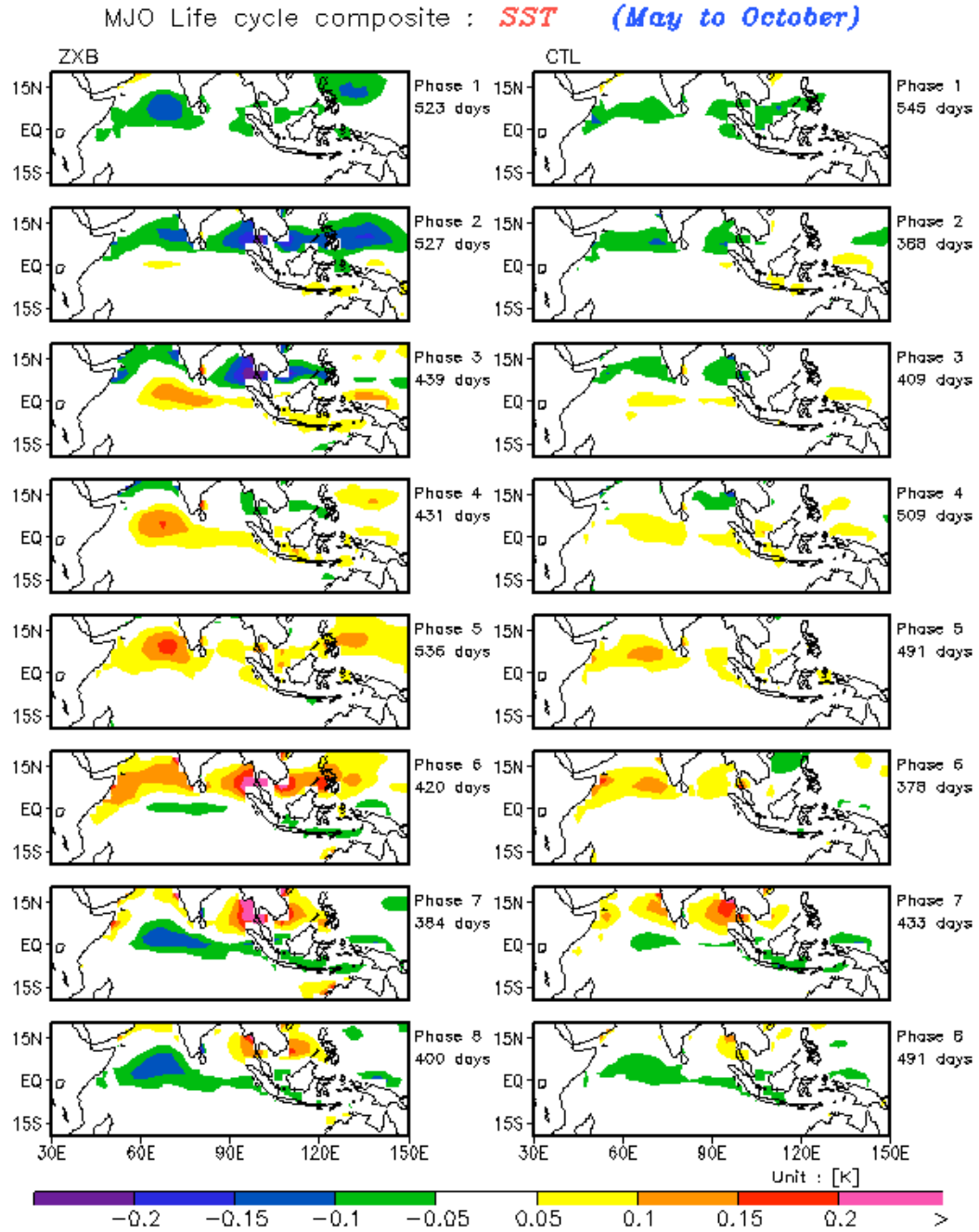
Figure 5.19. May-October composite of 20-100-day SST anomalies as a function of MJO phases for ZB run (left column) and CTL run (right column). The number of days used to generate the composite for each phase is shown to the right of each panel
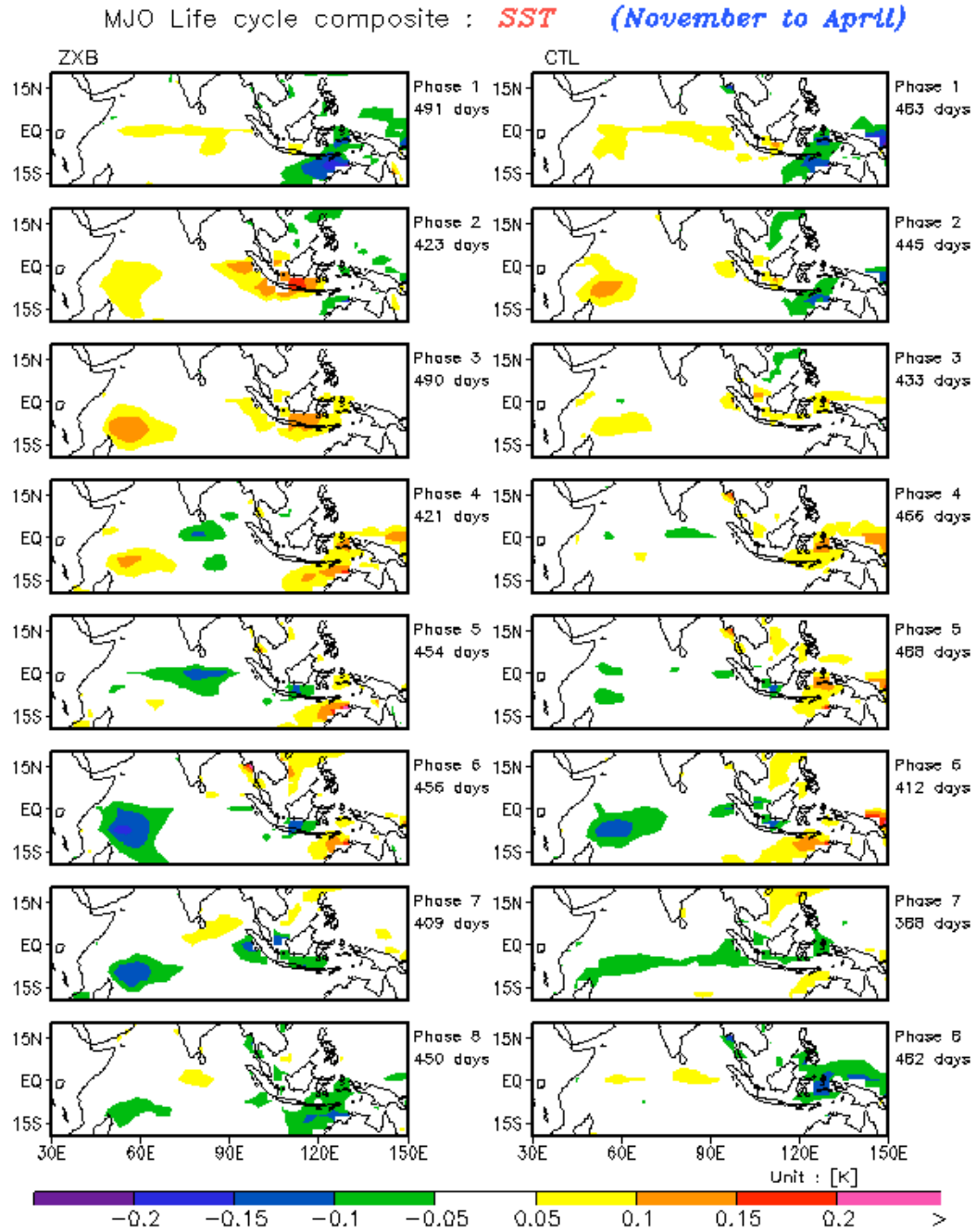
Figure 5.20. As in Fig. 5.19 but for boreal winter (November-April)

in the simulation. But in the ZB run, the DSST composite shows organized intraseasonal anomalies throughout the life cycle of ISO for both boreal winter and summer seasons. During boreal summer, the negative diurnal SST anomalies is seen in the northwest Pacific Ocean and the northern Indian Ocean with the largest value located in the Arabian Sea and the Bay of Bengal, while the positive diurnal SST anomalies start forming over the south of the equator (Fig. 5.17, phase 1 in the ZB run). The positive anomalies gradually increase and move northward across the equator in phase 2, and the centers of negative anomalies show the eastward propagation at the same time. In phase 3, the positive diurnal SST anomalies present in most of the areas over the Indian Ocean and the northwest Pacific, it reaches the maximum value over the south of the Arabian Sea. The negative anomalies are confined to the Bay of Bengal and west of Philippines, which are further weakening until the positive anomalies dominate the whole region in phase 4. Phases 5 to 8 show the similar processes with the anomalies patterns featuring the opposite sign. For the boreal winter (Fig. 5.18), the positive diurnal SST anomalies mainly locate over the south of the equator in the Indian Ocean at phase 1. Then the positive anomalies strengthen and form two centers in the north of Madagascar and the west of Indonesia, respectively. The negative anomalies start representing over north of the equator in the Indian Ocean at phase 2. In phase 3, the positive anomalies in the eastern part of Indian Ocean propagate eastward and the negative anomalies dominate the region instead. Meanwhile, the center of positive anomalies over the western basin of Indian ocean decay locally and be gradually replaced by the negative anomalies in the following phases.

A closer comparison between the DSST composite (Figs. 5.17 and 5.18) and OLR/wind composites (Figs. 5.15 and 5.16) reveals the influence of atmospheric variability on the DSST variation. The positive DSST anomalies show coincidently with the suppressed convection and reduced wind speed, and vice versa. Such a relationship is consistent with the previous results with the favorable conditions of the large amplitude of diurnal SST variability. Meanwhile, a further inspection of the phase relationship between the DSST and SST composites in the ZB run indicates that the DSST anomalies tend to lead the SST

anomalies (Figs. 5.19 and 5.20). For example, during boreal summer the maximum positive DSST anomalies occur over the south of the Arabian Sea in phase 3 of the composites (Fig. 5.17), and the largest SST anomalies are presented in phase 5 of the SST composites at the same location consequently (Fig. 5.19). Similar coherent patterns are also presented in the boreal winter composites for DSST and SST. For instance, the large DSST anomalies located over the north of Madagascar in phase 2 of the composites (Fig. 5.18), while the strong SST anomalies is shown at the same region in phase 3 of the SST composites (Fig. 5.20). Similarly, the negative DSST anomalies tend to lead the SST decline in the following phase. For example, the negative DSST anomalies in phase 1 of DSST composites (Fig. 5.17) are coincident with the negative anomalies in phase 2 of SST composites (Fig. 5.19) during boreal summer.

It needs to be pointed out that the SST composite in the ZB run is also intensified compared with the CTL run, especially for the boreal summer (Figs. 5.19 and 5.20). We believe that it's more direct connected with the implementation of the diurnal SST variability. As suggested in many previous studies, significant lead-lag correlation exist between intraseasonal precipitation and SST (Woolnough et al. 2000; Hendon 2000; Pegion and Kirtman 2008). We also notice that in both ZB and CTL runs, warm SST anomalies lead the maximum precipitation by about 10 days (two phases) and cold SSTAs lag the precipitation anomlies by about 10 days in the Indian Ocean and over the Maritime Continent.

In a summary, this is the likely scenario to describe the effect of the diurnal SST variability on the tropical intraseasonal variability: The strong SST diurnal cycle forms and lasts under the favorable atmospheric conditions during the suppressed phase of ISOs. The large DSST anomalies then leads to the intensified SST warm anomalies. As a result, the warm SST anomalies may trigger the stronger convective precipitation in the followed active phases of ISOs through preconditioning the surface moisture and moist static energy by the enhancement of surface evaporations. In turns, the intensified convections will lead to the negative anomalies of DSSTs and SSTs during the life cycle of ISOs.

We also notice that diurnal SST variability primarily intensifies the amplitude of atmospheric anomalies for ISO events in our simulations. However the simulation of the ISO events in the ZB run still suffer from unrealistic spatial distributions and propagating features, because the current model is lack of ability to reproduce the reasonable ISO signals. This is due to complicated reasons, such as the biases in the mean background state, improper convectional parameterization, and unrealistic air-sea feedbacks. These biases are not likely to be reduced significantly by only introducing diurnal SST variability in the model.

5.3 upscale feedback of the diurnal SST variability

Previous section illustrate that the diurnal SST variability may qualitatively affect the intraseasonal variability which can be seen by the intensified intraseasonal anomalies of SST, precipitation and surface winds. Furthermore, based on previous studies (Slingo et al. 2003, Zhou and Li 2010), we believe that the enhanced surface evaporation that results from the positive diurnal SST anomalies during the suppressed phases of ISOs may be important for the convective preconditioning in readiness for the next active phase. The life cycle composite of the latent heat flux (LHF) also shows the intensified latent heat loss from the ocean to atmosphere in ZB run comparing with the CTL run (figures not shown). In the following part, we attempt to quantitatively diagnose how the diurnal SST variability may impact the ISO, especially to nonlinearly rectify the intraseasonal latent heat flux (LHF).

The surface LHF may be calculated according to the bulk formula as (Weare et al., 1981; Chu and Frederick, 1990)

$$\text{LHF} = L\rho|C_E|\mathbf{V}|(q_s - q_a) \tag{5.1}$$

Where L is the latent heat of condensation; ρ is the air density at the standard sea level; C_E is a constant exchange coefficient whose value is determined to guarantee the LHF calculated from the bulk formula has the minimum errors from the model outputs;

q_s is the sea surface specific humidity derived from the SST and sea level pressure of the model results, q_a is the model outputs of 10-meter specific humidity.

Following the analysis method proposed by Zhou and Li (2010), the zonal and meridional winds, and air-sea humidity difference fields are decomposed into three components: the background mean state, the diurnal scale component(0-5 days), and the intraseasonal component (20-100 days). The climatological annual cycle of each variable is used to represent the background state. For instance, the zonal wind can be decomposed as

$$u \approx \bar{u} + \tilde{u} + u' \tag{5.2}$$

where $\bar{u}$ is the mean state, $\tilde{u}$ is the intraseasonal variability and u' is the high frequency component.

If we insert the components of u, v and Δq into the bulk formula and conduct band-pass filtering on intraseasonal scale, the intraseasonal variability of LHF are predominately contributed by two parts, i.e. :

$$\widetilde{\text{LHF}} \approx L\rho C_E(|\tilde{\mathbf{V}}|\tilde{\Delta} q + \widetilde{|\mathbf{V'}|\Delta q'}) \tag{5.3}$$

The first term represents the intraseasonal anomalies of LHF resulting from the intraseasonal variability of wind and humidity difference, and second term indicates the nonlinear rectification of intraseasonal LHF induced by the high frequency variability. We will focus on the contribution of nonlinear rectification term by evaluating its ratio to the total LHF intraseasonal variance.

For boreal winter (Nov-Apr, Fig. 5.21) and summer (May-Oct, Fig. 5.22), respectively, two intraseasonal LHF fields are calculated from the ZB experiment. First, the LHF is calculated based on the sum of all three components which is approximately equal to the model generated LHF, then the 20-100-day band-pass filtering is conducted to isolate the intraseasonal signal. The standard deviation is displayed to reflect the strength of the total intraseasonal LHF field (Figs. 5.21a and 5.22a). Note that the tropical Indian and western

Pacific oceans are covered by large LHF variability, especially concentrated in the Arabian Sea and the Bay of Bengal during boreal summer and over north and northeast of Australia in boreal winter.

Second, the LHF is calculated based on the sum of only the background mean state and the diurnal scale component without involving the intraseasonal component, and the same 20-100-day filter is applied. The standard deviation of the intraseasonal LHF calculated this way reflects the nonlinear rectification because of the diurnal-mean state interaction (Figs. 5.21b and 5.22b). Similar to the total LHF, we find large variability over the Indian and western Pacific Oceans. However, this nonlinearly rectified LHF shows that the maximum variation tends to be organized in the summer hemisphere.

By comparing the standard deviation derived from two approaches mentioned above, we may evaluate the contribution from the diurnal-mean flow interaction to the total intraseasonal LHF. Figs. 5.21c and 5.22c show the ratio of the two standard deviations for boreal winter and summer, respectively. The large ratios exceeding 30% are observed over the tropical Indian and western Pacific oceans for both seasons, indicating that over theses regions, the diurnal-scale motion greatly feeds back onto the intraseasonal surface LHF. Maximum diurnal contributions may exceed 60% over the Arabian Sea and the Bay of Bengal throughout the year, and similar amount of contribution near the Sumatra and over the Java Sea in boreal winter. In general, the strong nonlinear rectification is coherent with the large intraseasonal variability.

We conducted a similar analysis for the CTL run to evaluate the diurnal-scale contribution on the intraseasonal LHF fields. Figs. 5.21d and Fig. 5.22d show the comparison between ratios of the nonlinear rectification over the total fields for the ZB and CTL runs. Overall, the diurnal contribution is significantly stronger over the Maritime Continent in the ZB run compared to those of the CTL run.
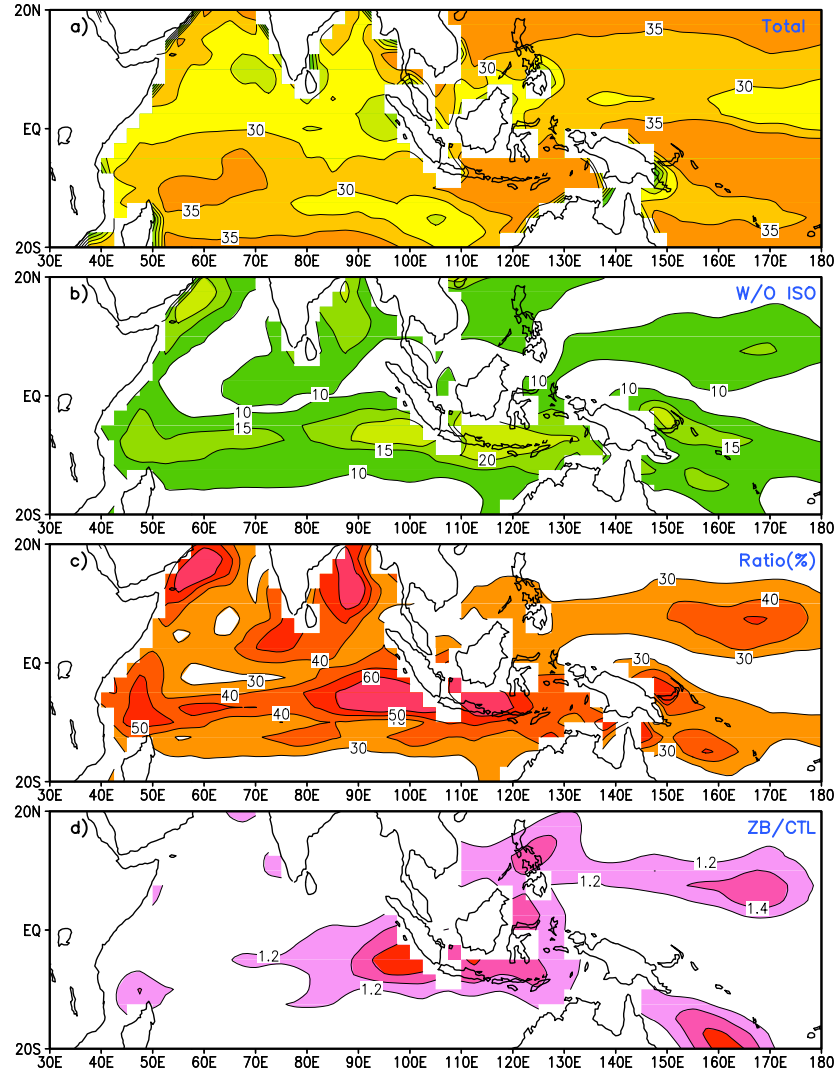
Figure 5.21. The standard deviation of 20-100-day latent heat flux (LHF) anomalies in ZB run during boreal winter calculated from a) the sum of background state, the diurnal component and the intraseasonal compnents, b) the sum of background state and the diurnal component. The ratio of standard deviation computed as above is shown in c) to measure the nonlinear rectification of diurnal scale variability. Similar ratio is calculated for CTL run and is compared with ZB run as shown in d)
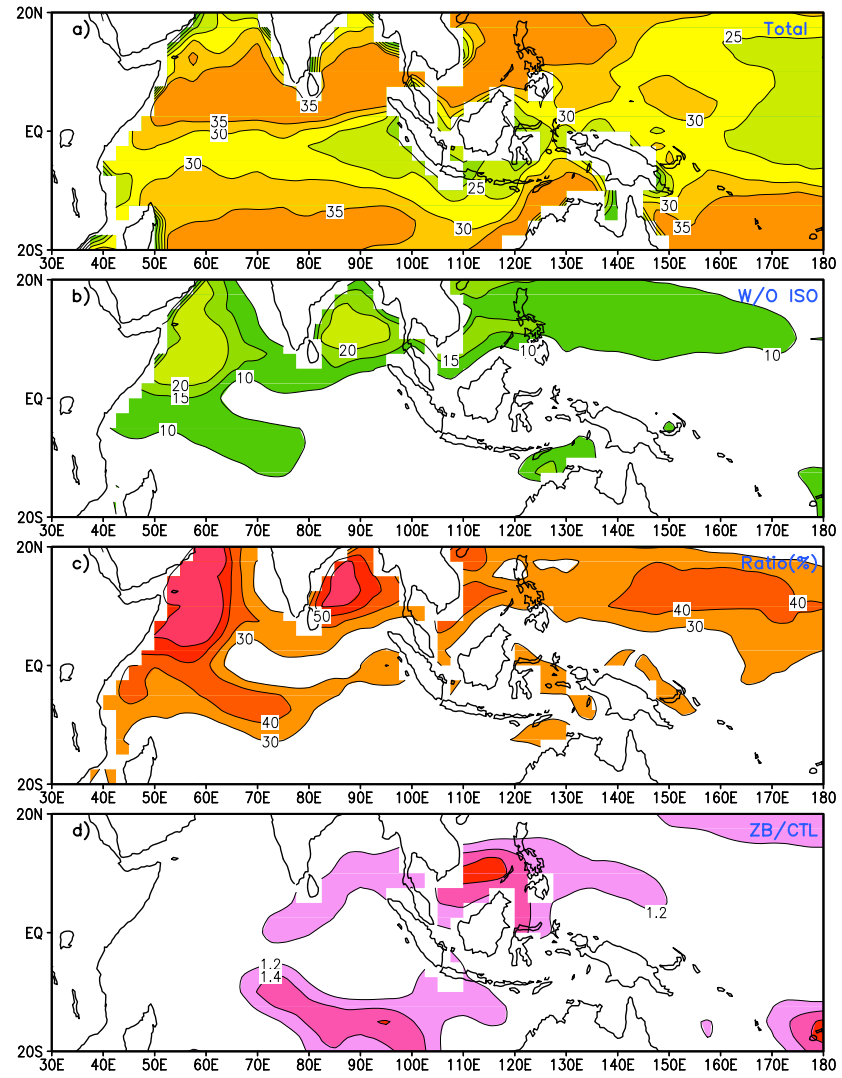
Figure 5.22. As in Fig. 5.21 but for boreal summer (May-October)

Chapter 6: Summary and Discussion

6.1 Results of the research

The diurnal variability is one of the dominant variations in SST. Many researchers have recently become interested in the diurnal SST variability, and a number of studies reveal the importance of its effects on the atmospheric variability, especially on the intraseasonal time scale. But the SST diurnal cycle is not represented in most of the current coupled general circulation models (CGCMs) which are generally used for the research of climate variability. To efficiently reproduce the diurnal SST variability in the CGCM and further investigate its potential influence on the intraseasonal variability, two one-dimensional mixed layer parameterizations, respectively developed by Zeng and Beljaars (ZB, 2005) and Schiller and Godfrey (SG, 2005) respectively, are applied to the NCEP Climate Forecast System (CFS).

Both parameterizations have not yet been fully tested in the coupled model, and therefore the first part of this research is to evaluate how well the diurnal mixed layer parameterizations can improve the diurnal SST variability in the CFS. The assessment is conducted using several measures. The point-by-point comparison between the model simulations and the in situ observations is performed, and a novel data analysis method (EEMD) is employed to identify the diurnal mode of the SST time series. Results reveal the parameterizations produce great improvement in simulating the SST diurnal cycle at every selected position. In particular, the ZB scheme generates a realistic amplitude of diurnal SST, while the SG scheme provides relatively weaker diurnal variation. Observations also indicate that the diurnal SST variability is not always keeping the same strength but is being significantly modified by the local weather conditions, and therefore the amplitude of SST diurnal cycle is intermittent. This intermittency is well captured by both parameterizations. The strong

diurnal SST in the simulations is associated with the favorable meteorological conditions of high solar insolation and low wind speed, while cloudiness and strong surface winds usually eliminate the daytime warming of SST. In general, surface winds primarily determine the strength of diurnal SST and the solar radiation is a secondary factor.

The annual mean and annual cycle of the diurnal SST variability in the simulations are compared with the satellite observations and reconstructed diurnal SST data based on the observations. Both experiments with the implementation of the parameterization show a comparable spatial distribution of the diurnal SST variability that is basically missed in the original CFS model. The annual mean of diurnal SST shows large amplitudes over regions including the northern Indian Ocean, the equatorial Pacific, the eastern equatorial Atlantic, as well as several coastal regions, such as the western Central America and northwest Australia. The large diurnal SST is also accompanied with mean states featuring strong daily peak solar radiation and light winds. The diurnal variation is generally large in the tropics throughout the year, while the strongest seasonal contrast of the diurnal SST is in the subtropical oceans between the boreal summer and winter. The large diurnal variability occurs in the subtropics that are under the atmospheric subtropical highs, which favors clear sky and relatively weak surface wind conditions. Additionally, the net solar radiation is strongest in summer. All these factors contribute to the enhancement of SST diurnal variability in the subtropical oceans of the summer hemisphere. In addition, the seasonality of diurnal SST over the Indian Ocean is greatly affected by the Indian monsoon. The strong diurnal cycle of the SST is apparent during the pre-monsoon season, and the diurnal variability is suppressed in boreal summer as the onset of the Indian summer monsoon induces strong tropical convection and increased surface winds.

The EOF analysis of simulated diurnal SST for different ocean basins display the consistent spatial pattern and the temporal evolution, similar to the patterns shown in the reconstructed data. More interestingly, there are several EOF modes of diurnal SST that show similar spatial distributions to some instances of SST interannual variability, such as the IOD in the Indian Ocean, ENSO in the Pacific Ocean and subtropical Atlantic SST

120

anomalies. Such coincidence might imply that the modulation of diurnal SST induced by the interannual variability of SSTs. The physical processes of the modulation and the possible feedbacks of diurnal SST on interannual SST variability need further investigation.

Over all, the parameterizations are able to produce the realistic diurnal SST in the model. Based on that, we investigate the influence of diurnal SST on the mean states of other variables. First of all, significant mean state errors in the CFS simulation still exist in all experiments for SST, rainfall, and 850 hPa zonal wind. These biases include the problematic mean SST distribution, the improper latitude and zonal locations of the ITCZ, and the underestimation of the lower tropospheric westerly winds, especially their zonal extension. Compared with the CTL run, the simulations involving the diurnal SST variability show a certain modulation of the mean states. Among these modulations, we find that the ZB and SG runs tend to compensate a portion of the mean state errors over several regions. For example, over the western Indian Ocean the CTL run show 1-1.5^{o}C warm biases of mean SST that are reduced by about 0.2-0.3^{o}C in the ZB and SG runs. Consequently, the biases of the precipitation over the western Indian Ocean are reduced. Closer inspection of the mean state biases in the ZB and CTL runs for different seasons reveals the rectification of the precipitation over the Maritime continent during the boreal summer, and increased intensity of lower tropospheric westerlies over the Indian Ocean and the Maritime Continent is also observed in summer.

The influence of the diurnal SST variability on the interannual SST variability over the eastern Pacific Ocean has been briefly discussed. All simulations generate the ENSO-like pattern of the SST anomalies over the area. The ZB and SG runs have a slightly changed amplitude of the cold/warm events, and the alternating phase of the cold/warm events becomes irregular in the ZB and SG runs compared with the CTL run. However, the dominant period of the ENSO-like oscillation is unchanged among all three of the experiments. Obviously a longer integration is necessary in the future to draw a robust conclusion on the interaction between SST variations of the diurnal scale and interannal scale.

Many previous studies reported that the diurnal cycle in SST has an impact on the tropical intraseasonal oscillation (ISO). In this research, a set of diagnoses is performed on the simulations for the ZB and CTL runs to explore the possible influence induced by the diurnal SST variability. As pointed out previously, both experiments generally suffer from similar mean state biases of SST, rainfall and 850hPa zonal winds for boreal summer and winter, and this may have an adverse impact on the simulation of tropical intraseasonal variability, including the magnitude, spatial pattern and the propagation of ISOs.

The standard deviation of the intraseasonal OLR anomalies indicates that both experiments tend to exaggerate the convective anomalies, especially over the summer hemisphere. Partly due to the mean SST biases, the associated enhanced convection is erroneously located over the western Indian Ocean in the boreal winter and in the Arabian Sea during the boreal summer for the ZB and CTL runs. For other regions such as the north of New Guinea and east of the Philippines, the ZB run displays more realistic convective anomalies compared with the CTL run.

For the propagation of the ISO in the simulations, the lag-longitude correlation and lag-latitude correlation are calculated. Both experiments produce comparable eastward propagation across the Indian and western Pacific Oceans during the boreal winter. The phase relationship between the convection and winds is captured by the simulations. However, the northward propagation of ISO is not represented in the results of either experiments.

The multivariate EOF analysis is conducted on an equatorially averaged OLR, 200- and 850-hPa zonal winds, and the leading pair of principle components is used to composite the ISO life cycle. There is no significant change of spectrum characteristics of the simulated ISOs. The ZB and CTL runs are able to capture several essential features of the ISO such as the phase relationship between convection anomalies and wind anomalies, and between SST anomalies and precipitation anomalies. However, the propagation of the ISO revealed in the life cycle composite is problematic in both the ZB and CTL runs. Besides these common features, the ZB run shows intensified intraseasonal anomalies of some fields including diurnal SST, SST, convection, precipitation, and surface wind speed. The

intensifications are apparent in almost every phase of the summer composite and in several phases of the winter composite. We hypothesize that the intensification mainly results from the model resolving the diurnal SST variability in the model. The significant diurnal warming of SST is coincident with the suppressed phase of the ISO, and the strong DSST anomalies will lead to the large SST anomalies in subsequent phases; then the intensified convection will form over the regions of the warmest SST.

Moreover, we attempt to quantitatively diagnose the nonlinear rectification of diurnal variability on the intraseasonal surface latent heat flux (LHF), with the approach adopted from Zhou and Li (2010). The result indicates that the diurnal-scale motion greatly feedbacks to the intraseasonal variability of the LHF over the Indian and western Pacific Oceans. The interaction between diurnal scale variability and mean state contributes more than 60% of intraseasonal LHF variation over the northern Indian Ocean throughout the year, and a similar impacts exists near the Sumatra and over the Java Sea in boreal winter. The nonlinear rectification is more significant over the Maritime continent in the ZB run than in the CTL run.

6.2   Limitations and future works

The coupling interval of 3-hour is set for all experiments. Although it is a great improvement from the original CFS model which only exchanges daily mean of the SST and fluxes between atmospheric and oceanic components, the 3-hour interval is still too long to generate the realistic SST variations which occurs instantaneously in the real world. Under the current model configurations, the mixed layer parameterizations receive the averaged fluxes from the atmospheric component and averaged bulk SST from the oceanic component to generate the skin SST. The newly calculated skin SST actually represents the condition of the past three hours but is used as the boundary condition for the following three hours. As shown in the observations, the skin SST may change dramatically in a short period especially during the daytime under the favorable weather conditions. The slow evolution of the simulated skin SST due to the model configuration may produce the biases we see

on the fields that are sensitive to the SST variations. For example, we have compared the simulations with a 1-hour coupling interval and a 3-hour interval. For the 1-hour coupling simulation, the daily precipitation peak appears at a time closer to the observations, especially over the oceans. One way to eliminate the limitation of the coupling interval is to embed the parameterization scheme into the atmospheric component, therefore the SST seen by the atmosphere can be updated at every integration time step, but as a trade off, the computational load will greatly increase.

Since the mixed layer parameterizations are independent of the oceanic model, it is only the numerically rectified values of SST that actually affect the structure and physical processes of the upper oceans. But in the observations such modification of the vertical structure near the sea surface is evident due to the appearance of the diurnal thermocline, and in the long term, it may have an impact on the SST variability of the longer time scale (Bernie et al. 2005). In our simulations, the impact of diurnal SST variability on the oceanic variability can be partly realized through the feedback of air-sea interaction. Determining what extent these indirect influences may contribute to the oceanic variation will require further assessment.

The mean states of the CFS model show the strong biases compared with the observations. Although the implementation of the diurnal SST variability leads to some reduction of model errors on several time-mean variables, the modification only accounts for a small portion of the model biases over a limited regions. It indicates that most of the CFS biases are mainly due to other deficiencies of the model rather than the absence of diurnal SST variability. On the other hand, it implies that certain physical processes may be incorrectly represented in the model, which may lead to the erroneous assessment of the influence of the diurnal SST variability. To reduce the influence of the model uncertainty, we can either conduct the ensemble simulation with a single model or perform a multi-model ensemble to identify the consistent patterns of the influences induced by the diurnal SST variability.

The diurnal SST variability most likely has the direct impacts on synoptic scale atmospheric variability, especially on the events appearing over the tropical/subtropical oceans

such as tropical/subtropical cyclones. Due to the coarse resolution of the CFS model, in this research we don't discuss the possible influences on cyclones, but it is worth applying the diurnal mixed layer parameterizations to a hurricane model and investigate the interaction between the diurnal SST and synoptic variability. Moreover, from our results it implies that the SST interannual variability may affect the diurnal SST variability, which needs further investigation. On the intraseasonal to seasonal variability, we study the possible impacts on the ISO events over the Indian and western Pacific Oceans. But the relationship between the Indian monsoon and diurnal SST variability, especially if there are feedbacks of diurnal SST on the onset of the monsoon, is also an interesting topic. Further more, if we can apply the realistic diurnal SST variability to a simplified theoretical coupled model instead of a full GCM, a better understanding of the fundamental mechanism of the impacts on other timescales may be achieved.

Bibliography

Bibliography

Alpert, J. C., M. Kanamitsu, P. Caplan, J. Sela, G. White, and E. Kalnay, 1988: Mountain induced gravity wave drag parameterization in the nmc medium-range model. *Preprints of the Eighth Conference on Numerical Weather Prediction*, Baltimore, MD, 726–733.

Anderson, S., R. A. Weller, and R. B. Lukas, 1996: Surface buoyancy forcing and the mixed layer of the western pacifc warm pool: Observations and 1d model results. *J. Climate*, **9**, 3056–3085.

Annamalai, H. and K. R. Sperber, 2005: Regional heat sources and the active and break phases of boreal summer intraseasonal(30-50 day) variability. *J. Atmos. Sci.*, **62**, 2726–2748.

Asselin, R., 1972: Frequency filter for time integrations. *Mon. Wea. Rev.*, **100**, 487–490.

Barnston, A. G., M. Chelliah, and S. B. Goldenberg, 1997: Documebtation of a highly enso-related sst region in the equatorial pacific. *Atmos. Ocean*, **35**, 367–383.

Bernie, D. J., S. J. Woolnough, J. M. Slingo, and E. Guilyardi, 2005: Modeling of diurnal and intraseasonal variability of the ocean mixed layer. *J.Climate*, **18**, 1190–1202.

Blade, I. and D. L. Hartmann, 1993: Tropical intraseasonal oscillations in a simple nonlinear model. *J. Atmos. Sci.*, **50**, 2922–2939.

Briegleb, B. P., P. Minnus, V. Ramanathan, and E. Harrison, 1986: Comparison of regional clear-sky albedo inferred from satellite observations and model computations. *J. Clim. and Appl. Meteo.*, **25**, 214–226.

Carlson, T. N., 1969: Synoptic histories of three african disturbances that developed into atlantic hurricanes. *Mon. Wea. Rev.*, **97**, 256–276.

Carton, J. A. and Z. Zhou, 1997: Annual cycle of sea surface temperature in the tropical atlantic ocean. *J. Geophys. Res.*, **102**, 27 813–27 824.

Chou, M. D., 1992: A solar radiation model for use in climate studies. *J. Atmos. Sci.*, **49**, 762–772.

Chou, M. D. and K. T. Lee, 1996: Parameterizations for the absorption of solar radiation by water vapor and ozone. *J. Atmos. Sci.*, **53**, 1204–1208.

Chou, M. D., M. J. Suarez, C. H. Ho, M. M. H. Yan, and K. T. Lee, 1998: Parameterizations for cloud overlapping and shortwave single scattering properties for use in general circulation and cloud ensemble models. *J. Climate*, **11**, 202–214.

Chu, P. S. and J. Frederick, 1990: Westerly wind bursts and surface heat flux in the equatorial western pacific in may 1992. *J. Meteor. Soc. Japan*, **68**, 523–537.

Clayson, C. and D. Weitlich, 2005: Vinterannual variability of tropical pacific diurnal sea surface temperature warming and nighttime cooling. *Geophys. Res. Lett.*, **32**, L21604, doi:10.1029/2005GL023786.

Clayson, C. and D. Weitlich, 2007: Variability of tropical diurnal sea surface temperature. *J. Climate*, **20**, 334–352.

Cornillon, P. and L. Stramma, 1985: The distribution of diurnal sea surface warming events in the western sargasso sea. *J.Geophys. Res.*, **90**, 11 811–11 815.

Cronin, M. F. and W. S. Kessler, 2002: Seasonal and interannual modulation of mixed layer variability at 0°, 110^ow. *Deep Sea Res., Part I*, **11**, 1–17.

Dai, A. and K. E. Trenberth, 2004: The diurnal cycle and its depiction in the community climate system model. *J. Climate*, **17**, 930–951.

Davey, M. K. and Coauthors, 2002: Stoic: A study of coupled model climatology and variability in tropical ocean regions. *Clim. Dyn.*, **18**, 403–420.

Deser, C. and C. A. Smith, 1998: Diurnal and semidiurnal variations of the surface wind field over the tropical pacific ocean. *J. Climate*, **11**, 1730–1748.

Dickey, T., J. Marra, D.E.Sigurdson, R. Weller, C. Kinkade, S. Zedler, J. Wiggert, and C. Langdon, 1998: Seasonal variability of bio-optical and physical properties in the arabian sea: October 1994-october 1995. *Deep Sea Res., Part II*, **45**, 2001–2025.

Donlon, C. J., P. Minnett, C.Gentemann, T. Nightingale, I.J.Barton, B.Ward, and M. Murray, 2002: Toward improved validation of satellite sea surface skin temperature measurements for climate research. *J. Climate*, **15**, 353–369.

Duchon, C. E., 1979: Lanczos filtering in one and two dimensions. *J. Appl. Meteor.*, **18**, 1016–1022.

Fairall, C., E. F. Bradley, J. S. Godfrey, G. A. Wick, J. B. Edson, and G. S. Young, 1996: Cool-skin and warm-layer effects on sea surface temperature. *J.Geophys. Res.*, **101**, 1295–1308.

Flament, P., M. Sawyer, and C. Trefois, 1994: Amplitude and horizontal structure of a large diurnal sea surface warming event during the coastal ocean dynamics experiment. *J.Phys. Oceanogr.*, **24**, 124–139.

Frey, H., M. Latif, and T. Stockdale, 1997: The coupled gcm echo-2. part i: The tropical pacific. *Mon. Wea. Rev.*, **125**, 703–720.

Gent, P. R. and J. C. MaWilliams, 1990: Isopycnal mixing in ocean circulation models. *J. Phys. Oceanogr.*, **20**, 150–155.

Gentemann, C. L., C. J. Donlon, A. Stuart-Menteth, and F. Wentz, 2003: Diurnal signals in satellite sea surface temperature measurements. *Geophys. Res. Lett.*, **30(3)**, 1140, doi: 10.1029/2002GL016291.

Godfrey, J. S., R. Houze, R. J. Jr., R.Lukas, J. Redelsperger, A. Sumi, and R. Weller, 1998: Coupled ocean-atmosphere response experiment(coare): An interim report. *J.Geophys. Res.*, **103**, 14 395–14 450.

Grell, G. A., 1993: Prognostic evaluation of assumprions used by cumulus parameterizations. *Mon. Wea.Rev*, **121**, 764–787.

Griffies, S. M., A. Gnanadesikan, R. C. Pacanowski, V. Larichev, J. K. Dukowicz, and R. D. Smith, 1998: Isoneutral diffusion in a z-coordinate ocean model. *J. Phys. Oceanogr.*, **28**, 805–830.

Grodsky, S. A., J. A. Carton, and S. Nigam, 2003: Near surface westerly wind jet in the atlantic itcz. *Geophys. Res. Lett.*, **30(19)**, 2009, doi:10.1029/2003GL017867.

Hayes, S., L. J. Mangum, J. Picaut, A. Sumi, and K. Takeuchi, 1991: Toga-tao: A moored array for real-time measurements in the tropical pacific ocean. *Bull. Amer. Meteor. Soc.*, **72**, 339–347.

Hendon, H. H., 2000: Impact of air-sea coupling on the madden-julian oscillation in a general circulation model. *J. Atmos. Sci.*, **57**, 3939–3952.

Hendon, H. H. and M. L. Salby, 1994: The life-cycle of the madden-julian oscillation. *J. Atmos. Sci.*, **51**, 2225–2237.

Hong, S. Y. and H. L. Pan, 1996: Nonlocal boundary layer vertical diffusion in a medium-range forecast model. *Mon. Wea. Rev.*, **124**, 2322–2339.

Horel, J. D., 1982: On the annual cycle of the tropical pacific atmosphere and ocean. *Mon. Wea. Rev*, **110**, 1863–1878.

Hou, Y. T., K. A. Campana, and S.-K. Yang, 1996: Shortwave radiation calculations in the ncep's global model. *International Radiation Symposium, IRS96*, Fairbanks, AL.

Hou, Y. T., S. Moorthi, and K. Campana, 2002: Parameterization of solar radiation transfer in the ncep models. NCEP Office Note 441.

Hu, Z. Z., B. Huang, and K. Pegion, 2008: Low cloud errors over the southeastern atlantic in the ncep cfs and their association with lower-tropospheric stability and air-sea interaction. *J. Geophys. Res.*, **113**, D12114, doi:10.1029/2007JD009514.

Huang, B., Z. Z. Hu, and B. Jha, 2007: Evolution of model systematic errors in the tropical atlantic basin from coupled climate hindcasts. *Clim. Dyn.*, **28**, 661–682.

Huang, B., P. S. Schopf, and J. Shukla, 2004: Intrinsic ocean-atmosphere variability of the tropical atlantic ocean. *J. Climate*, **17**, 2058–2077.

Huang, B. and J. Shukla, 2005: Ocean-atmosphere interactions in the tropical and subtropical atlantic ocean. *J. Climate*, **18**, 1652–1672.

Huang, N. E. and N. O. Attoh-Okine, 2005: *Hilbert-Huang Transforms in Engineering.* CRC Press, 313 pp.

Huang, N. E. and S. S. P. Shen, 2005: *Hilbert-Huang Transform and Its Applications.* World Sci., 311 pp.

Huang, N. E., Z. Shen, S. R. Long, M. C. Wu, E. H. Shih, Q. Zheng, C. C. Tung, and H. H. Liu, 1998: The empirical mode decomposition and the hilbert spectrum for nonlinear and non-stationary time series analysis. *Proc. Roy. Soc. Lond.*, **454A**, 903–993.

Inness, P. M. and J. M. Slingo, 2003: Simulation of the madden-julian oscillation in a coupled general circulation model. part i: Comparsion with observations and an atmosphere-only gcm. *J. Climate*, **16**, 345–364.

Inness, P. M., J. M. Slingo, E. Guiyardi, and J. Cole, 2003: Simulation of the madden-julian oscillation in a coupled general circulation model. part ii: The role of the basic state. *J. Climate*, **16**, 365–382.

Kawai, Y. and H. Kawamura, 2002: Evaluation of the diurnal warming of sea surface temperature using satellite-derived marine meteorological data. *J. Oceanogr.*, **58**, 805–814.

Kawai, Y. and A. Wada, 2007: Diurnal sea surface temperature variation and its impact on the atmosphere and ocean: a review. *J. Oceanogr.*, **63**, 721–744.

Kiladis, G. N., K. H. Straub, and P. T. Haertel, 2005: Zonal and vertical structure of the madden-julian oscillation. *J. Atmos. Sci.*, **62**, 2790–2809.

Kim, Y. J. and A. Arakawa, 1995: Improvement of orographic gravity wave parameterization using a mesoscale gravity wave model. *J .Atmos. Sci.*, **52**, 1875–1902.

Large, W., J. C. McWilliams, and S. C. Doney, 1994: Ocean vertical mixing :a review and a model with a nonlocal boundary layer parameterization. *Rev. Geophys.*, **32**, 363–403.

Latif, M. and Coauthors, 2001: Ensip: The el nino simulation intercomparison project. *Climate Dyn.*, **18**, 255–276.

Lau, K. M., J. H. Kim, and Y. Sud, 1996: Intercomparison of hydrologic processes in amip gcms. *Bull. Amer. Meteor. Soc.*, **77**, 2209–2227.

Lawrence, D. M. and P. J. Webster, 2002: The boreal summer intraseasonal oscillation: Relationship between northward and eastward movement of convection. *J. Atmos. Sci.*, **59**, 1593–1606.

Li, W., R. Yu, H. Liu, and Y. Yu, 2001: Impacts of diurnal cycle of sst on the interseasonal variation of surface heat flux over the western pacific warm pool. *Adv. Atmos. Sci.*, **18**, 793–806.

Lin, J. L. and Coauthors, 2006: Tropical intraseasonal variability in 14 ipcc ar4 climate models. part i: Convective signals. *J. Climate*, **19**, 2665–2690.

Liu, Z., 1996: Modeling equatorial annual cycle with a linear coupled model. *J. Climate*, **9**, 2376–2385.

Loschnigg, J. and P. J. Webster, 2000: A coupled ocean-atmosphere system of sst regulation for the indian ocean. *J. Climate*, **13**, 3342–3360.

Luo, J. J., S. Masson, A. W. Robertson, and A. Arakawa, 2005: Reducing climatology bias in an oceanatmosphere cgcm with improved coupling physics. *J. Climate*, 2344–2360.

Madden, R. A. and P. R. Julian, 1971: Detection of a 40-50-day oscillation in the zonal wind in the tropical pacific. *J. Atmos. Sci.*, **28**, 702–708.

Madden, R. A. and P. R. Julian, 1994: Observations of the 40-50-day tropical oscillation-a review. *Mon. Wea. Rev.*, **122**, 814–837.

Mahrt, L. and H. L. Pan, 1984: A two-layer model of soil hydrology. *Bound. Layer Meteor.*, **29**, 1–20.

Manganello, J. V. and B. Huang, 2009: The influence of systematic errors in the southeast pacific on enso variability and prediction in a coupled gcm. *Clim. Dyn.*, **32**, 1015–1034.

Matthews, A. J., 2000: Propagation mechanisms for the madden-julian oscillation. *Quart. J. Roy. Meteor. Soc*, **126**, 2637–2651.

Matthews, E., 1985: Atlas of archived vegetation, land use, and seasonal albedo data sets. NASA Technical Memorandum 86199, Goddard Institute for Space Studies, New York, NY.

McPhaden, M. and Coauthors, 2009: Rama: The research moored array for africanasianaustralian monsoon analysis and prediction. *Bull. Amer. Meteor. Soc.*, **90**, 459–480.

Mechoso, C. R., cited 2006: modeling the south eastern pacific climate: Progress and challenges. ncep emc seminar, [available online at http://www.emc.ncep.noaa.gov/seminars/presentations/2006/mechoso.ncep.jan.06.ppt].

Mechoso, C. R. and Coauthors, 1995: The seasonal cycle over the tropical pacific in coupled ocean-atmosphere general circulation models. *Mon. Wea. Rev.*, **123**, 2825–2838.

Meehl, G. A., C. Covey, B. McAvaney, M. Latif, and R. J. Stouffer, 2005: Overview of the coupled model intercomparison project. *Bull. Amer. Meteor. Soc.*, **86**, 89–93.

Mellor, G. and T. Yamada, 1974: A hierarchy of turbulent closure models for planetary boundary layers. *J. Atmos. Sci.*, **31**, 1791–1806.

Mitchell, T. and J. M. Wallace, 1992: The annual cycle in equatorial convection and sea surface temperature. *J. Climate*, **5**, 1140–1156.

Moorthi, S., H. L. Pan, and P. Caplan, 2001: Changes to the 2001 ncep operational mrf/avn global analyssi/forecast system. NWS Tech. Procedures Bulletin 484, 14 pp.

Niller, P. P. and E. Kraus, 1977: *One-dimensional models: Modeling and Prediction of the Upper Layers of the Ocean*. Pergamon Press, 285 pp.

Nowlin, W. D. and Coauthors, 1996: An ocean observing system for climate. *Bull. Amer. Meteor. Soc.*, **77**, 2243–2273.

Pacanowski, R. C. and S. M. Griffies, 1998: Mom 3.0 manual. Tech. rep., NOAA/GFDL.

Pan, H. L. and W. S. Wu, 1995: Implementing a mass flux convection parameterization package for the nmc medium-range forecast model. NMC Office Note 409, 40 pp.

Pan, X., B. Huang, and J. Shukla, 2010: Sensitivity of the tropical pacific seasonal cycle enso to changes in mean state induced by a surface heat flux adjustment in ccsm3. *Clim. Dyn.*, doi:10.1007/s00382-010-0923-y.

Pegion, K. and B. P. Kirtman, 2008: The impact of air-sea interactions on the simulation of tropical intraseasonal variability. *J. Climate*, **21**, 6616–6635.

Phillander, S. G. H. and Y. Chao, 1991: On the contrast between the seasonal cycles of the equatorial atlantic and pacific oceans. *J. Phys, Oceanogr.*, **21**, 1399–1406.

Pinsky, M. A., 2002: *Introduction to Fourier Analysis and Wavelets*. Brooks/Cole, 400 pp.

Pollard, R., P. B. Rhines, and R. O. R. Y. Thompson, 1973: The deepening of the wind-mixed layer. *Geophys. Fluid Dyn.*, **4**, 381–404.

Price, J., C. N. K. Mooers, and J. C. V. Leer, 1978: Observation and simulation of storm-induced mixed-layer deepening. *J. Phys. Oceanogr*, **8**, 582–599.

Price, J. and R. A. Weller, 1986: Diruanl cycling: Observation and models of the upper ocean response to diurnal heating, cooling and wind mixing. *J.Geophys. Res.*, **91**, 8411–8427.

Qin, H., H. Kawamura, and Y. Kawai, 2007: Detection of hot event in the equatorial indo-pacific warm pool using advanced satellite sea surface temperature, solar radiation, and wind speed. *J. Geophys. Res.*, **112**, 07015, doi:10.1029/2006JC003969.

Qin, H., H. Kawamura, F. Sakaida, and K. Ando, 2008: A case study of the tropical hot event in november 2006 (he0611) using a geostationary meteorological satellite and the tao/triton mooring array. *J. Geophys. Res.*, **113**, 08045, doi:10.1029/2007JC004640.

Reynolds, R. W., 1988: A real-time global sea surface temperature analysis. *J. Climate*, **1**, 75–88.

Reynolds, R. W., 1993: Impact of mount pinatubo aerosols on satellite-derived sea surface temperatures. *J. Climate*, **6**, 768–774.

Reynolds, R. W. and D. C. Marsico, 1993: An improved real-time global sea surface temperature analysis. *J. Climate*, **6**, 114–119.

Reynolds, R. W. and T. M. Smith, 1994: Improved global sea surface temperature analyses using optimum interpolation. *J. Climate*, **7**, 929–948.

Roll, H., 1965: *Physics of the Marine Atmosphere, International Geophysics Series*, Vol. 7. Academic Press, New York, 426 pp.

Rui, H. and B. Wang, 1990: Development characteristics and dynamic structure of tropical intraseasonal convection anomalies. *J. Atmos. Sci.*, **47**, 357–379.

Saha, S., et al., 2006: The ncep climate forecast system. *J. Climate*, **19**, 3483–3517.

Saji, N. H., B. N. Goswami, P. N. Vinayachandran, and T. Yamagata, 1999: A dipole mode in the tropical indian ocean. *Nature*, **401**, 360–363.

Sakaida, F., J. Kudoh, and H. Kawamura, 2000: A-highers-the system to produce the high spatial resolution sea surface temperature maps of the western north pacific using the avhrr/noaa. *J. Oceanogr.*, **56**, 707–716.

Schiller, A. and J. S. Godfrey, 2005: A diagnostic model of the diurnal cycle of sea surface temperature for use in coupled ocean-atmosphere models. *J.Geophys. Res.*, **110**, C11 014, doi:10.1029/2005JC002 975.

Schneider, E. K., 2002: Understanding differences between the equatorial pacific as simulated by two coupled gcms. *J. Climate*, **15**, 449–469.

Servain, J. and Coauthors, 1998: A pilot research moored array in the tropical atlantic (pirata). *Bull.Amer. Meteor. Soc.*, **85**, 167–172.

Shinoda, T. and H. H. Hendon, 1998: Mixed layer modeling of intraseasonal variability in the tropical western pacific and indian oceans. *J. Climate*, **11**, 2668–2685.

Slingo, J. M., P. Inness, R. Neale, S. Woolnough, and G. Y. Yang, 2003: Scale interactions on diurnal to seasonal timescales and their relevance to model systematic errors. *Ann. Geophys.*, **46**, 139–155.

Smagorinsky, J., 1963: General circulation experiments with the primitive equations: I. the basic experiment. *Mon. Wea. Rev.*, **91**, 99–164.

Smith, N. and G. T. Needler, 1995: An ocean observin system for climate. *Climatic Change*, **31**, 475–494.

Soloviev, A. V., 1982: On the vertical structure of the ocean thin surface layer at light wind. *Dokl. Acad. Sci. USSR, Earth Sci. Ser., Engl. Transl.*, 751–760.

Soloviev, A. V. and R. Lukas, 1997: Observation of large diurnal warming events in the near-surface layer of the western equatorial warm pool. *Deep-sea Res.*, **44**, 1055–1076.

Sperber, K. R., 2003: Propagation and the vertical structure of the madden-julian oscillation. *Mon. Wea. Rev.*, **131**, 3018–3037.

Staylor, W. and A. C. Wilbur, 1990: Global surface albedoes estimated from erbe data. *Preprints of the Seventh Conference on Atmospheric Radiation*, San Francisco CA, AMS, 231–236.

Stommel, H., K. Saunders, W. Simmons, and J. Cooper, 1965: Observations of the diurnal thermocline. *Deep-Sea Res.*, **16**, 269–284.

Stuart-Menteth, A., I. Robinson, and P. Challenor, 2003: A global study of diurnal warming using satellite-derived sea surface temperature. *J. Geophys. Res.*, **105(C5)**, 3155, doi: 10.1029/2002JC001534.

Sui, C., X. Li., K. M. Lau, and D. Adamec, 1997: Multiscale air-sea interactions during toga coare. *Mon. Wea. Rev.*, **125**, 448–462.

Sundqvist, H., E. Berge, and J. E. Kristjansson, 1989: Condensation and cloud studies with mesoscale numerical weather prediction model. *Mon. Wea. Rev.*, **117**, 1641–1757.

Sverdrup, H. U., M. W. Johnson, and R. H. Fleming, 1942: *The oceans : Their Physics, Chemistry and General Biology.* Prentice-Hall, Englewood Cliffs, New York, 1087 pp.

Thompson, B., J. Crease, and J. Gould, 2001: The origins, development and conduct of woce. *Ocean Circulation and Climate*, Academic Press, 31–43.

Tichmarsh, E., 1948: *Introduction to the theory of Fourier integrals.* Oxford University Press, 394 pp.

Troen, I. and L. Mahrt, 1986: A simple model of the atmospheric boundary layer; sensitivity to surface evaporation. *Bound.-Layer Meteor.*, **37**, 129–148.

Vitart, F., 2009: mpact of the madden julian oscillation on tropical storms and risk of landfall in the ecmwf forecast system. *Geophys. Res. Lett.*, **36**, L15802, doi: 10.1029/2009GL039089.

Waliser and Coauthors, 2009: Mjo simulation diagnostics. *J. Climate*, **22**, 3006–3030.

Waliser, D. and Coauthoers, 2003: Agcm simulations of intraseasonal variability associated with the asian summer monsoon. *Climate Dyn.*, **21**, 423–446.

Waliser, D. E., 2006: *Intraseasonal variability.* Springer, 203-258 pp.

Wang, B. and H. Rui, 1990: Synoptic climatology of transient tropical intraseasonal convection anomalies:1975-1985. *Meteor. Atmos. Phys.*, **44(1-4)**, 43–61.

Wang, B., R. Wu, and T. Li, 2003: Atmosphere-warm ocean interaction and its impacts on asian-australian monsoon variation. *J. Climate*, **16**, 1195–1211.

Wang, B. and X. Xie, 1997: A model for the boreal summer intraseasonal oscillation. *J. Atmos. Sci.*, **54**, 72–86.

Wang, W., S. Saha, H. L. Pan, S. Nadiga, and G. White, 2005: Simulation of enso in the new ncep coupled forecast system model. *Mon. Wea. Rev.*, **133**, 1574–1593.

Ward, B., 2006: Thermometric measurements of the molecular sublayer at the air-water interface. *J. Geophys. Res*, **111**, C02005, doi:10.1029/2004JC002689.

Weare, B. C., 2006: Centered composite analysis of variations associated with the madden-julian oscillation. *J. Climate*, **19**, 1834–1849.

Weare, B. C., P. T. Strub, and M. D. Samuel, 1981: Annual mean surface heat fluxes in the tropical pacific ocean. *J. Phys, Oceanogr*, **11**, 705–717.

Webster, P. and R. Lukas, 1992: Toga-coare: The coupled ocean-atmosphere response experiment. *Bull. Amer. Meteor. Soc.*, **73**, 1377–1416.

Webster, P. J., C. A. Clayson, and J. A. Curry, 1996: Clouds, radiation, and the diurnal cycle of sea surface temperature in the tropical western pacific. *J. Climate*, **9**, 1712–1730.

Webster, P. J., V. Magana, T. Palmer, J.Shukla, R.A.Tomas, M.Ynai, and T.Uasunari, 1998: Monsoons: Processes, predictability, and the prospects for prediction. *J.Geophys.Res*, **103**, 14 451–14 510.

Wheeler, M. C. and H. H. Hendon, 2004: An all-season real-time multivariate mjo index: Development of an index for monitoring and prediction. *Mon. Wea. Rev.*, **132**, 1917–1932.

Wick, G. A., J. C. Holmann, C. W. Fairall, and A. T. Jessup, 2005: Improved oceanic cool skin correlation using a refined solar penetration model. *J. Phys. Oceanogr.*, **35**, 1986–1996.

Woods, J. and W. Barkmann, 1986: The response of the upper ocean to solar heating. i: The mixed layer. *Quart. J. R. Met. Soc.*, **112**, 1–27.

Woolnough, S. J., F. Vitart, and M. A. Balmaseda, 2007: The role of the ocean in the madden-julian oscillation: Implications for mjo prediction. *Q. J. R. Meteorol. Soc.*, **133**, 117–128.

Wu, Z. and N. E. Huang, 2009: Ensemble empirical mode decomposition: a noise-assisted data analysis method. *Advances in Adaptive data Analysis*, **1**, 177–229.

Xie, P. and P. A. Arkin, 1997: Global precipitation: A 17-year monthly analysis based on gauge observations, satellite estimates and numerical model outputs. *Bull. Amer. Meteor. Soc.*, **78**, 2539–2558.

Xie, S. P., 1994: On the genesis of the equatorial annual cycle. *J. Climate*, **7**, 2008–2013.

Yasunari, T., 1979: Cloudiness fluctuations associated with the northern hemisphere summer monsoon. *J. Meteor. Soc. Japan*, **57**, 227–242.

Yasunari, T., 1981: Structure of an indian summer monsoon system with around 40-day period. *J. Meteor. Soc. Japan*, **59**, 336–354.

Yokoyama, R., S. Tanba, and T. Souma, 1995: Sea surface effects on the sea surface temperature estimation by remote sensing. *Int. J. remote Sens.*, **16**, 227–238.

Zeng, X. and A. Beljaars, 2005: A prognostic scheme of sea surface skin temperature for modeling and data assimilation. *Geophys. Res. Lett*, **25**, 1411–1414.

Zhang, C., 2005: Madden-julian oscillation. *Rev. Geophys.*, **43**, RG2003, doi: 10.1029/2004RG000158.

Zhang, C., M. Dong, S. Gualdi, H. H. Hendon, E. D. Maloney, A. Marshall, K. R. Sperber, and W. Wang, 2006: Simulations of the madden-julian oscillation in four pairs of coupled and uncoupled models. *Climate Dyn.*, **27**, 573–592.

Zhang, G. J. and H. Wang, 2006: Toward mitigating the double itcz problem in ncar ccsm3. *Geophys. Res. Lett.*, **33**, L06709, doi:10.1029/2005GL025229.

Zhao, Q. Y. and F. H. Carr, 1997: A prognostic cloud scheme for operational nwp models. *Mon. Wea. Rev.*, **125**, 1931–1953.

Zhou, C. and T. Li, 2010: Upscale feedback of tropical synoptic variability to intraseasonal oscillations through the nonlinear rectification of the surface latent heat flux. *J. Climate*, **23**, 5738–5754.

Curriculum Vitae

Jian Li grew up in Xinjiang, China. He attended Lanzhou University, where he received his Bachelor of Science in Meteorology in 2002. He went on to receive his Master of Science in Meteorology from Beijing University in 2005. He then received his Doctorate in Climate Dynamics from George Mason University in 2011. He will be a postdoctoral scholar at Center for Ocean Land Atmosphere Studies, Maryland in Fall 2011.